Module 3501: Lithosphere – Application of SAR Interferometry to Monitor Crustal Deformation

Dr. Mahdi Motagh
Helmholtz Center Potsdam, GFZ

DLR seit 1558 TECHNISCHE UNIVERSITÄT MÜNCHEN GFZ Helmholtz Centre Potsdam SAREDU Remote Sensing Education Initiative

Educational Objectives

- To get introduced to the application of SAR interferometry and advanced InSAR time-series methods (Persistent scatterer - PS, Small BAseline Subset - SBAS) to understand deformation processes associated with geohazards such as earthquakes, volcanoes, withdrawal of crustal fluids and landslides.
- To learn about some analytical geophysical models for interpretation of coseismic, interseismic, postseismic and volcano deformation fields from InSAR measurements.
- To understand the limitations of interferometric measurements in different applications.

Tutorials

- Doris short course – software for interferometric SAR processing.
- StaMPS/MTI short course – software for PS and SBAS processing.

Requirements

- Basic knowledge of SAR remote sensing

  (Module ID 1000: Basics - Mathematics / Physics / Data Processing / SAR Basics)

- You know how SAR interferometry and differential SAR interferometry work

  (Module ID 2200: Radar Interferometry)

Further Reading

- Bürgmann, R., Rosen, P., & Fielding, E. (2000). Synthetic Aperture Radar Interferometry to measure Earth's surface topography and its deformation. *Annual Review of Earth and Planetary Sciences, 28*, 169-209.
- Dzurisin, D. (2007). *Volcano Deformation: Geodetic Measuring Techniques*. Berlin, Heidelberg: Springer-Verlag. ISBN 3540426426.
- Madsen, S. N. & Zebker, H. A. (1998). Synthetic Aperture Radar Interferometry: Principles and Applications. In: Henderson, F. M., & Lewis, A. J. (eds.) (1998). *Manual of Remote Sensing - Principles and Applications of Imaging Radar* (3rd ed.) (pp. 359-380). New York: John Wiley & Sons.
- Massonnet, D., & Feigl, K. L. (1998). Radar interferometry and its application to changes in the earth's surface. *Reviews of Geophysics, 36*, 441-500.
- Simons, M. & Rosen, P. (2007). Interferometric Synthetic Aperture Radar Geodesy. In: Schubert, G. & Herring, T. (eds.). *Treatise on Geophysics, Volume 3: Geodesy* (pp. 391-446), New York: Elsevier Press. Retrieved on October 10, 2012 from http://www.gps.caltech.edu/~simons/pdfs/Simons_Treatise.pdf
- Segall, P. (2010). *Earthquake and volcano deformation*. Princeton University Press.

Structure

- Introduction to Plate Tectonics
- InSAR and earthquakes
- InSAR and postseismic deformation
- InSAR and interseismic deformation
- InSAR and volcano deformation
- InSAR and landslides
- InSAR and anthropogenic deformation

  [see also Module 3101: Anthroposphere – SAR Interferometry]

SAREDU Remote Sensing Education Initiative

Structure

- Introduction to Plate Tectonics
- InSAR and earthquakes
- InSAR and postseismic deformation
- InSAR and interseismic deformation
- InSAR and volcano deformation
- InSAR and landslides
- InSAR and anthropogenic deformation

  [see also Module 3101: Anthroposphere – SAR Interferometry]

Introduction to Plate Tectonics

- All continents have moved to their present positions from one Super-continent called Pangaea ('all land' in Greek); first proposed by Alfred Wegner in early 20th century.
- The basic idea in the theory of Plate tectonics is that the Earth's outermost layer, the lithosphere, is divided into a number of interlocking tectonic plates which are floating on the mantle.
- Deformation takes place at plate margins.

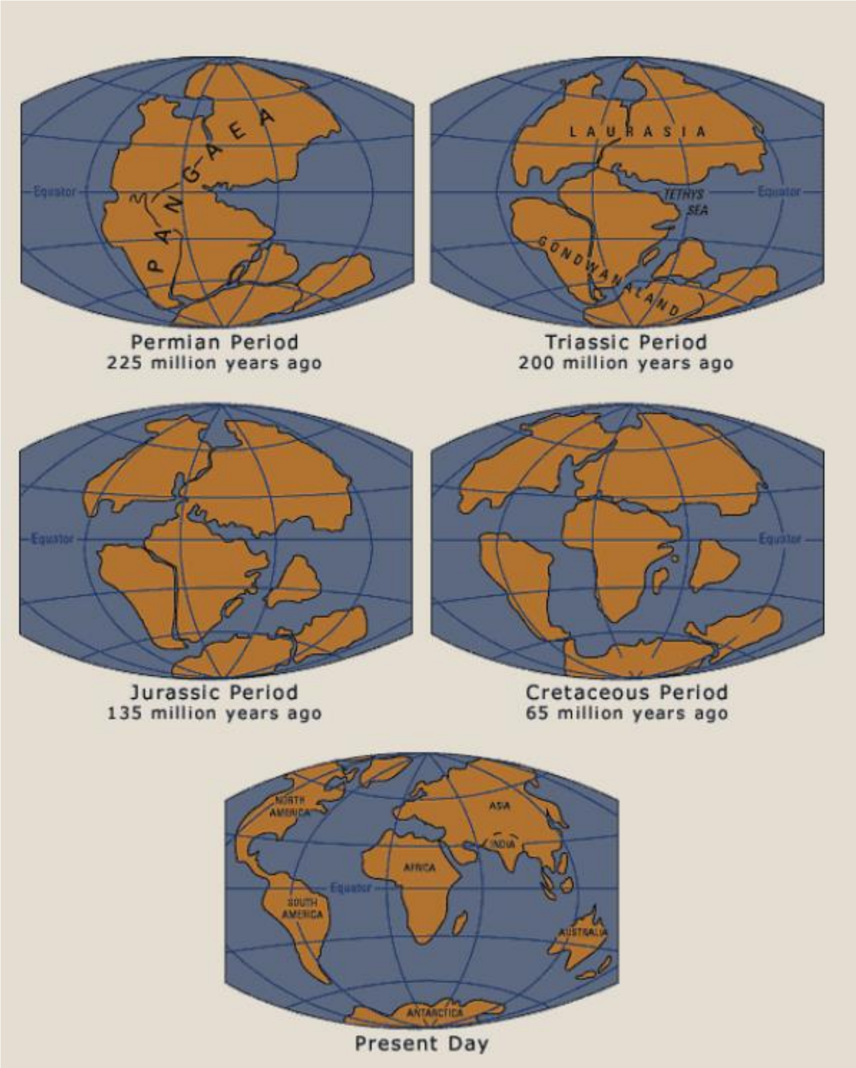

http://www.exploratorium.edu/faultline/PDFs/pangaea.pdf

SAREDU Remote Sensing Education Initiative

Categories of plate boundaries

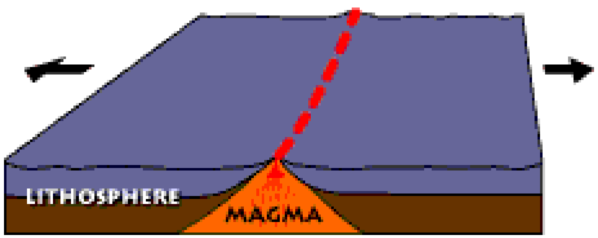

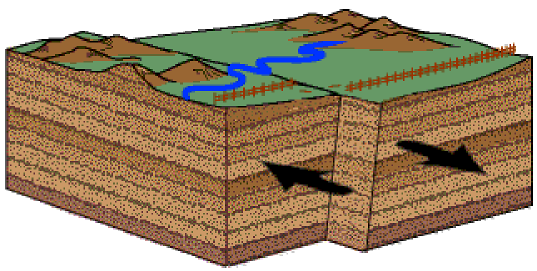

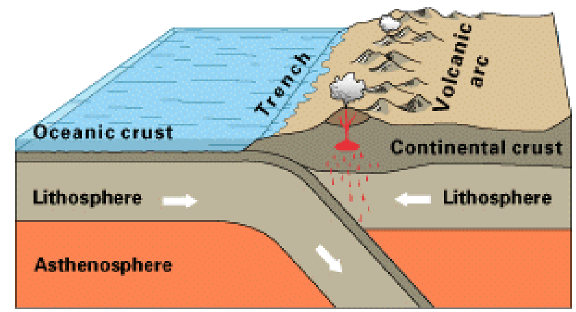

Oceanic-continental convergence

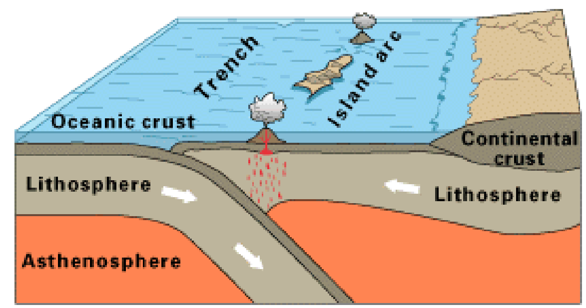

Oceanic-oceanic convergence

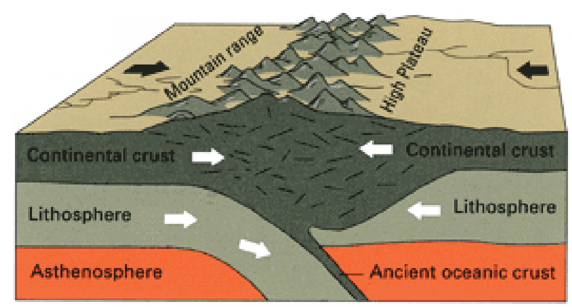

Continental-continental convergence

- Left: **Divergent**: Plates move away from each other
- Middle: **Transform:** Plates move past another
- Right: **Convergent:** Plates moves towards one another. Three types of convergent boundaries: **Oceanic-Continental, Oceanic-Oceanic** and **Continental-Continental**

(Image source: USGS)

SAREDU Remote Sensing Education Initiative

Relative plate motions

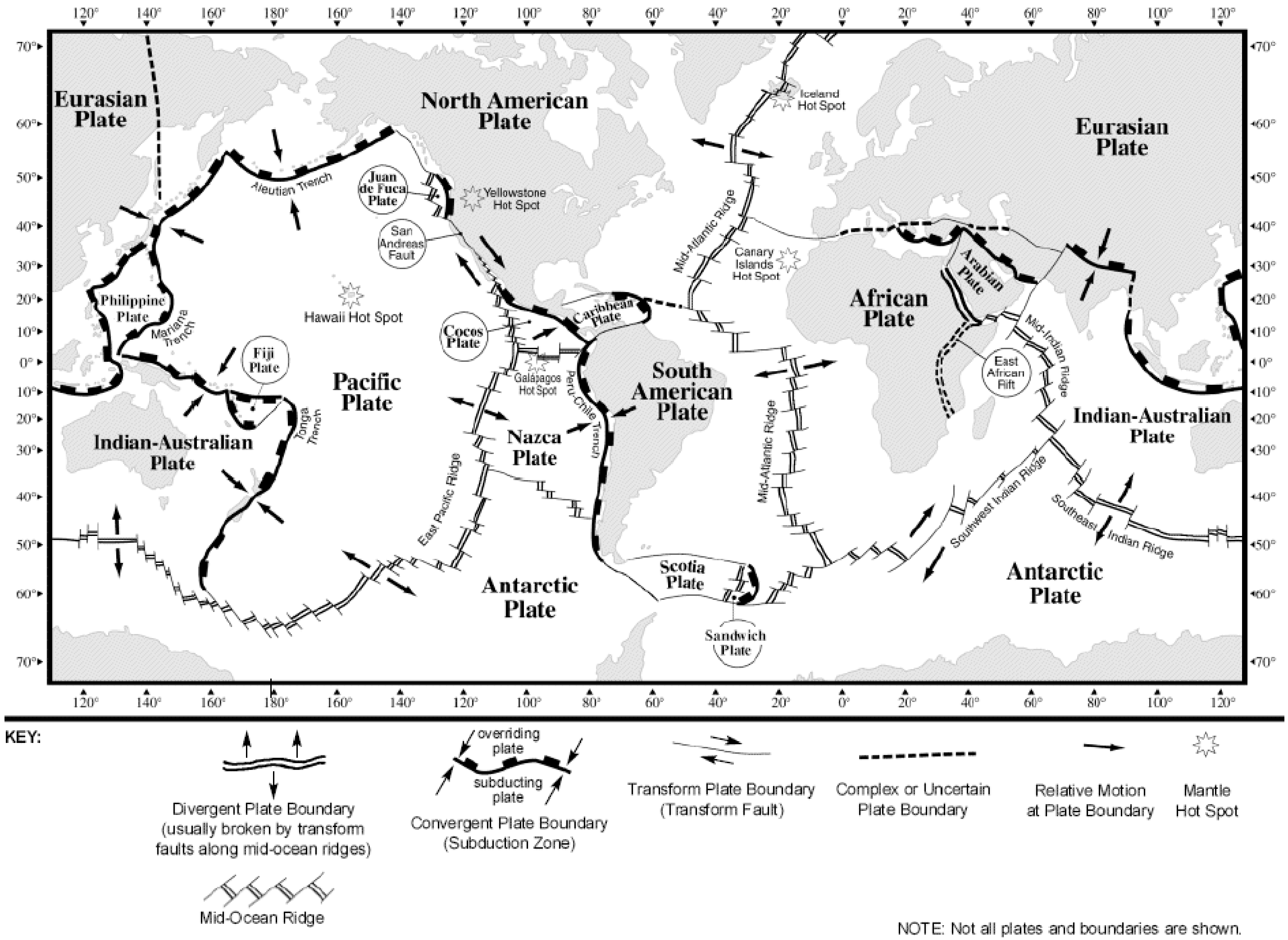

http://www.regentsearthscience.com/tsunami/plates.gif

Earthquake

Earthquake: is the sudden break of the lithosphere along a fault

- **Interplate earthquake**: is an earthquake that occurs at the boundary between two tectonic plates. Interplate earthquakes account for more than 90 percent of seismic energy release around the world.

- **Intraplate earthquake:** is an earthquake that occurs in the interior of a tectonic plate

Distribution of earthquakes

- Plate tectonic predicts that the majority of the Earth's tectonic activity takes place at the margins of the plates
- Location of earthquake epicenters define plate boundaries

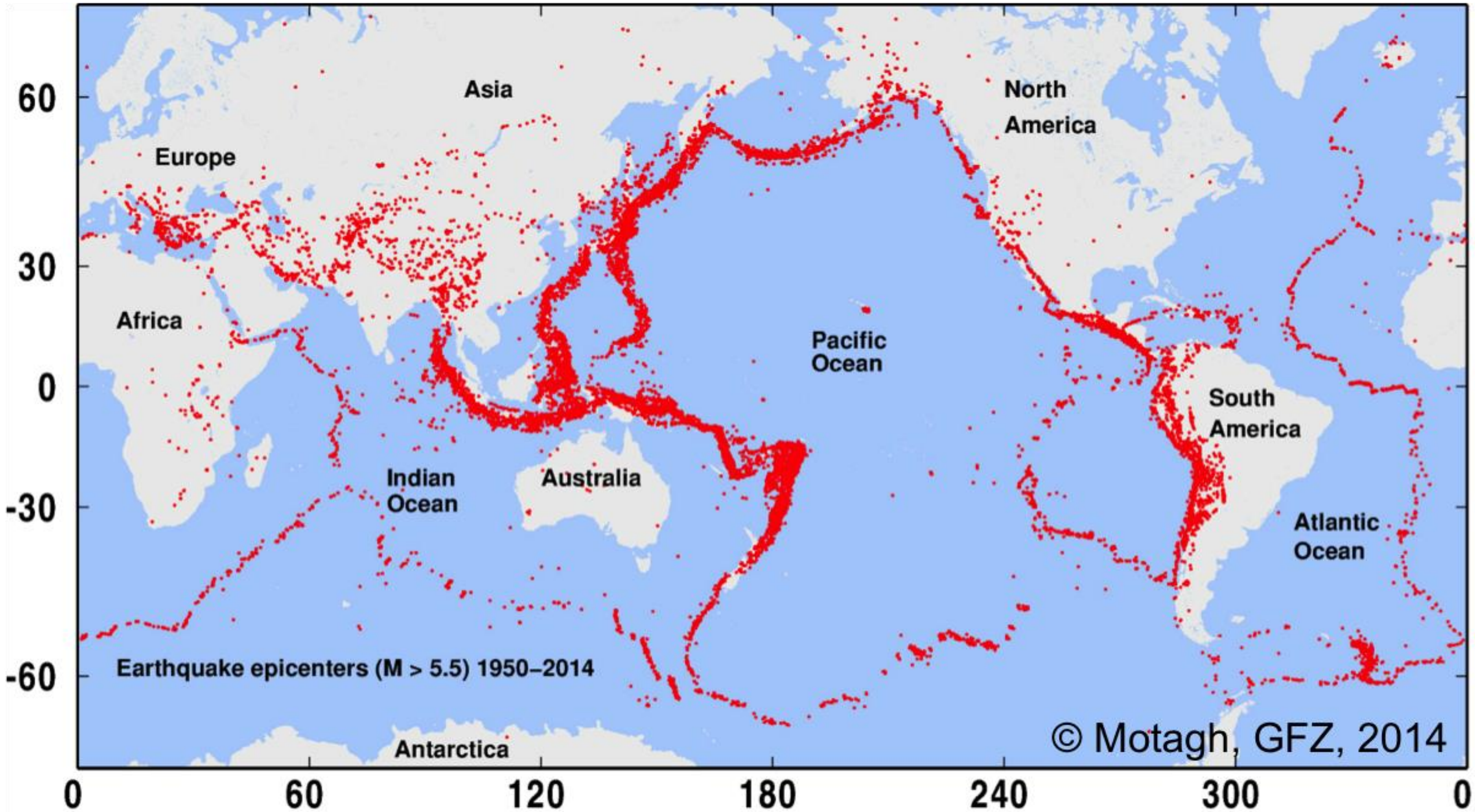

Mechanism of earthquakes

Reid's Elastic rebound theory

- Provides a simple explanation of how seismic energy is spread during earthquakes
- Rocks on opposite sides of the fault accumulate energy and slowly deform (interseismic deformation) until their internal strength is exceeded at the time of earthquake
- The theory is too simplistic. It cannot explain e.g. rapid transient deformation that often occurs following an earthquake

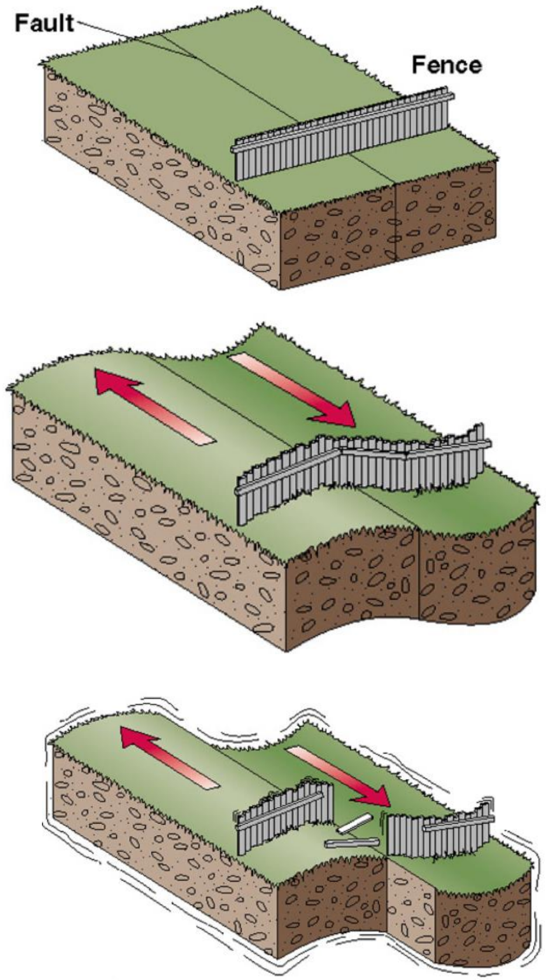

Original positions

Deformation (interseismic)

Sudden rupture (earthquake) and the release of energy

Seismic cycle

- **Inter-seismic slip**

  Refers to the slow process of elastic strain accumulation occurring for long periods above the interseismically locked portions of a fault

- **Co-seismic slip**

  Refers to the sudden slip that occurs on the locked portion of the fault at the time of earthquake

- **Post-seismic slip**

  Refers to the transient slip that occurs in the periods of minutes to years after the earthquake

Seismic cycle

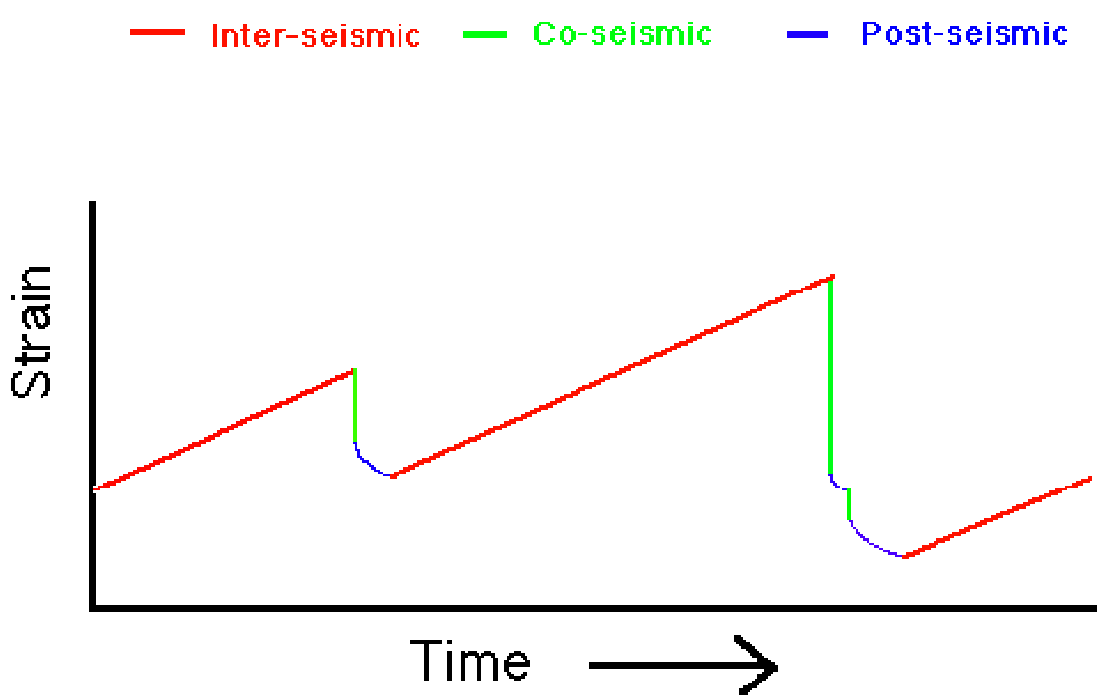

The term "cycle" does not mean that the earthquake occurrence is periodic, but refers instead to the repeated rupture of a fault

History of strain accumulation and release along a single fault patch.

http://geoscience.wisc.edu/~chuck/Classes/Mtn_and_Plates/eq_cycle.html

Earthquake Faults

Faults are classified based on how adjacent blocks of rocks on each side of the fault or fault zone move past each other

- **Strike-slip fault**

  Refers to the sideways movement of blocks

- **Thrust (Reverse) fault**

  The block above the fault moves up relative to the block below the fault due to compression

- **Normal fault**

  The block above the fault moves down relative to the block below the fault due to extension

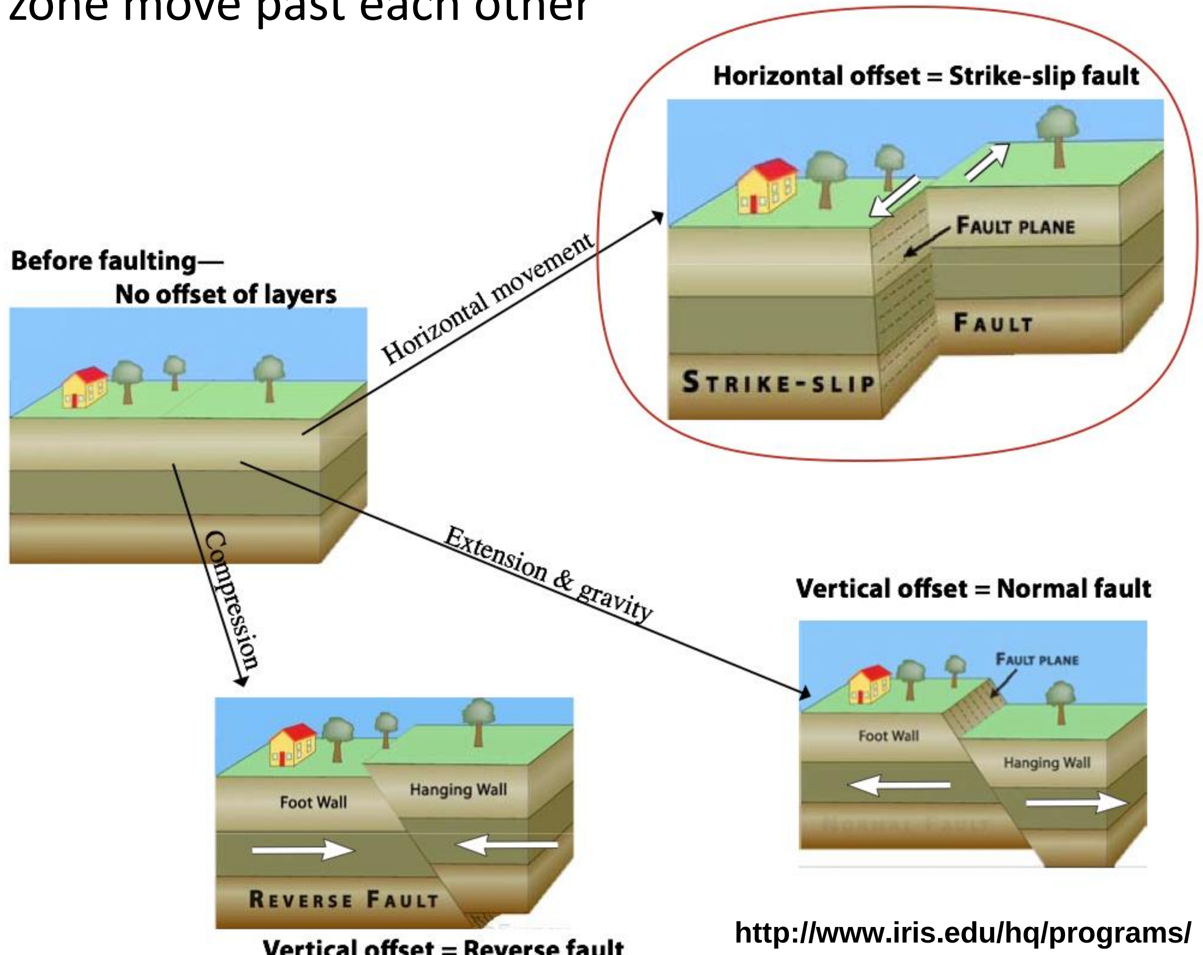

http://www.iris.edu/hq/programs/education_and_outreach/animations/2

SAREDU Remote Sensing Education Initiative

InSAR and crustal deformation

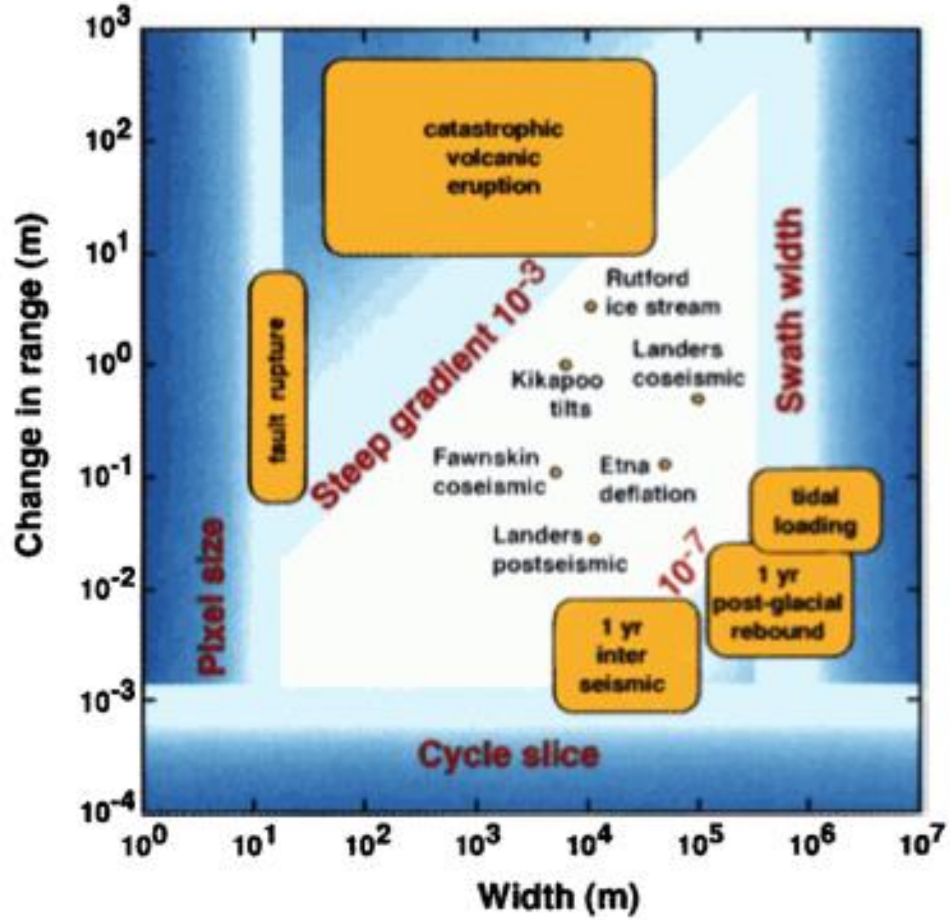

Massonnet & Feigl, 1998

Classification of crustal deformation signals by width and range change. To be detected by interferometry, a signal must fall within the white irregular pentagon. Each of its sides indicates a different physical limit.

Structure

- Introduction to Plate Tectonics
- InSAR and earthquakes
- InSAR and postseismic deformation
- InSAR and interseismic deformation
- InSAR and volcano deformation
- InSAR and landslides
- InSAR and anthropogenic deformation

  [see also Module 3101: Anthroposphere – SAR Interferometry]

SAREDU Remote Sensing Education Initiative

InSAR and earthquake

- **Goal:**
  - To derive reliable source parameters (fault geometry) and high-resolution fault slip models for earthquakes

- **Why?**
  - Mapping of coseismic ground deformation allows for a better understanding of the mechanics of earthquake process and mechanical behavior of the upper layers of the Earth
  - Source parameters obtained from the inversion of coseismic ground deformation data provide important inputs for a variety of models and processes including stress change following an earthquake, postseismic models, and fault interactions

SAREDU Remote Sensing Education Initiative

InSAR and earthquake

- **Data requirements:**
  - Two radar images, one before the earthquake and one after the earthquake with the same polarization, together with an external DEM. DEM can also be constructed interferometrically with a 3rd SAR image.

- **Main tools:**
  - Dislocation theory (e.g. Okada, 1985)
  - Inversion methodologies (e.g. Du et al.,1992; Cervelli et al., 2001)

SAREDU Remote Sensing Education Initiative

Rectangular dislocation in elastic half-space model

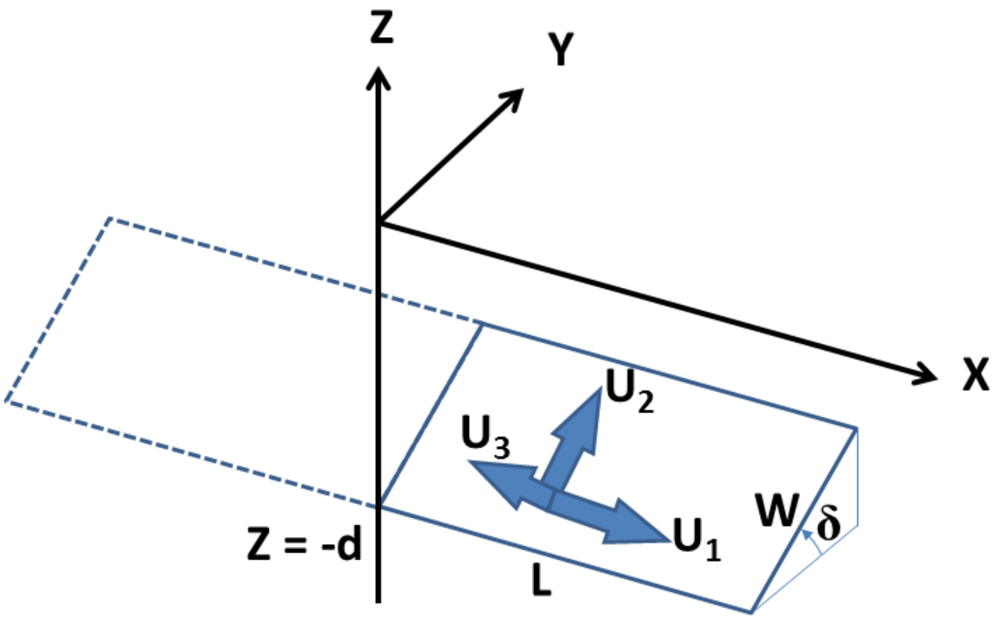

Sketch of rectangular dislocation typically employed for source inversion of earthquakes from geodetic data. L=length, W=width, δ=dip angle, d=lower depth of the fault plane. U_1, U_2 and U_3 correspond to strike-slip, dip-slip and tensile components of an arbitrary dislocation, respectively.

Okada, 1985

Elasticity

- Elasticity refers to the continuum mechanics of bodies which deform reversibly under stress

- Linear elastic deformation is governed by Hooke's law:

$$s = Ee$$

s : Applied stress

E : Material constant called Young's modulus

e: Strain

Aki & Richards, 1980

SAREDU Remote Sensing Education Initiative

Elasticity

- Partial differential equation for static deformation in elastic medium:

$$(/ + 2m)\nabla(\nabla \cdot \mathrm{u}) - m\nabla \times (\nabla \times \mathrm{u}) = \nabla \cdot \mathrm{G}$$

$/$: first Lamé constant

m: shear modulus or second Lamé constant

u: displacement vector

G: stress tensor

$$\nabla \times \mathrm{u} = \begin{vmatrix} \mathbf{i} & \mathbf{j} & \mathbf{k} \\ \partial_{\mathbf{x}} & \partial_{\mathbf{y}} & \partial_{\mathbf{z}} \\ U_{\mathbf{x}} & U_{\mathbf{y}} & U_{\mathbf{z}} \end{vmatrix} = \begin{pmatrix} \partial_y U_z - \partial_z U_y \\ \partial_z U_x - \partial_x U_z \\ \partial_x U_y - \partial_y U_x \end{pmatrix}$$

$$\nabla \cdot \mathrm{U} = \partial_x \mathrm{U}_x + \partial_y \mathrm{U}_y + \partial_z \mathrm{U}_z$$

Wang et al. , 2003

Elasticity

- Elastic properties of homogenous isotropic elastic material are uniquely determined by two elastic moduli, by knowing of them other elastic moduli can be calculated

$$E = \frac{\sigma_{11}}{\varepsilon_{11}} = \frac{\mu(3\lambda + 2\mu)}{\lambda + \mu} : \text{Young's modulus}$$

$$\nu = -\frac{\varepsilon_{33}}{\varepsilon_{11}} = \frac{\lambda}{2(\lambda + \mu)} : \text{Poisson's ratio}$$

$$K = \lambda + (2/3)\mu : \ \text{Bulk modulus}$$

$$\sigma_{ij} : \text{stress tensor} \qquad \varepsilon_{ij} : \text{strain tensor}$$

- Of the five elastic parameters λ, μ, ν, E, K only two are independent

Ranalli, 1995

SAREDU Remote Sensing Education Initiative

Flowchart of coseismic deformation analysis using InSAR observations

Taking unwrapped interferogram

↓

Downsampling of the data for computational efficiency

↓

Selection of the dislocation model (e.g. Okada model) and applying forward modeling or a nonlinear optimization algorithm to find best fitting model

↓

Discretizing the fault plane into a number of small patches (subfaults) and estimating slip distribution

SAREDU Remote Sensing Education Initiative

Non-linear inversion and model parameter estimation

- The relation between observed surface deformation and fault parameters can be expressed by a matrix equation:

$$d = G(m) + e$$

d=observed deformation
m= fault parameters
G= Green function relating fault parameters to surface displacement (Okada, 1985)
ε= observation error

- Optimal model parameters are obtained by either forward modelling (trial and error) or nonlinear inversion techniques (e.g. Cervelli et al., 2001)

Deformation modeling

- Forward Model

$$d = G(m)$$

displacement
Green function
Source parameters

- Inverse Model

$$m = G^{-1}(d)$$

- Source parameters include:
  - length(L), width (W), strike (α), Dip (δ), depth of the reference point on the fault plane (d), strike-slip component (U1) & dip-slip component (U2).

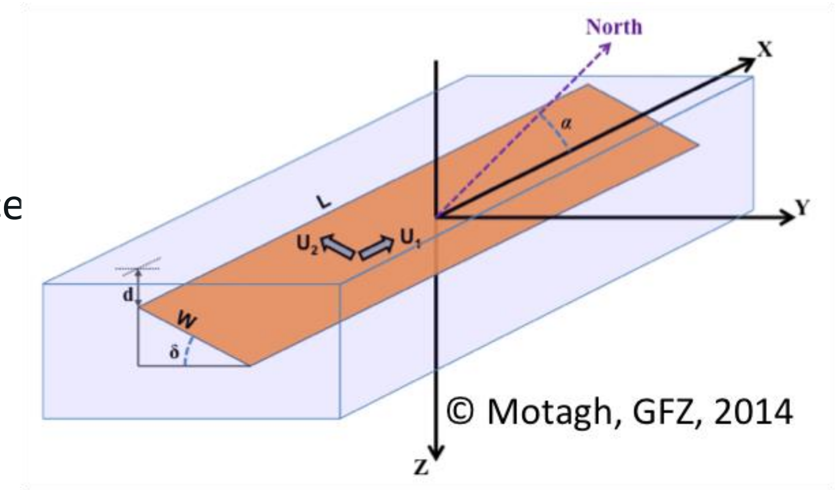

SAREDU Remote Sensing Education Initiative

Fault Slip distribution

- For a fixed geometry, fault slip distribution can be parameterized as a discrete grid of rectangular elements, in which the slip within each element is assumed to be uniform
- The slip vector is a linear function of surface displacements

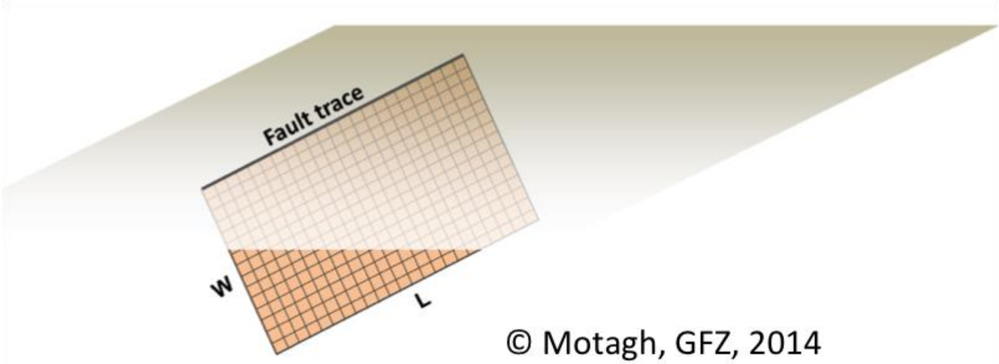

© Motagh, GFZ, 2014

d=*G*s
d= vector of surface displacement
G= Green function from Okada (1985)
s= slip vectors

Du et al., 1992

Fault Slip distribution

- Fault slip distribution inversion poses a regularized inverse problem
- The solution is obtained by minimizing a combination of fit to data, control on the initial model (s_0) and model roughness ($Hs=d_0$)

$$\phi=\{\text{Data misfit}\} + \alpha^2 \{\text{initial model}\} + \beta^2 \{\text{roughness}\}$$

$$f = \|\mathrm{Gs} - \mathrm{d}\|^2 + a^2 \|\mathrm{s} - \mathrm{s}_0\| + b^2 \|\mathrm{Hs} - \mathrm{d}_0\|$$

Du et al., 1992

SAREDU Remote Sensing Education Initiative

Error sources

- Ignoring error sources in InSAR observations might bias modeling results

- Main error sources in InSAR-derived coseismic deformation maps are inaccurate satellite orbit information, DEM errors, interferometric decorrelation, and unwrapping error

- Tropospheric phase delay is usually ignored for large earthquakes. For small and medium sized earthquakes the effect from atmospheric artifacts can be partly reduced by stacking

Error sources

- Baseline uncertainty

  It appears as a phase ramp and can be removed from coseismic interferograms by bi-linear interpolation

- DEM error

  It is a function of the perpendicular baseline of the interefrogram and topography of the imaged area (pairwise logic and use of small-baseline interferograms are recommended)

- Coherence loss and phase unwrapping error

  The coherence loss can be due to different factors causing temporal decorrelation or because of large deformation gradient (e.g. when a fault rupture reaches to the surface)

SAREDU Remote Sensing Education Initiative

Practical considerations

- Surface deformation detection of earthquakes depends on the size and depth of earthquakes. The earthquake should produce measurable surface deformation, above the detection threshold of InSAR technique (~ 0.5-1 cm).
- For small earthquakes (4.5 <M< 5.5) at shallow depths (< 10 km), deformation detection depends on the number of interferograms available for stacking in order to increase signal to noise ratio and mitigate atmospheric artifacts.

SAREDU Remote Sensing Education Initiative

InSAR-based catalogue of earthquakes

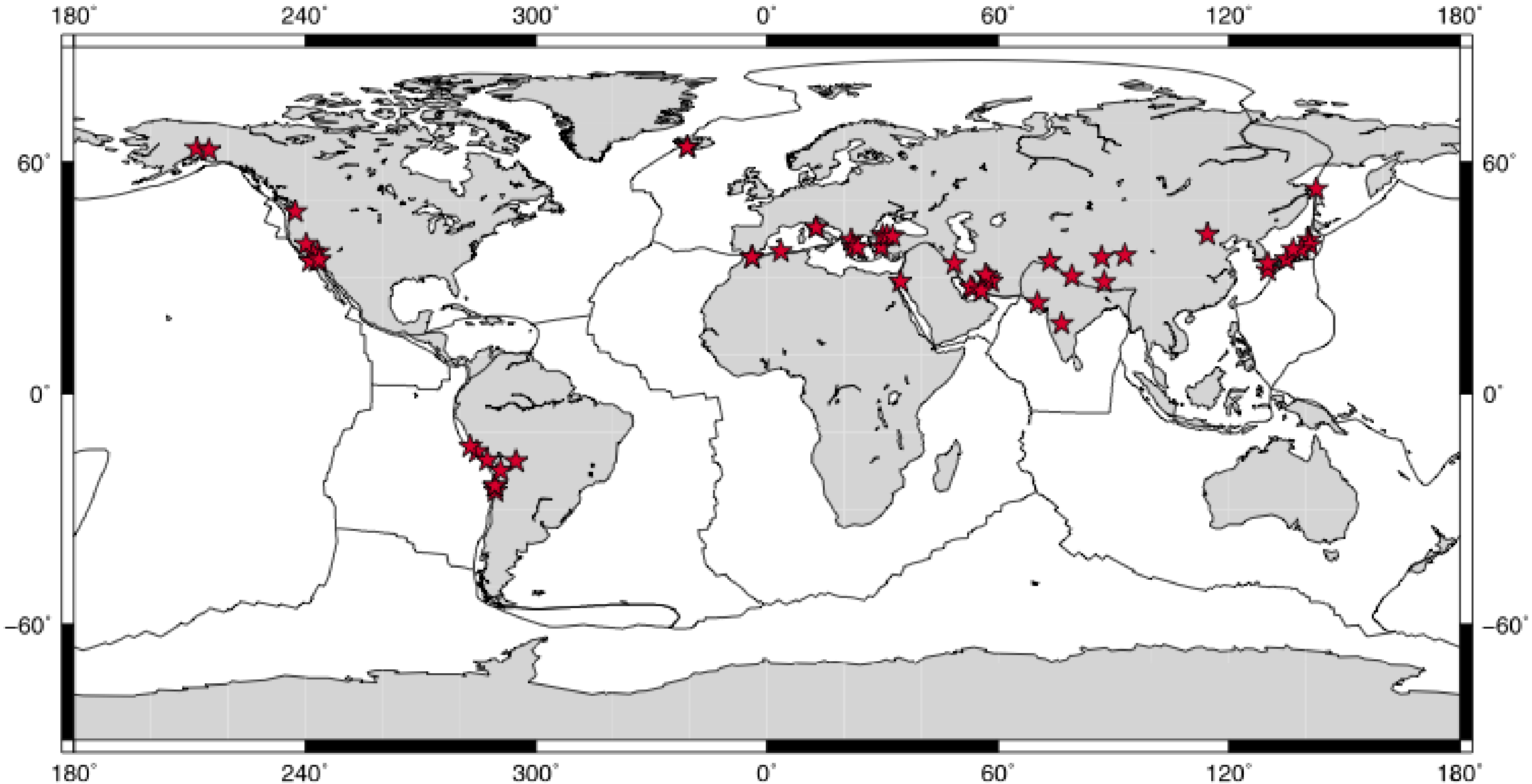

Geographical distribution of more than 50 earthquakes with magnitudes between Mw 5.0 and 8.5 and depth less than 60 km studied using InSAR between 1992 and 2012.

Weston et al., 2011

28 June 1992, Mw 7.3, Landers, California, earthquake

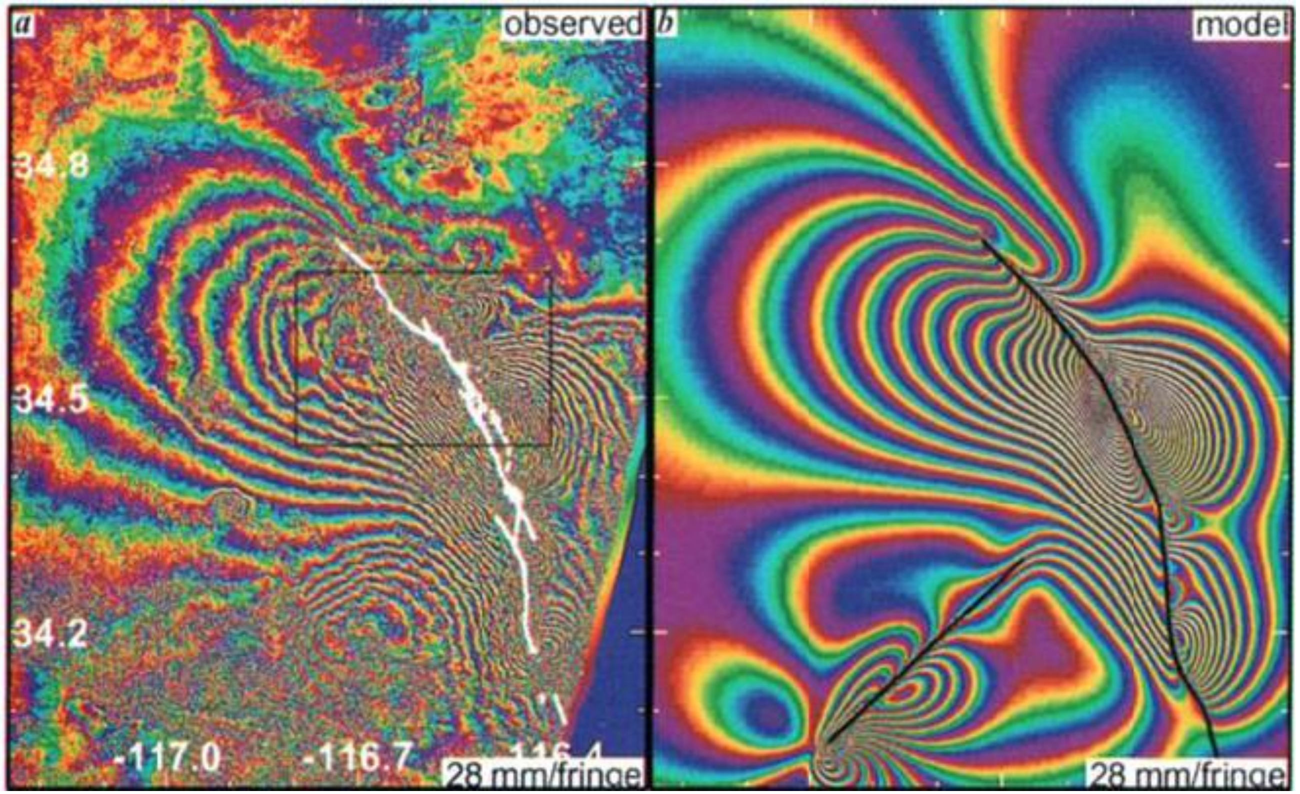

(a) Observed ERS1 interferogram between April 24, 1992 and June 18, 1993. White lines indicate coseismic surface rupture. (b) Modeled interferogram with black lines indicating fault patches derived from the elastic dislocation model.

Massonnet & Feigl, 1998

SAREDU Remote Sensing Education Initiative

16 October 1999, Mw 7.1, Hector Mine, California, earthquake

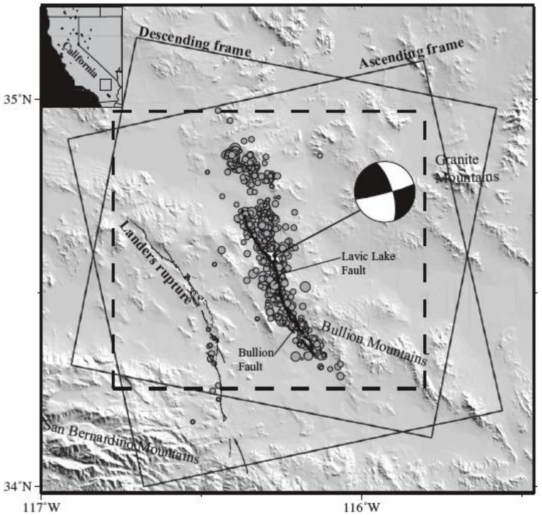

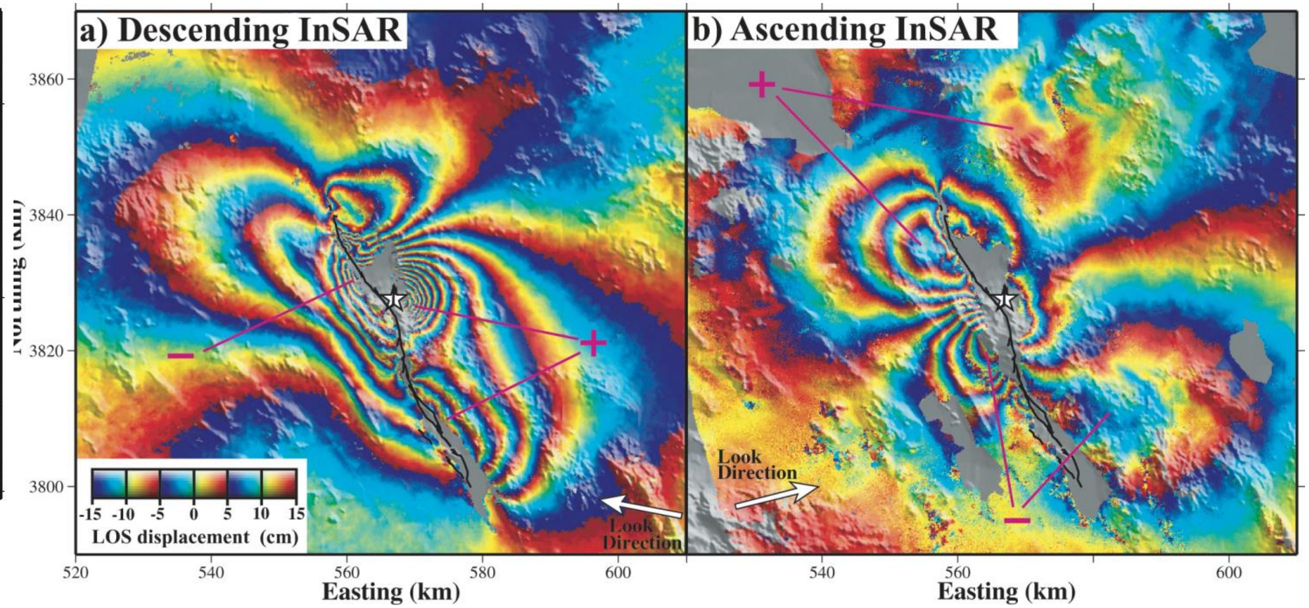

Dashed rectangle shows the area covered by the interferograms on the right. Black thick line shows surface rupture of the 1999 Hector mine earthquake.

ERS2	Master scene	Slave scene	Temporal baseline	Perpendicular baseline
Descending	15 Sept. 1999	20 Oct. 1999	35 days	21 m
Ascending	12 Nov. 1995	21 Nov. 1995	4 years	55 m

Jónsson et al., 2002

SAREDU Remote Sensing Education Initiative

Fault slip models of the 1999 Hector Mine earthquake

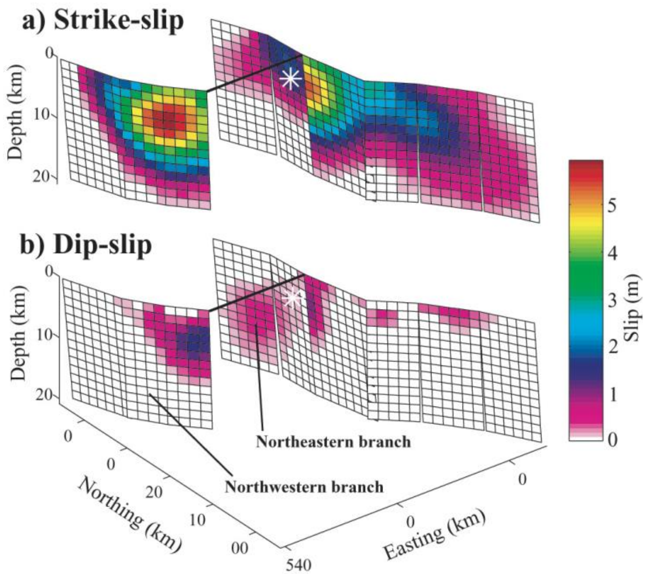

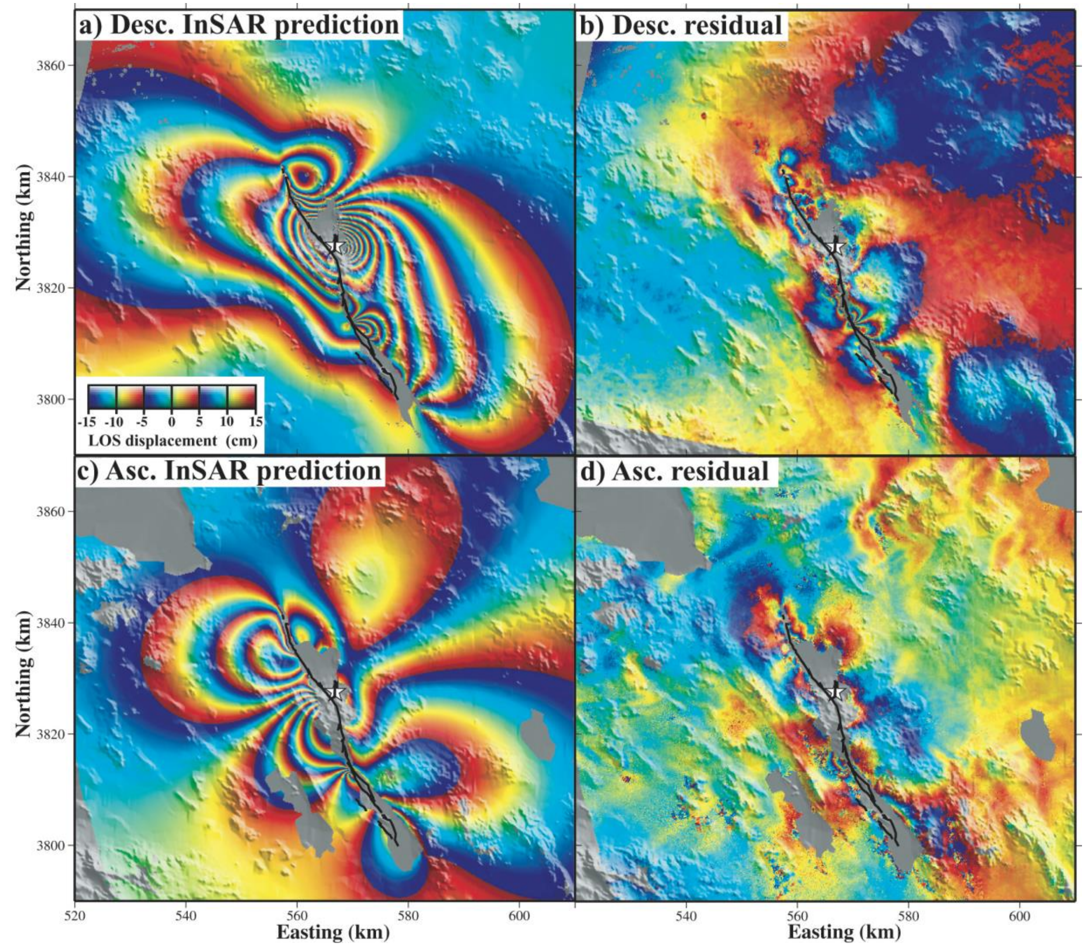

- Complex geometry, multiple strands
- Fault slip concentration at shallow depth (6 -10 km)
- Significant vertical fault slip

Jónsson et al., 2002

SAREDU Remote Sensing Education Initiative

The Mw 7.9, 3 Nov. 2002, Denali Fault earthquake

	Date 1	Date 2	θ*	α†	$B_\perp$‡
ifm1	29-Oct-02	22-Nov-02	27.7	− 14.5	110
ifm2	20-Oct-02	13-Nov-02	39.5	− 169.1	− 10
ifm3	11-Oct-02	4-Nov-02	47.0	− 9.1	158
ifm4	18-Sept-02	5-Nov-02	23.4	− 15.3	22
ifm5	15-Oct-02	8-Nov-02	34.2	− 12.3	105

*Incidence angle at scene center.
†Satellite Azimuth (angle between the satellite ground track and local north).
‡Perpendicular baseline (in meters).

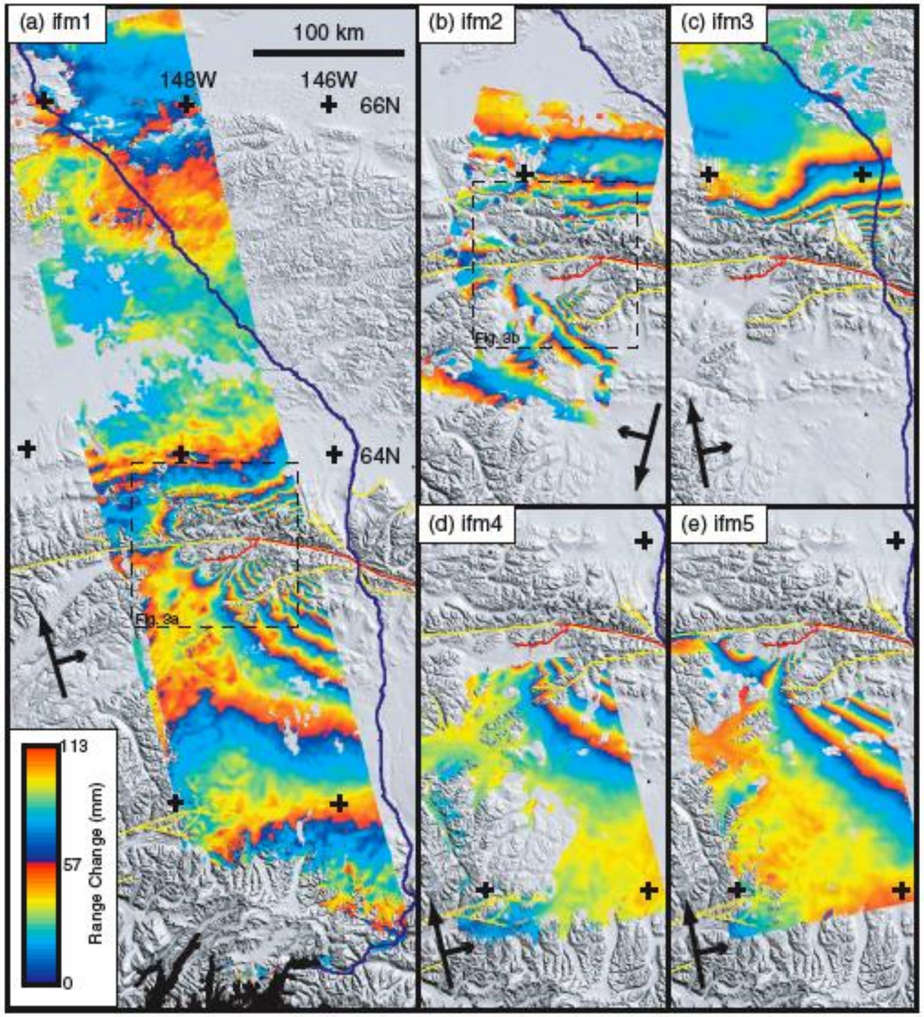

- SAR data from Canadian Radarsat-1 satellite
- Yellow lines are mapped faults and red lines are surface rupture of 3 Nov. 2002 earthquake

Wright et al., 2004

SAREDU Remote Sensing Education Initiative

Fault slip model of the 2002 Denali earthquake

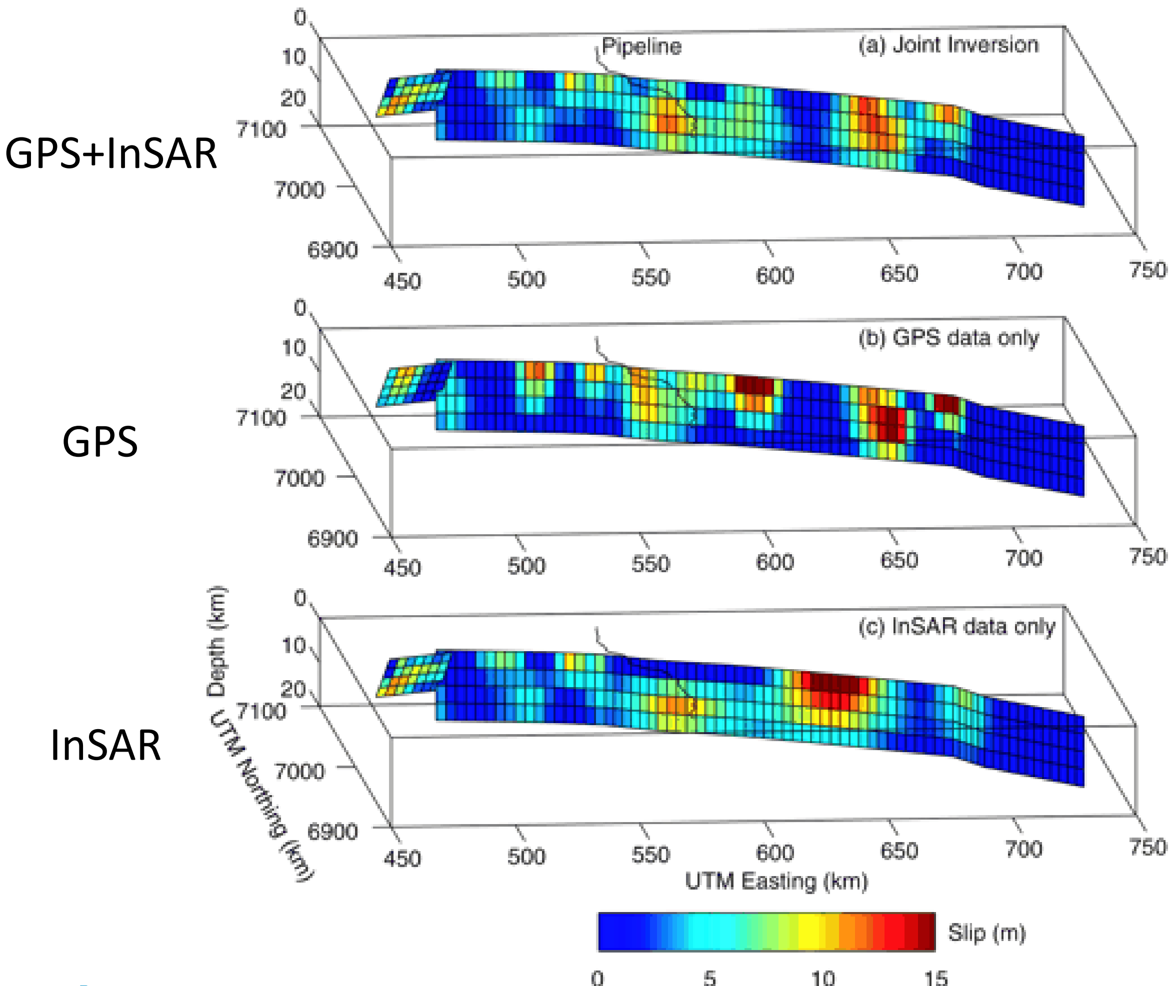

- Complex slip distribution
- Spatial variation of slip along strike
- Two main areas of high slip east of the pipeline crossing: (1) peak slip of ~ 12 m at a depth of ~ 10 km with slip of about 7 m at the surface (2) approx. 12 m of slip at the surface about 80 km east of the pipeline crossing
- The slip is generally below 5 m west of the pipeline crossing

Wright et al., 2004

26 December 2003, Mw 6.5, BAM, Iran, earthquake

Descending Envisat - 3 December 2003 to 7 January 2004

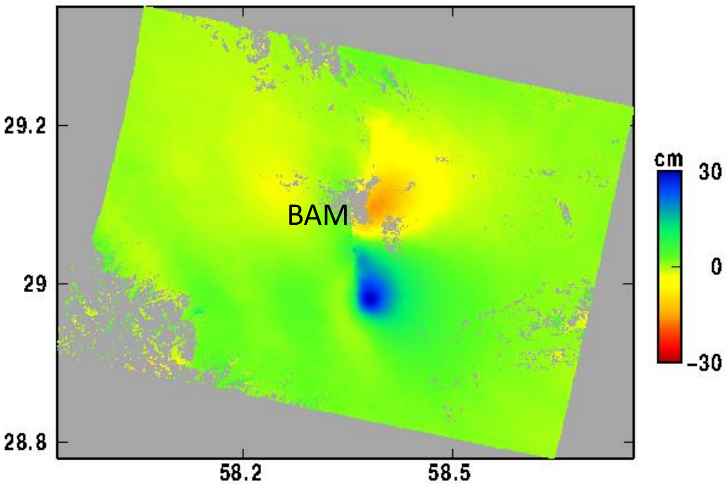

↗ The InSAR data can be best explained by a new near vertical right-lateral strike-slip fault rupturing an area of 11 by 8 km south of the city of BAM

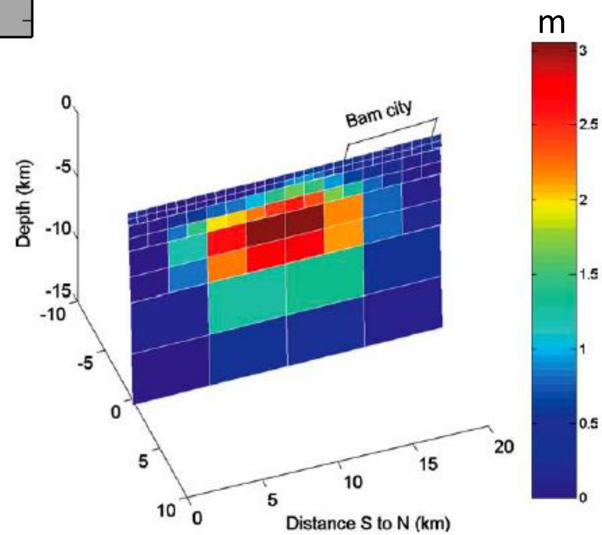

Ascending Envisat: 16 November 2003- 29 February 2004

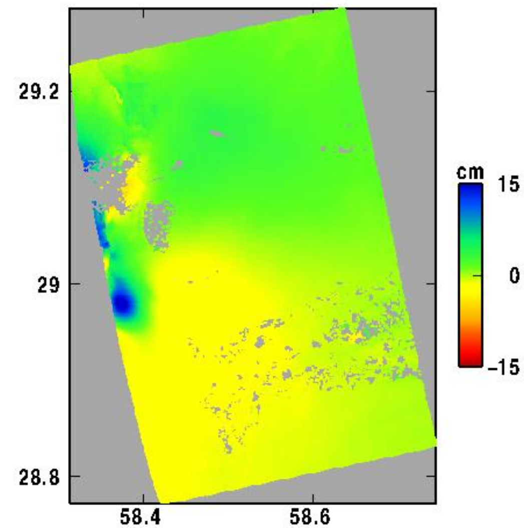

↗ Peak slip of ~ 3 m at a depth of 3-5 km

↗ The InSAR data rule out slip on previously mapped BAM fault between BAM and Baravat!

Motagh et al., 2006

SAREDU Remote Sensing Education Initiative

15 August 2007, Mw 8.0, Pisco, Peru, earthquake imaged by Wide Swath (WS) Envisat

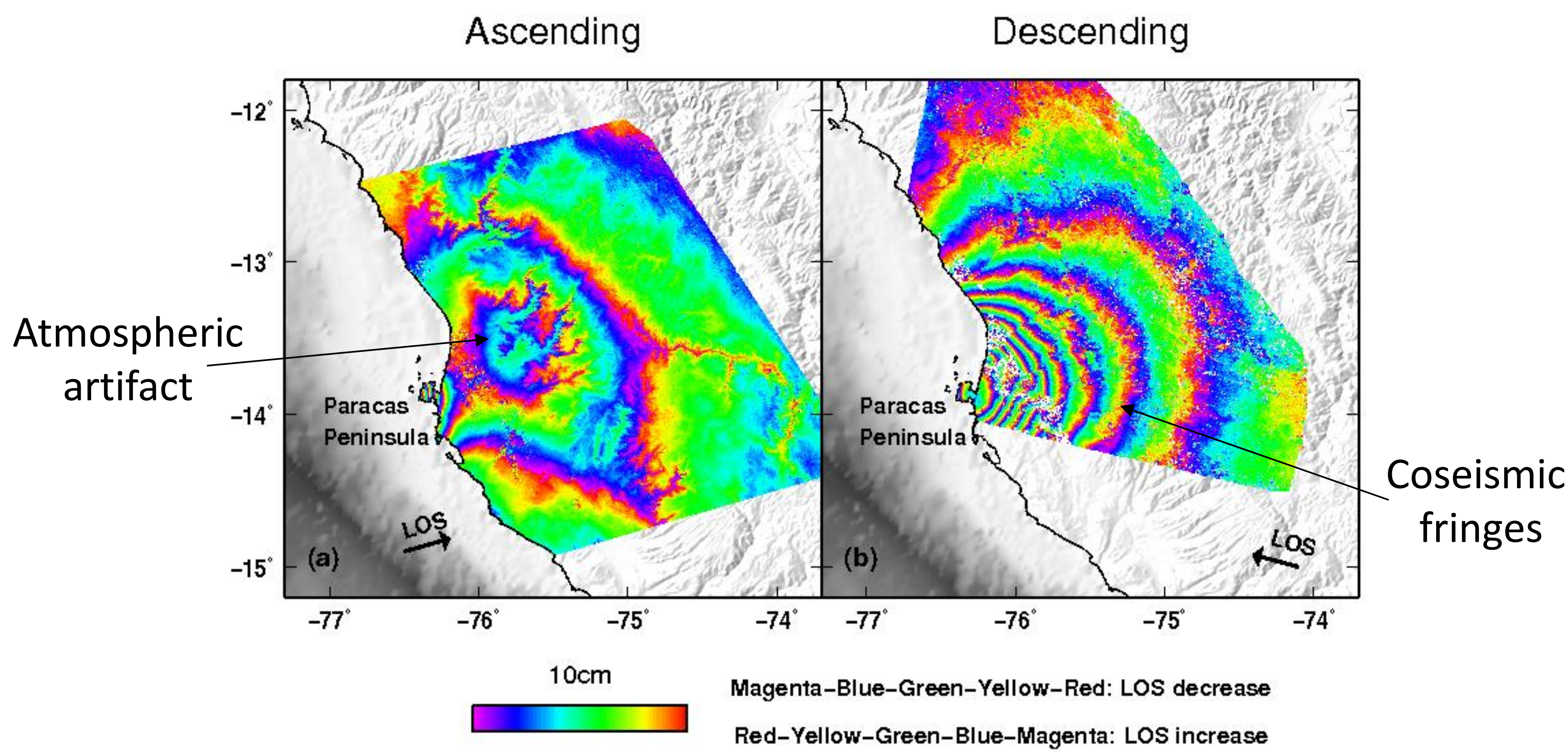

Motagh et al., 2008a

Fault slip model of the 2007 Pisco earthquake

- The 2007 Pisco event ruptured part of a known seismic gap along the Peruvian margin, partially filled the gap
- Homogenous slip distribution
- Peak slip of ~ 5-6 m at a depth of ~ 18-20 km offshore
- Depth of faulting is confined to less than 40 km depth

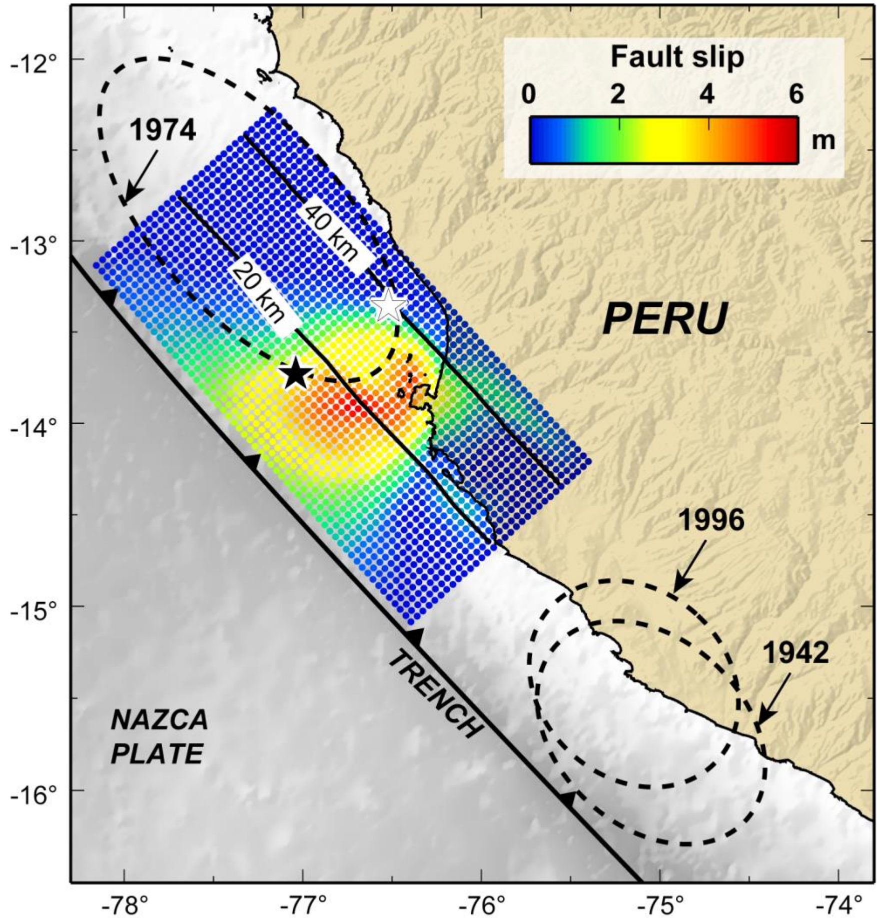

Motagh et al., 2008a

14 Nov 2007, Mw 7.8, Tocopilla, Chile earthquake

Descending, I2 Mode (incidence angle θ ~ 23°), track 368

Descending, I2 Mode (incidence angle θ ~ 23°), track 96

Ascending, Wide Swath (WS) Mode, 23° <θ<31°, track 361

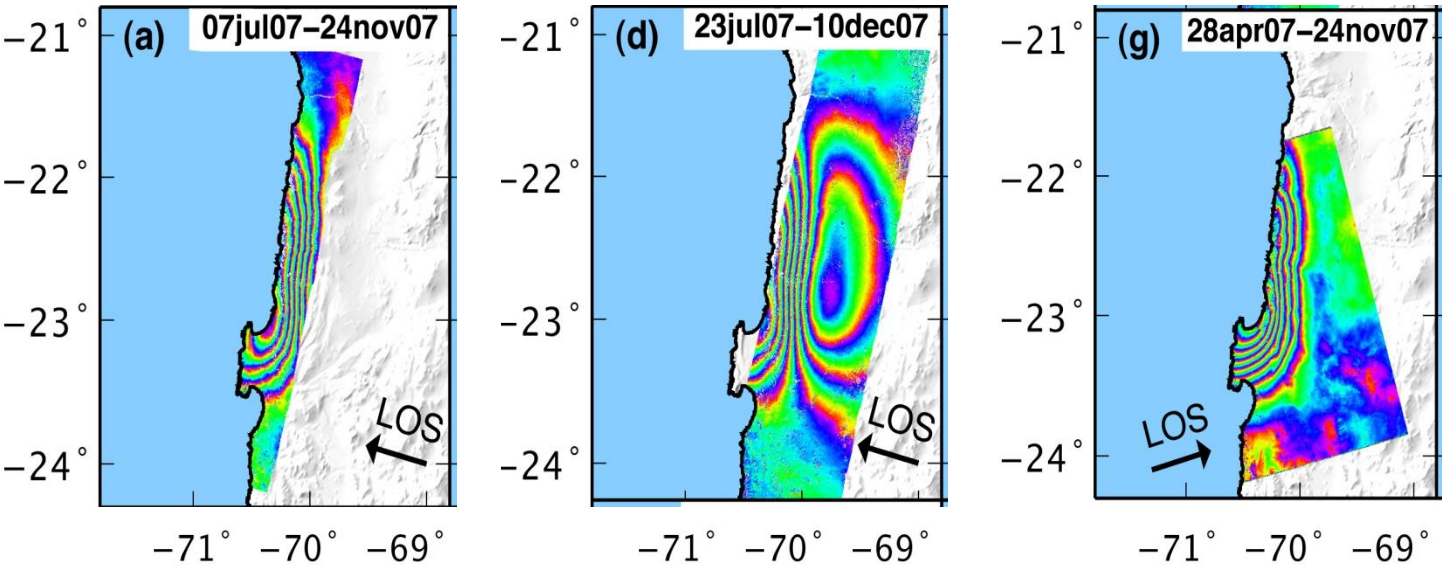

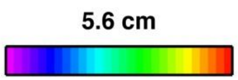

Magenta–Blue–Green–Yellow–Red: LOS decrease
Red–Yellow–Green–Blue–Magenta: LOS increase

The transition zone from LOS uplift to subsidence around 70° W in Figure (d) is called hinge line. It corresponds to the downdip termination of the ruptured area on the subducting interface.

Motagh et al., 2010

14 Nov 2007, Mw 7.8, Tocopilla, Chile earthquake

- The main slip is concentrated on two asperities, the largest being located in the southern part of the rupture area and north of the Mejillones peninsula
- Maximum slip of about 2.5 m
- Depth of faulting between 30 and 50 km
- Relation to the 1995 Antofagasta earthquake: The 1995 Antofagasta earthquake occurred on the shallower part of the plate interface between 10 and 40 km depth (orange contour on the right figure), while the 2007 Tocopilla earthquake occurred on the deeper part of the interface zone between 30 and 50 km depth

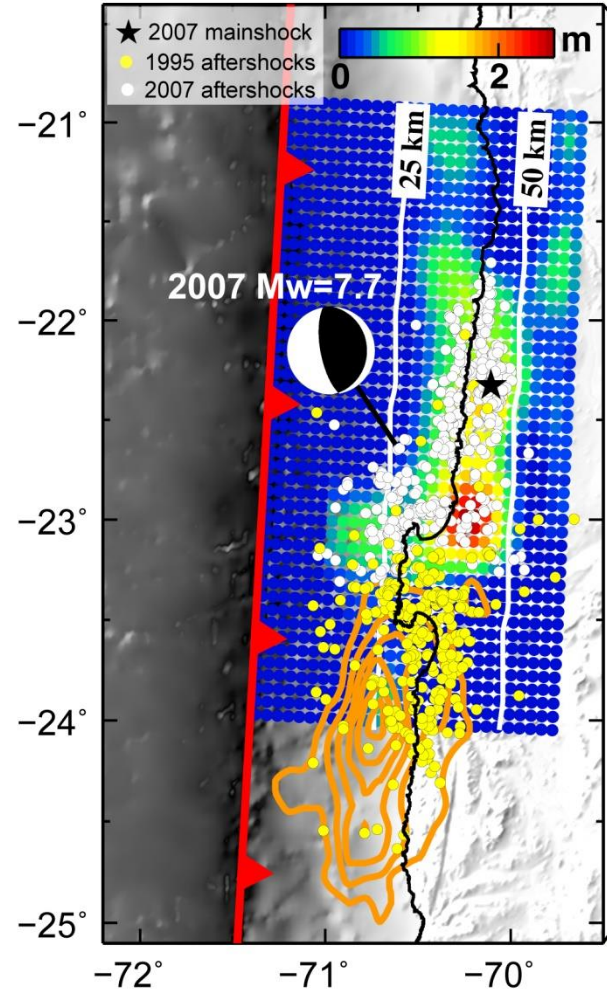

Motagh et al., 2010

SAREDU Remote Sensing Education Initiative

6 April 2009, Mw 6.3, L'Aquila, Italy earthquake

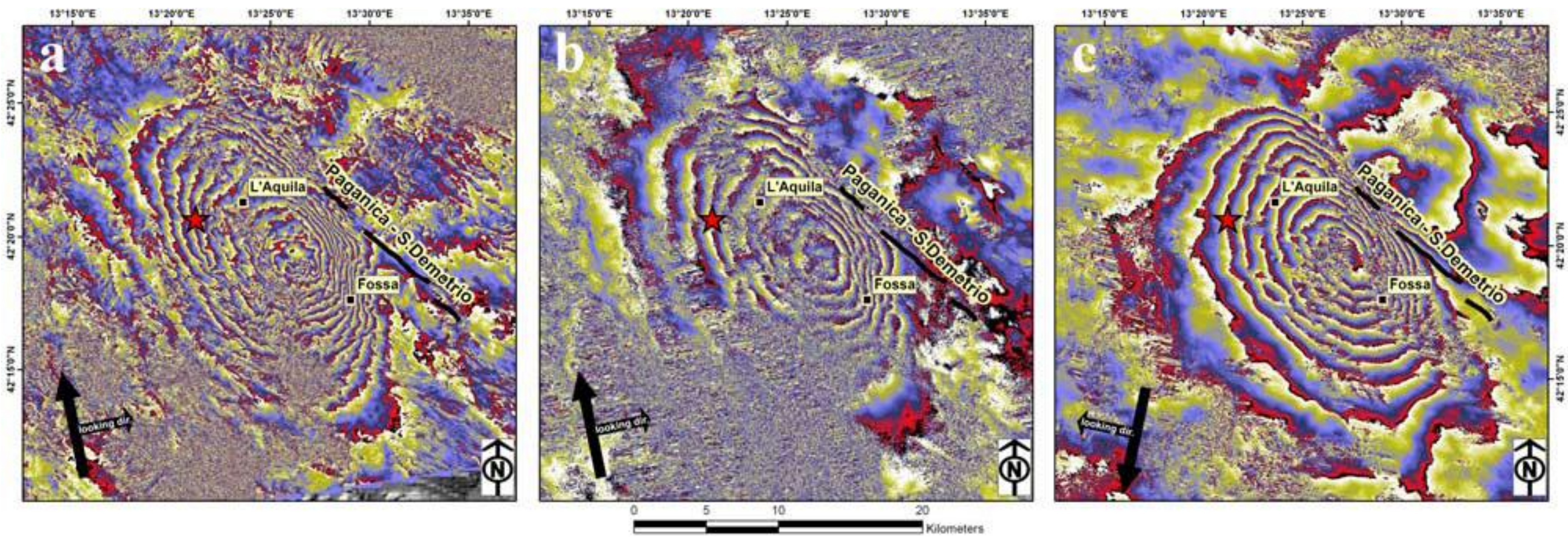

Differential interferogram from (a) COSMO-SkyMed ascending (04/04/2009-12/04/2009), (b) Envisat ascending (11/03/2009-15/04/2009), and (c) Envisat descending (27/04/2008-12/04/2009).
The black line is Paganica-S. Demetrio fault.

Atzori et al., 2009

Distributed-Slip model

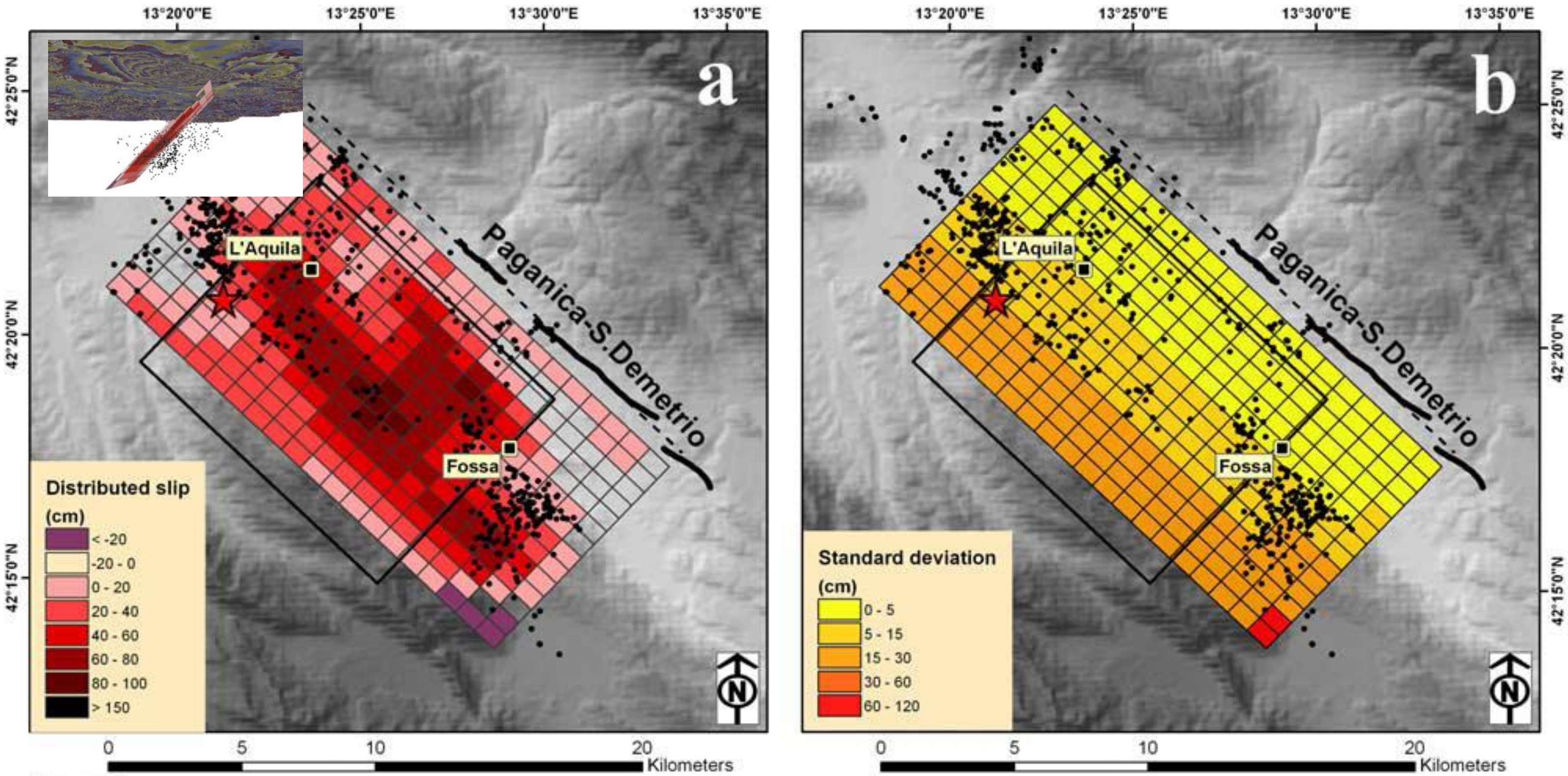

(a) Slip distribution estimated by linear inversion of Envisat and COSMO-SkyMed data. The inset on the upper left shows a 3D view of the fault plane. (b) Uncertainty of the slip model

Atzori et al., 2009

SAREDU Remote Sensing Education Initiative

4 September 2010, Mw 7.1, Darfield (Canterbury), New Zealand, earthquake

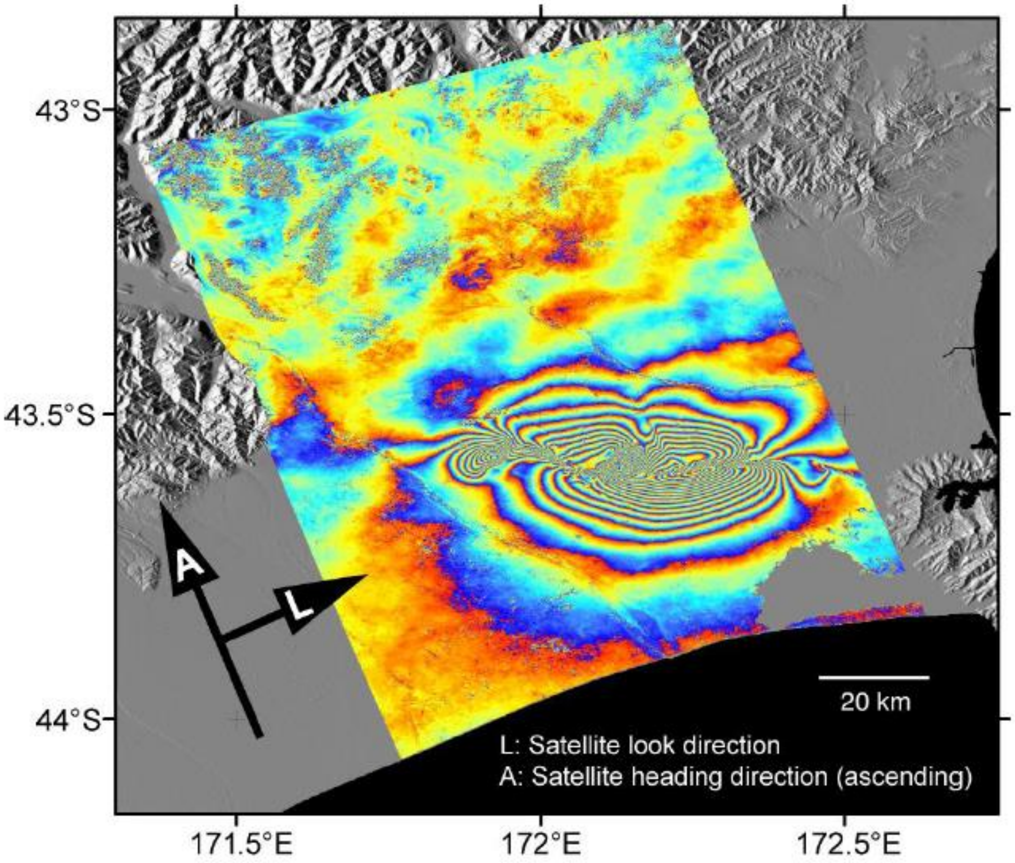

- ALOS L-band interferogram constructed from images on 13th August and 28th September, 2010
- Each color cycle indicates ~ 12 cm of ground motion in the line-of-sight to the satellite

Beavan et al., 2010

Fault slip model of the 2010 Darfield earthquake

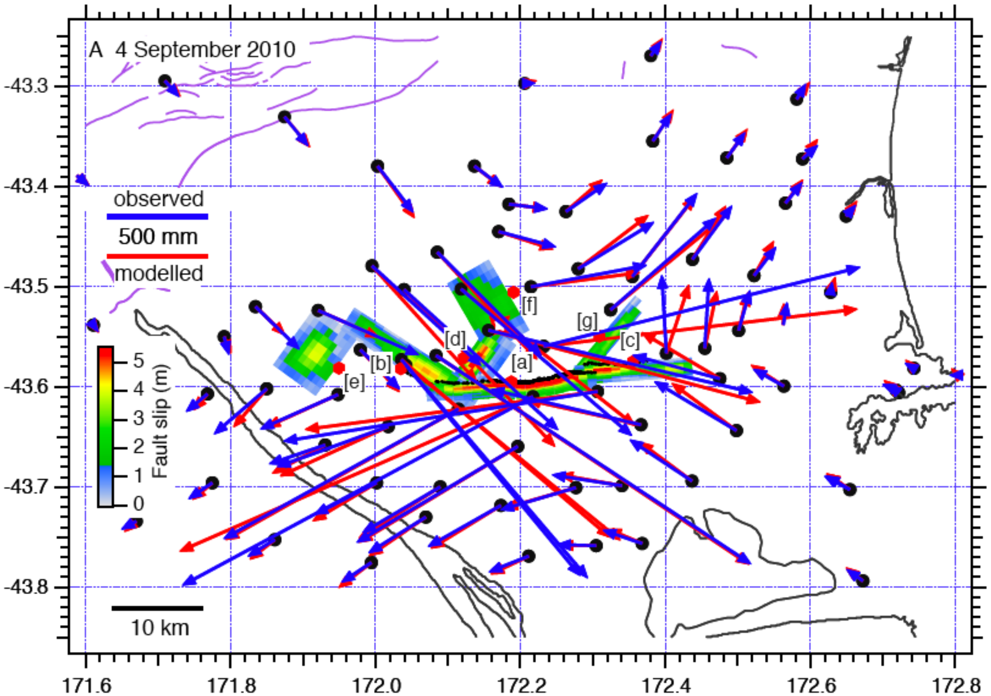

Observed (blue) and modelled (red) displacements at GPS sites, and the slip model derived from the joint inversion of GPS and InSAR data (ALOS & Envisat). Black line is the surface rupture of the 2010 Darfield earthquake.

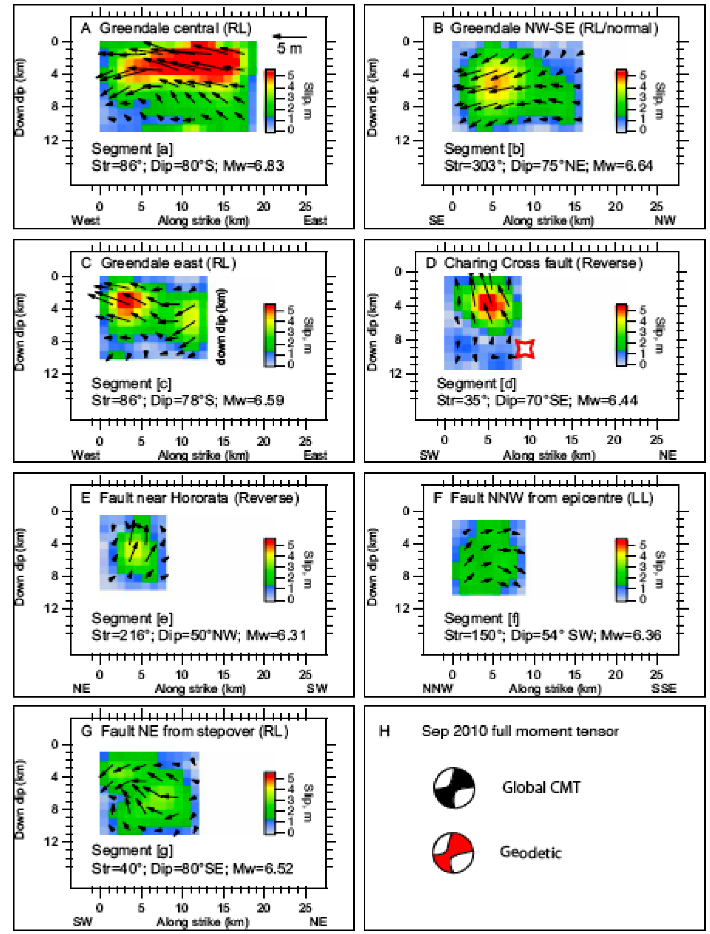

Slip magnitude and direction on each of the fault segments modelled as active during the earthquake.

SAREDU Remote Sensing Education Initiative

Beavan et al., 2012

Locating Small earthquakes: Zagros mountains

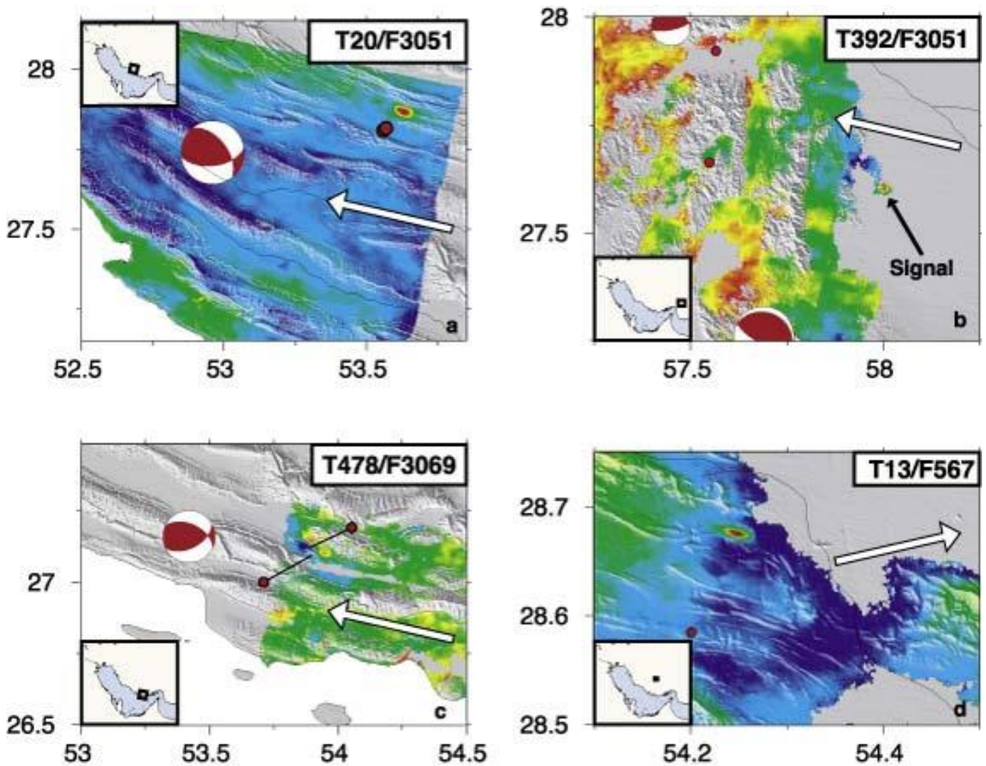

Date	T/F	InSAR M_w/Z
97/05/05	478/3069	5.4/4.4
97/09/18	478/3069	5.0/3.5
98/10/01	13/567	4.7/0.7
99/04/30	20/3051[b]	5.3/3.2
Unknown	392/3051	4.8/2.0

T/F: track and frame from ERS1/2 for each earthquake; M_w: magnitude; Z: depth to the center of the fault plane in kilometers inferred from inversion of InSAR data

(a) the 1999/04/30 earthquake, (b) an unknown signal, (c) the 1997/05/05 and 1997/09/18 earthquakes, and (d) the 1998/10/01 earthquake, all overlain on topography, with the satellite-to-ground LOS direction indicated by the white arrow. Red circles show teleseismically determined locations and focal mechanisms.

Lohman & Simons, 2005

Locating Small earthquakes: 29 June 1992, Ms 5.4, Little Skull Mountain (LSM) earthquake

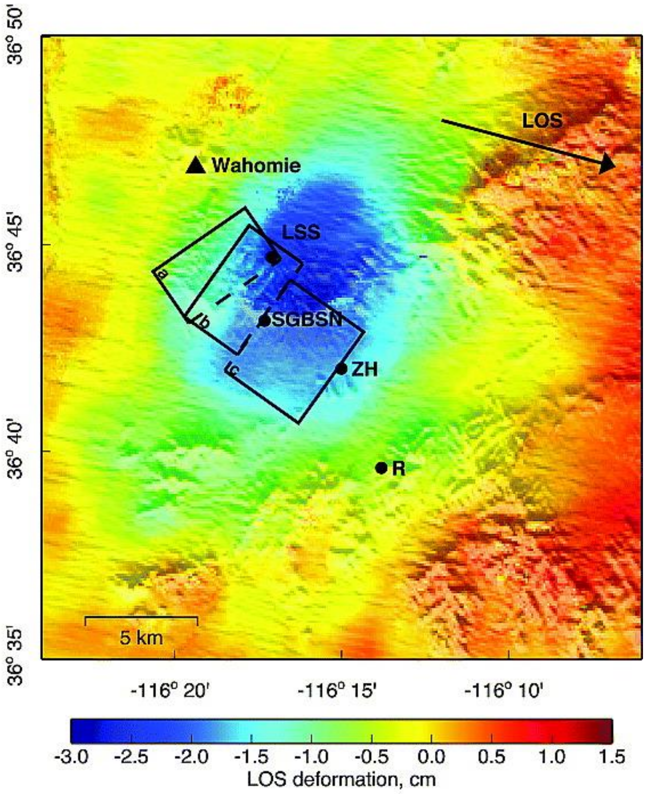

Average surface displacements induced by the 1992, M_s 5.4, Little Skull Mountain (NV) earthquake. The results obtained by stacking 3 ERS1 interferograms spanning 24/4/1992-14/05/1993, 24/4/1992-18/06/1993 and 24/4/1992-24/09/1995. Dots and rectangles indicate various published models for this event.

Lohman et al., 2002

SAREDU Remote Sensing Education Initiative

2005 Kashmir earthquake: Sub-pixel correlation of Envisat SAR imagery

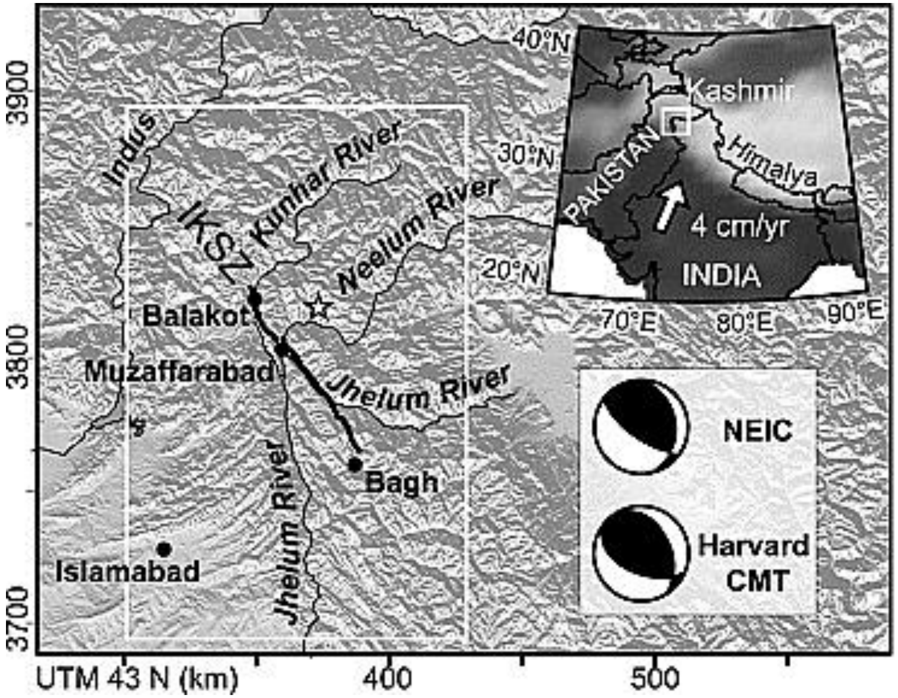

Shaded DEM of the Kashmir region. The star is the epicenter of the October 2005 earthquake. Thick black line is the fault rupture.

- Mw 7.6, 8th October 2005
- 80,000 deaths
- Mountainous environment with high topography and steep slopes, causing decorrelation for using conventional InSAR
- **Sub-pixel correlation in azimuth and range direction provides an alternative for classical InSAR in this situation**

Pathier et al., 2006

SAREDU Remote Sensing Education Initiative

2005 Kashmir earthquake: Sub-pixel correlation of Envisat SAR imagery

Direction	Track	Beam	Pre-Event	Start Date	End Date	⊥ Baseline, m
Ascending	270	I6	5	25-06-2005	12-11-2005	60
Ascending	499	I6	4	19-09-2005	24-10-2005	270
Descending	463	I2	20	17-09-2005	26-11-2005	90

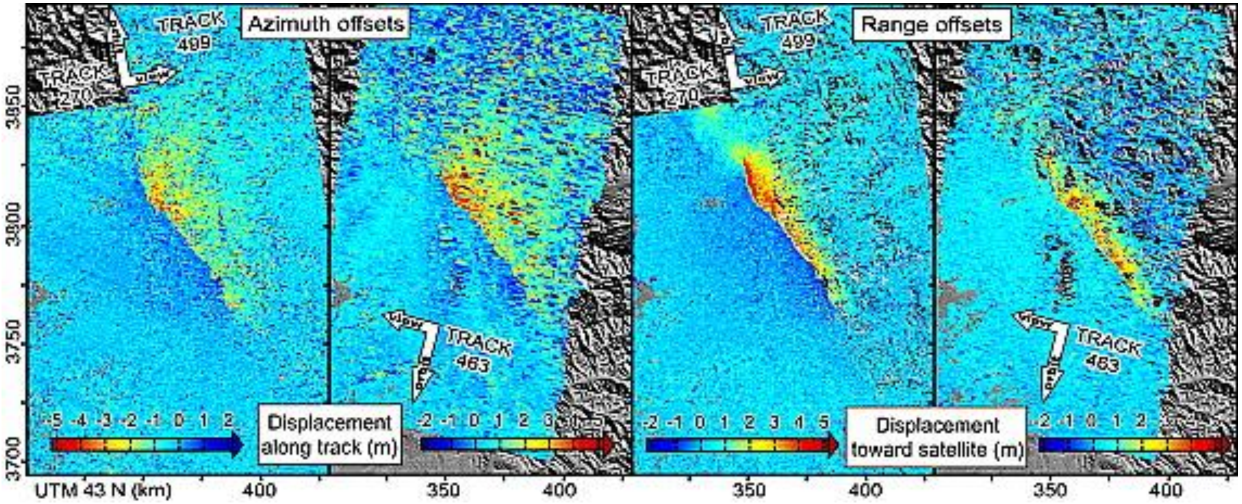

Pathier et al., 2006

- Azimuth and range offset measurements from ASAR Envisat pairs listed on the Table.
- Sharp discontinuity at the center of the image corresponds to surface deformation at the highly deformed area between hanging wall to the east and footwall to the west.
- Coseismic displacement field is consistent with a NE-dipping thrust fault.

Benefit of InSAR

- **Better constrain on the source model and earthquake location**

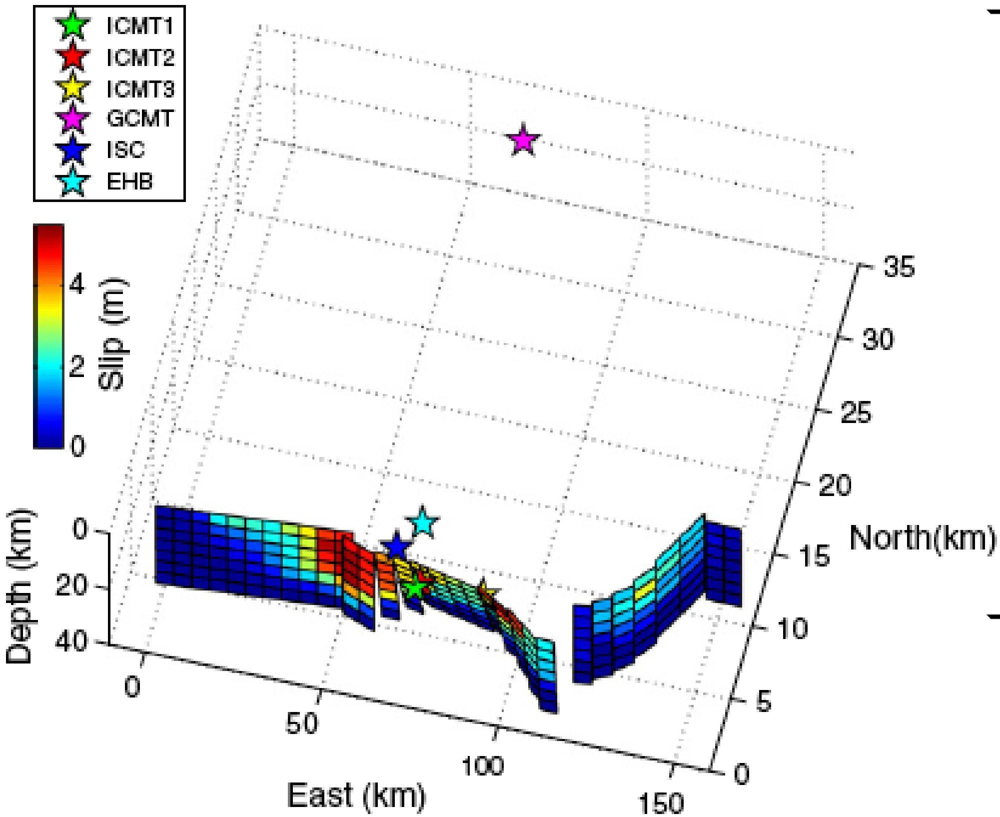

- Fault slip model of the 1999 Izmit earthquake from Cakir et al. (2003) with ICMT1 refers to the centroid location inferred from that study. ICMT2 and ICMTs refer to the centroid locations from other studies that used InSAR for the inversion. The remaining starts refer to earthquake locations extracted from seismic catalogues

- The GCMT location derived from seismic observations is 30 km away from the modeled fault plane!

Weston et al., 2012

Non-unique kinematic models

- The fault slip models are highly non-unique depending on the optimization technique, processing strategy, and constraints that are used in the inversion

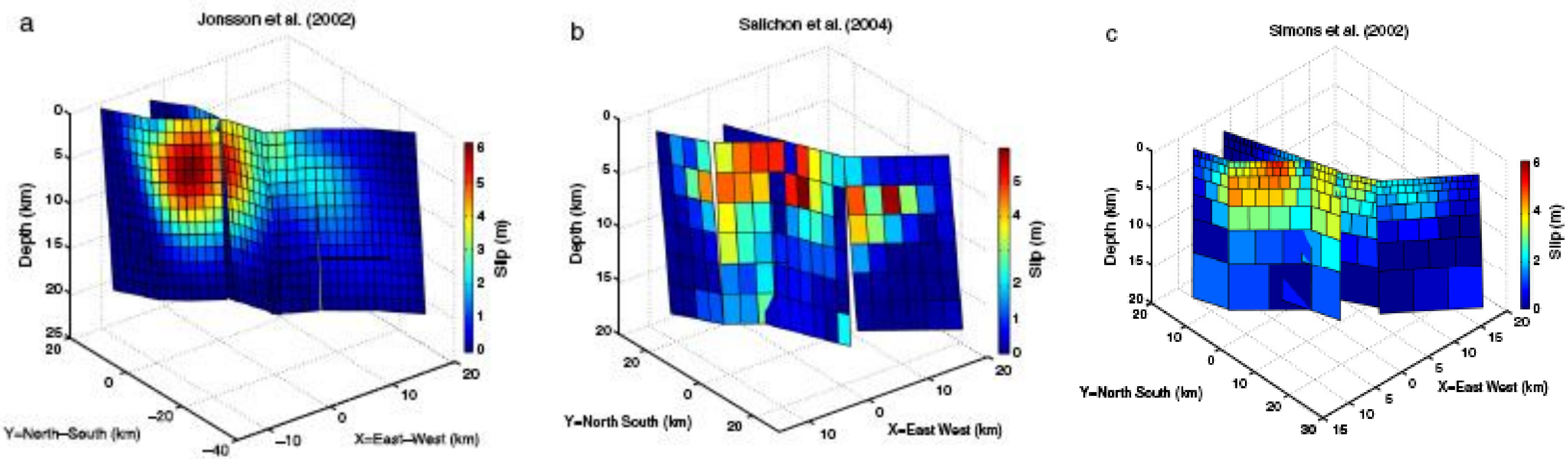

Different slip models for the 1999 Hector Mine earthquake from (a) joint inversion of InSAR and GPS data, (b) joint inversion of InSAR, GPS and teleseismic data, (c) joint inversion of GPS and InSAR data

Weston et al., 2012

Tools for dislocation modeling

- **EDGRN/EDCMP**

  -FORTRAN code for calculating co-seismic static deformation based on the dislocation theory (Wang et al. 2003).

  -The software can be downloaded

  ftp://ftp.gfz-potsdam.de/pub/home/turk/wang/edgrn+edcmp-code+input.zip

  -Or email to wang_AT_gfz-potsdam.de

- **SDM**

  -FORTRAN code for inverting co-seismic surface deformation data (GPS, InSAR, etc.) for fault slip distribution.

  -The software can be downloaded from

  ftp://ftp.gfz-potsdam.de/pub/home/turk/wang/sdm2011-code+input.rar

SAREDU Remote Sensing Education Initiative

Tools for dislocation modeling

- **Okada**

  -A Matlab program by François Beauducel to compute surface deformation due to a finite rectangular source in an elastic half-space earth model

  -The code can be downloaded from Matlab Central

  http://www.mathworks.com/matlabcentral/fileexchange/25982-okada--surface-deformation-due-to-a-finite-rectangular-source

MathWorks

Simulation using EDGRN/EDCMP: strike-slip fault

Fault parameters:
Length = 11 km
Width = 8 km
X_ref* = 0
Y_ref* = 0
Z_ref* = 25 m
Dip = 90˚
Strike = 358˚
Slip = 2 m

*X_ref (North), Y_ref (East) and Z_ref: coordinates of the upper reference point in EDGRN/EDCMP

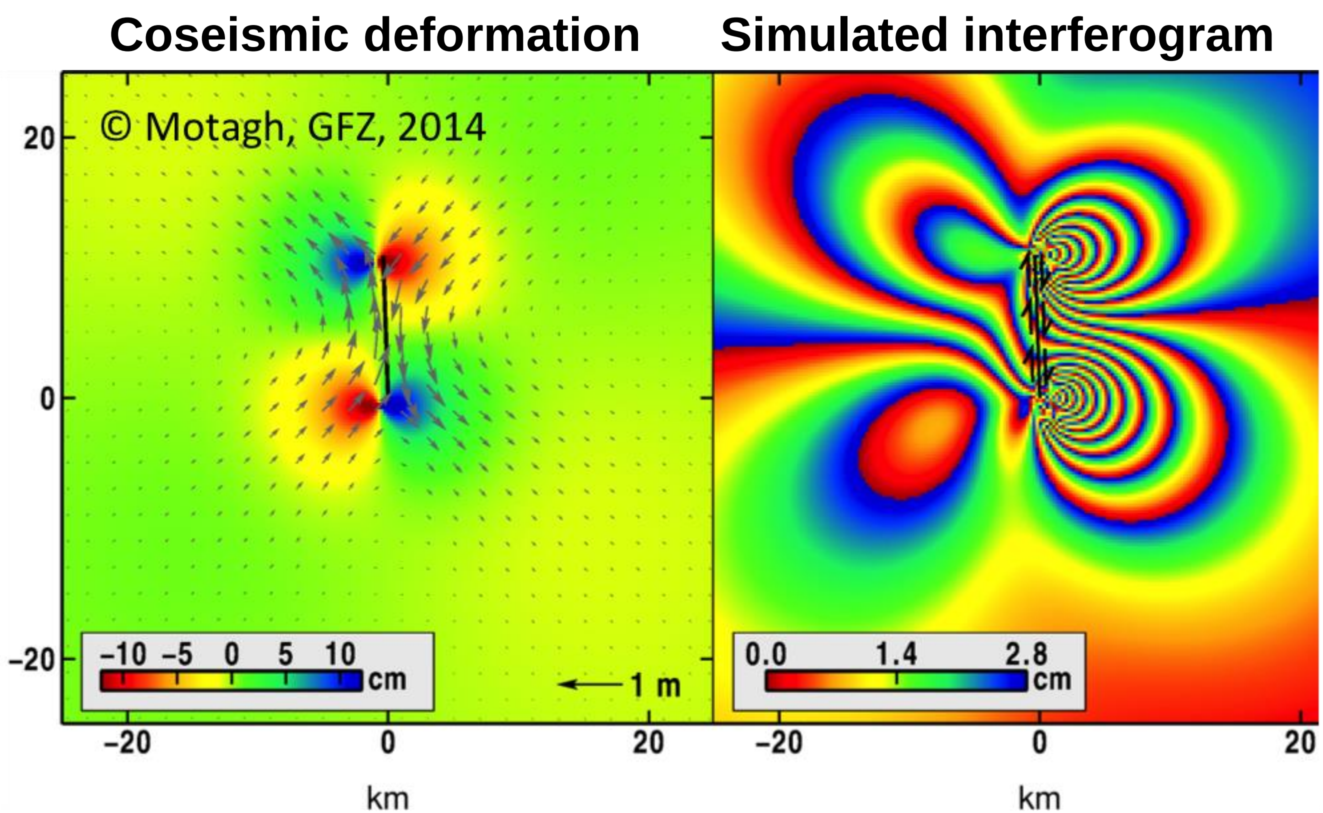

(left) Coseismic displacement in elastic half-space model. The color shows vertical deformation. (right) Simulated descending (heading angle 190˚, incidence angle 23˚) c-band interferogram.

SAREDU Remote Sensing Education Initiative

Simulation using EDGRN/EDCMP: Blind thrust faulting

Coseismic deformation **Simulated interferogram**

Fault parameters:
Length = 12.7 km
Width = 7.8 km
X_ref * = 10 km
Y_ref* = -10 km
Z_ref* = 4.4 km
Dip = 47°
Strike = 161°
Slip = 1.95 m
Rake= 89°

*X_ref (North), Y_ref (East)& Z_ref: coordinates of the reference point in EDGRN/EDCMP

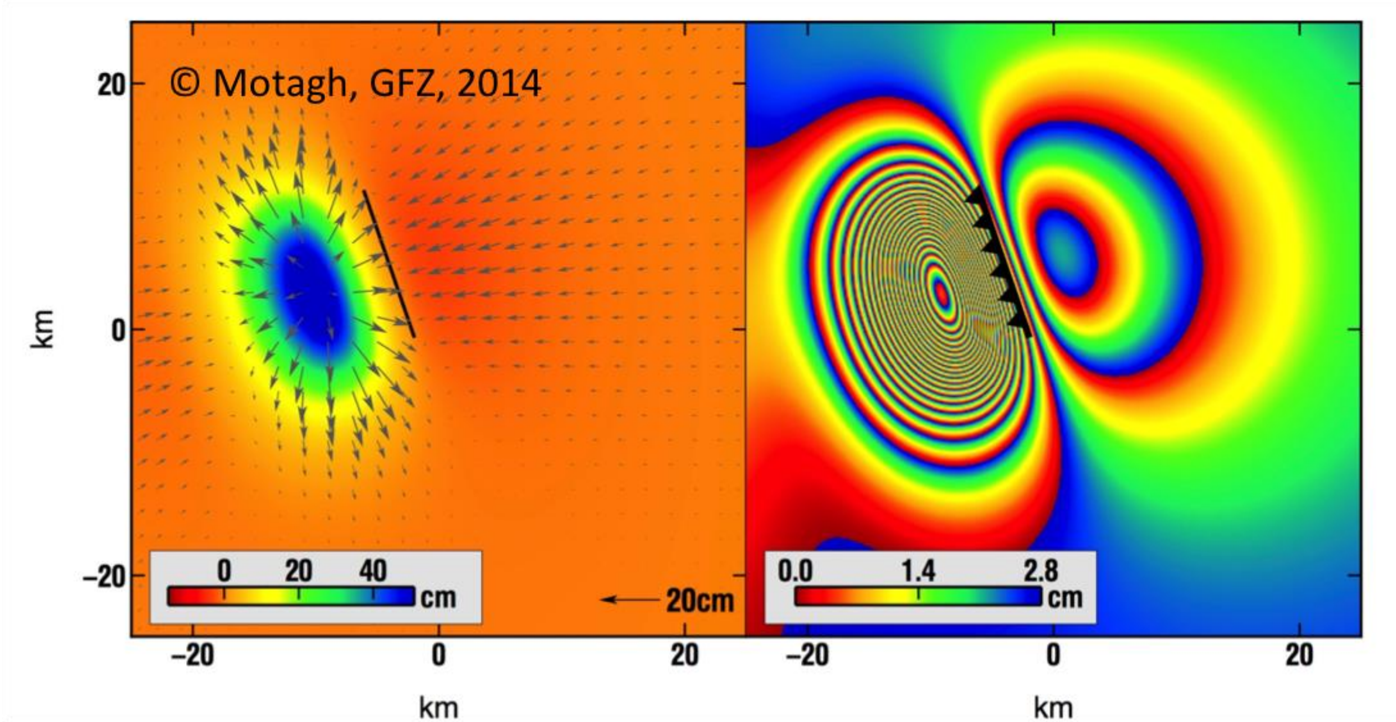

(left) Coseismic displacement in elastic half-space model. The color shows vertical deformation. (right) Simulated C-band wrapped interferogram with fringe spacing of 28 mm. Fault parameters are taken from Parsons et al. (2006).

SAREDU Remote Sensing Education Initiative

Structure

- Introduction to Plate Tectonics
- InSAR and earthquakes
- InSAR and postseismic deformation
- InSAR and interseismic deformation
- InSAR and volcano deformation
- InSAR and landslides
- InSAR and anthropogenic deformation

  [see also Module 3101: Anthroposphere – SAR Interferometry]

SAREDU Remote Sensing Education Initiative

InSAR and postseismic deformation

- **Goal**
  - To understand the mechanism of transient response of the lithosphere to the sudden change of stresses caused by earthquakes

- **Data requirement and methodology**
  - Data: SAR images in single polarization
  - Techniques: Repeat-pass interferometry, stacking or advanced time-series methods such as SBAS and PS-InSAR to to improve signal to noise ratio in measuring large-scale postseismic deformation signal

- **Main Tools**
  - Afterslip, poroelastic rebound, viscoelastic relaxation

InSAR and postseismic deformation

- **Advantages**
  - Information on vertical displacement provided by InSAR is crucial in distinguishing between competing models of postseismic deformation operative after an earthquake
- **Error sources and limitations**
  - Atmospheric noise limits the capability to study large-scale postseismic deformation (e.g. viscoelastic deformation) using InSAR observations
  - Early transient postseismic signal might not be captured by InSAR observations because of satellite revisit time, in particular in missions with long revisit time
- **Outlook for future satellites**
  - Short revisit time of future SAR missions (e.g. Sentinel) allows for a better capturing of early transient postseismic deformation

Models of postseismic deformation

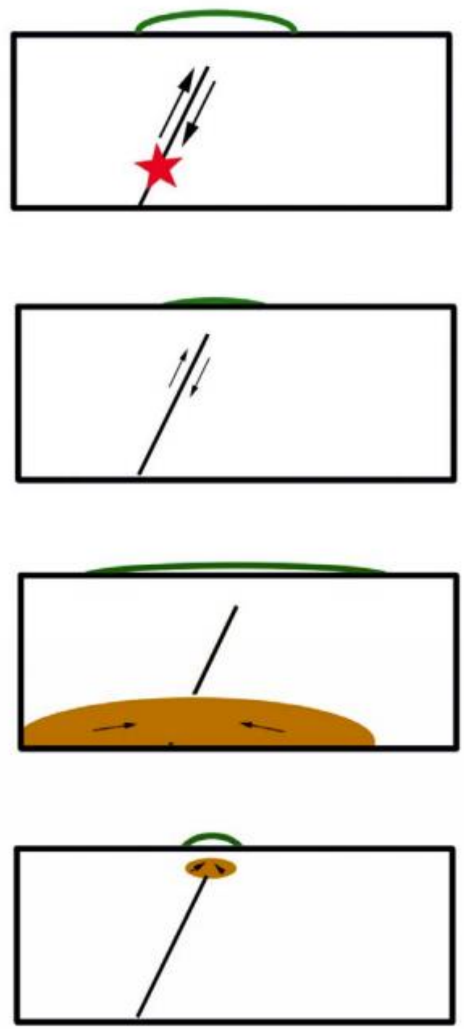

Coseismic deformation

After-slip
Continuous low-magnitude
slip along the ruptured fault
Simiar wavelength as coseismic

Viscous relaxation
Time dependent viscous
flow of the lower crust
broad wavelength deformation

Poro-elastic deformation
induced by pore-fluid flow
in response to stress changes
Shorth wavelength deformation

Wdowinski et al., 2011

SAREDU Remote Sensing Education Initiative

Afterslip

- **Process definition**
  - Slow continuation of the rupture process after the earthquake
- **Deformation pattern**
  - Similar to the coseismic deformation pattern but with a lower magnitude
- **Time-scale**
  - Shortly after the earthquake

Post-seismic motion following the 1997 Manyi (Tibet) earthquake

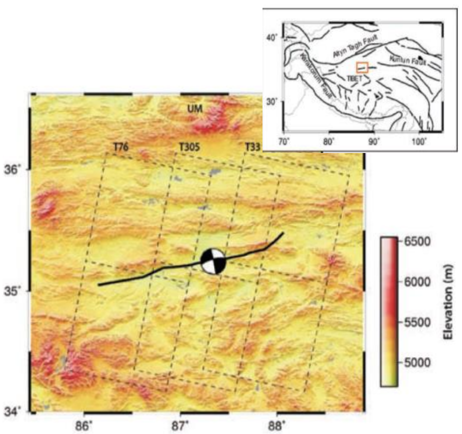

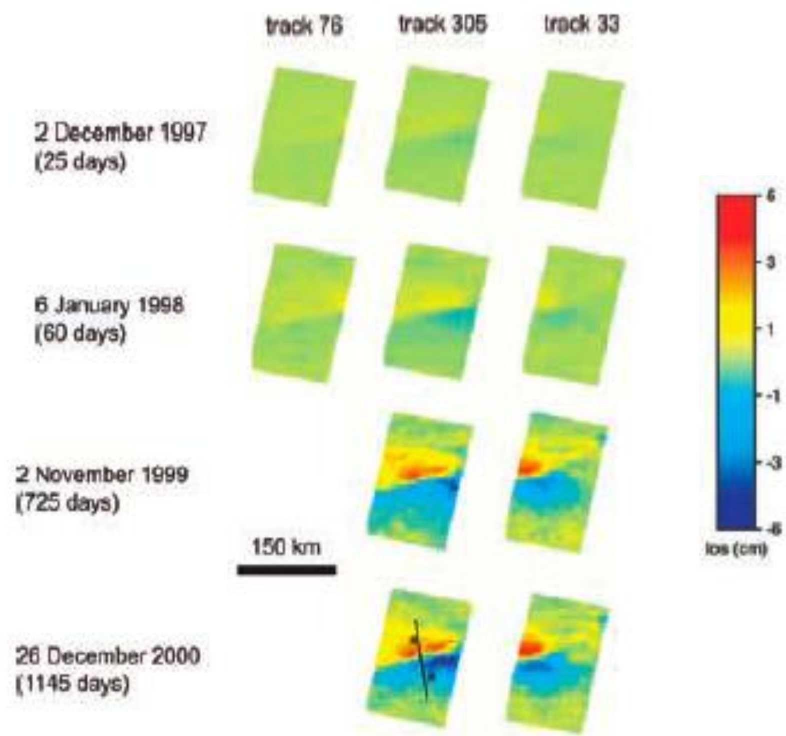

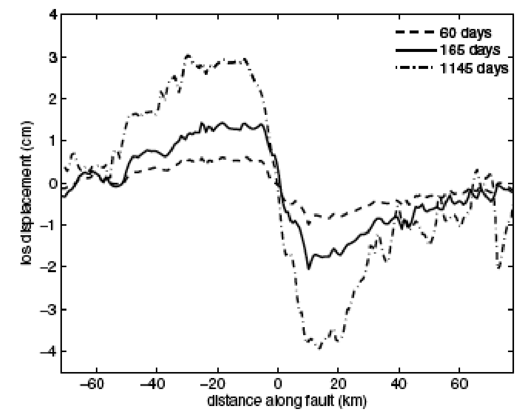

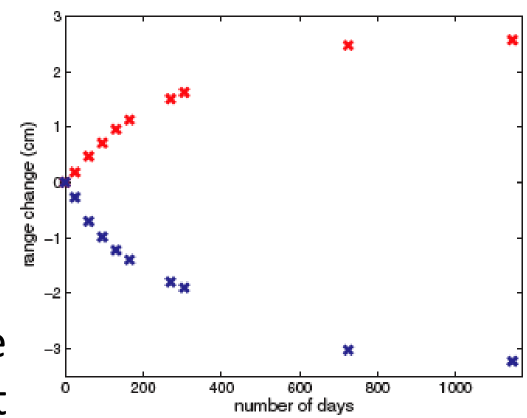

Post-seismic motion obtained from ERS2 time-series analysis. Line in bottom centre image marks location of profiles on the right figure (top), and stars denote locations of time-series curves shown on the right (bottom)

Ryder et al., 2007

Afterslip following the 1997 Manyi (Tibet) earthquake

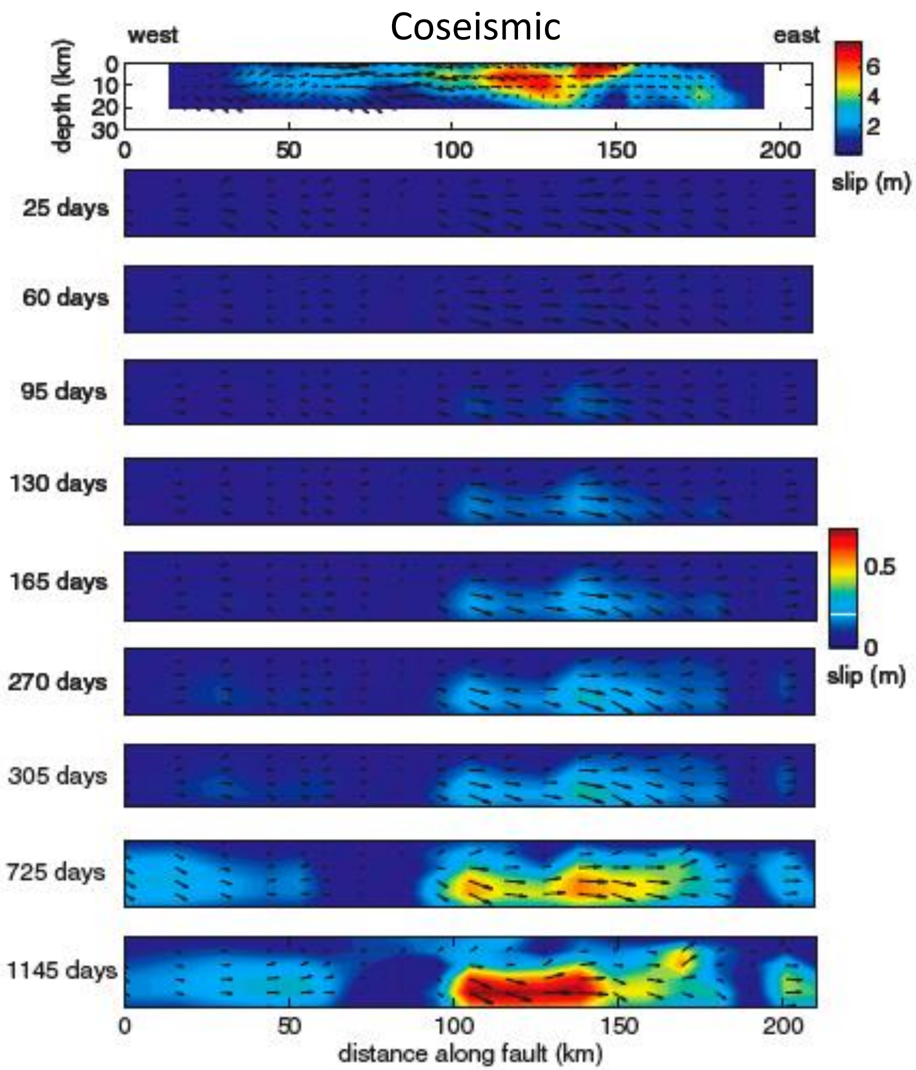

Ryder et al., 2007

SAREDU Remote Sensing Education Initiative

Afterslip following 6 April 2009, L'Aquilla, Italy, earthquake

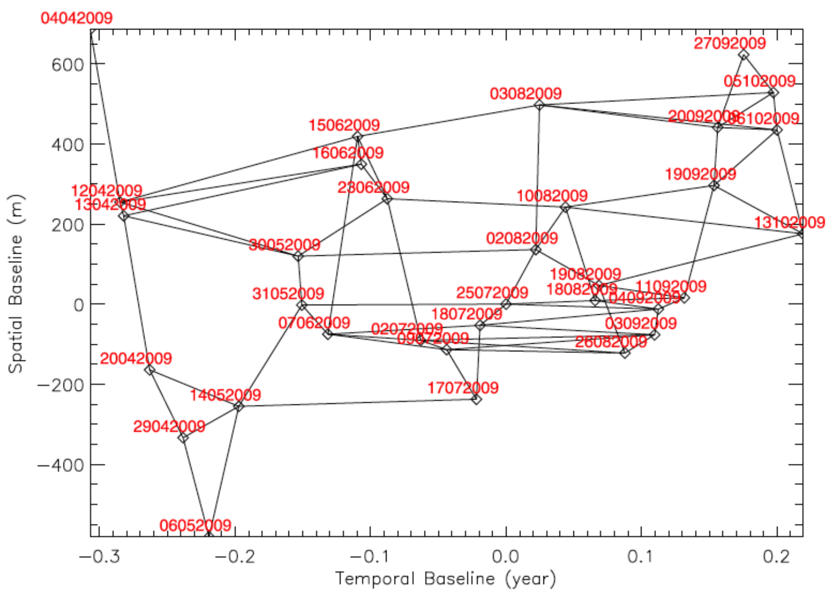

The network of X-band interferograms from COSMO-SkyMed (CSK) data used for the time-series analysis of postseismic ground deformation following 6 April 2009 earthquake

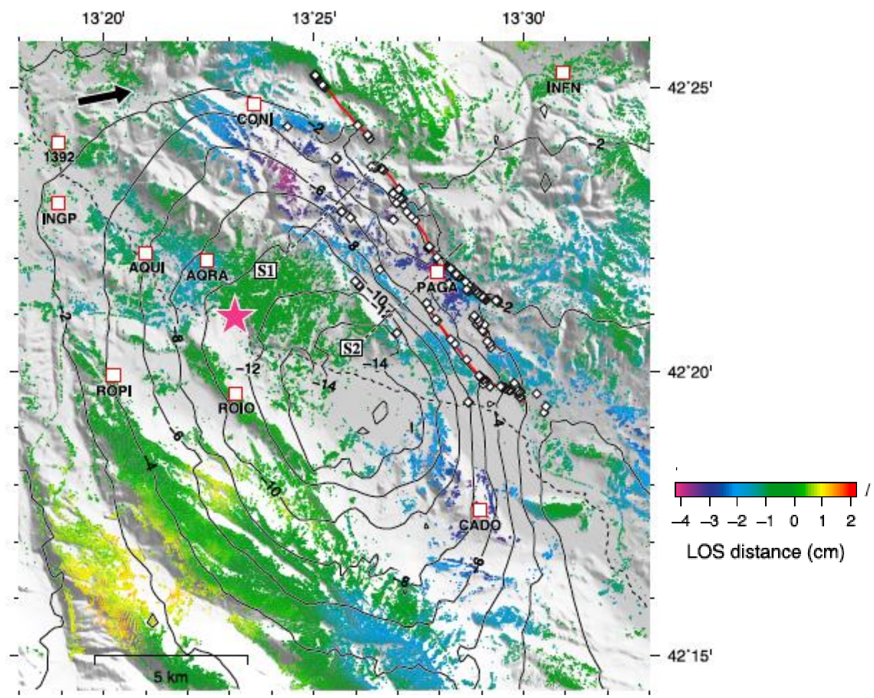

Postseismic deformation between 12 April 2009 and 5 October 2000 obtained by SBAS time-series analysis. The pink star indicates the epicenter. The contours represent coseismic displacement field between 4 April and 12 April 2009. Red lines are surface cracks after the earthquake.

SAREDU Remote Sensing Education Initiative

D'Agostino et al., 2012

Postseismic afterslip model

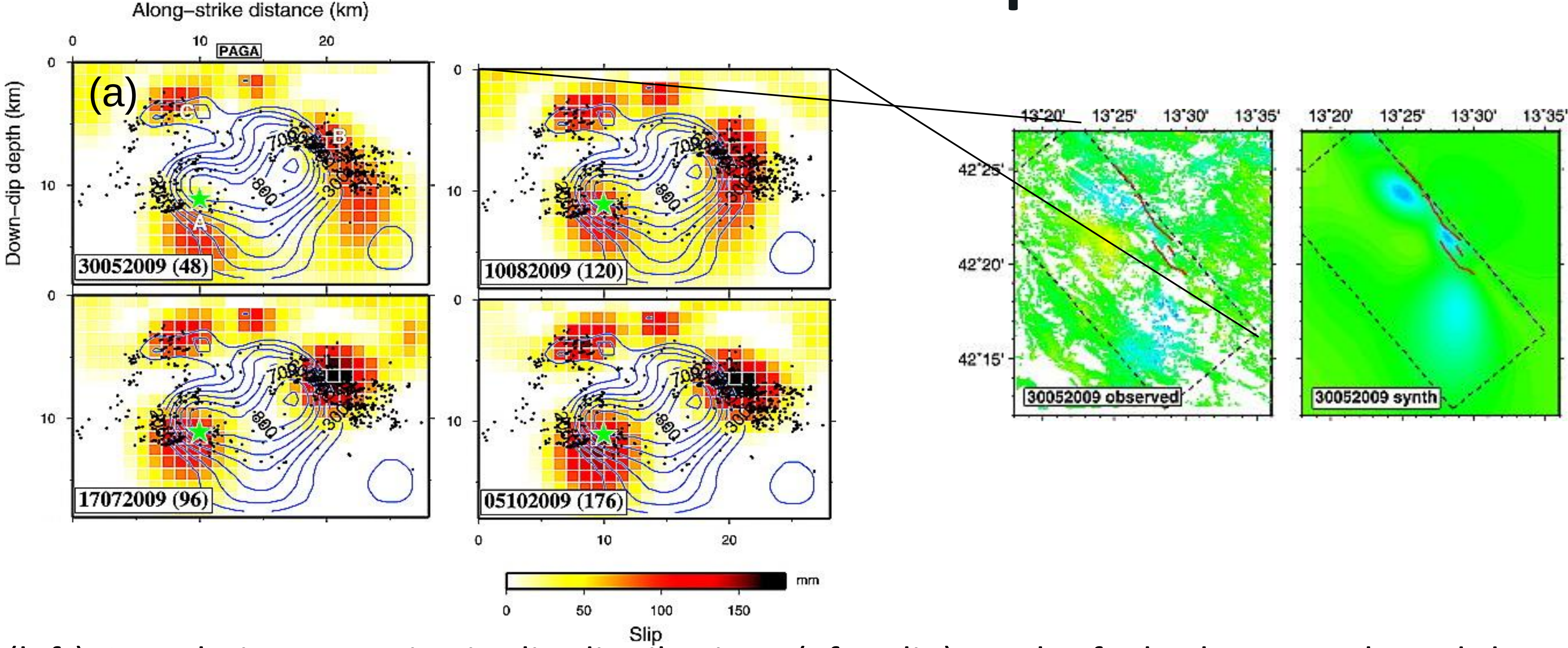

(left) Cumulative postseismic slip distributions (afterslip) on the fault plane at selected dates since 12 April 2009. The regions labeled with capital letters A, B and C are persistent features of the afterslip model derived from the inversion of postseismic observations. Coseismic slip is shown by blue contours for comparison. (right) An example of postseismic ground motion between 12 April and 30 May 2009 and a synthetic model calculated from the afterslip model in (a)

SAREDU Remote Sensing Education Initiative

D'Agostino et al., 2012

Viscoelastic relaxation

- **Process definition**
  - The postseismic deformation is caused by stress relaxation in the ductile lower crust and upper mantle (viscoelastic material) below the seismogenic upper crust

- **Deformation pattern**
  - Different deformation pattern than coseismic deformation

- **Time scale**
  - Several decades or longer

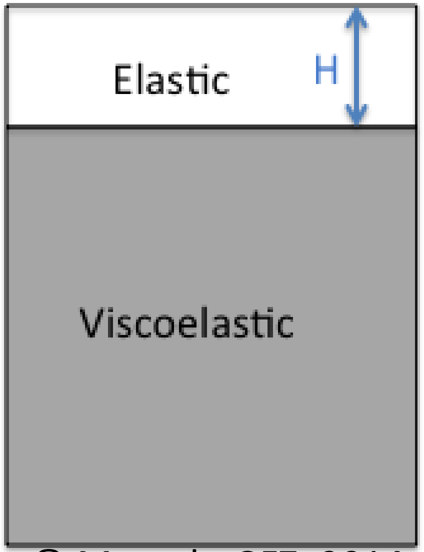

© Motagh, GFZ, 2014

SAREDU Remote Sensing Education Initiative

Viscoelastic Rheology

- **Burger body**

μ_m, μ_k : Hooke's law (elasticity)

η_m, η_k : Newtonian fluid (viscosity)

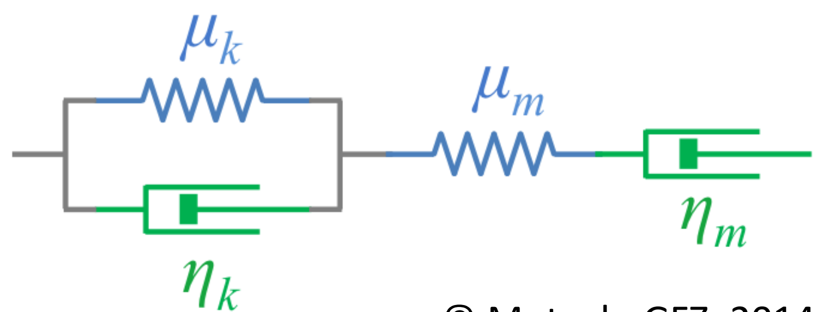

© Motagh, GFZ, 2014

- **Viscosity**
  - Fluid viscosity is a measure of its resistance to flow. For a linear rheology:

$$\eta = \frac{\sigma_s}{\dot{\gamma}_s}$$

σ_s : shear stress

$\dot{\gamma}_s$: shear strain rate

For mantle $\simeq 10^{20} - 10^{22}$ Pascal-second (Pa.s); for water $\simeq 10^{-3}$ Pa.s at T=20°C

For glacier ice $\simeq 10^{13}$ Pa.s

Ranalli (1995)

Viscoelastic Rheology

- Special cases of a Burger's body:
  - Maxwell

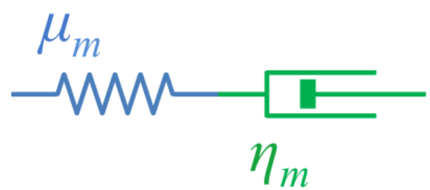

$$t_r = \frac{h_m}{m_m} : \text{relaxation time}$$

  - Kelvin

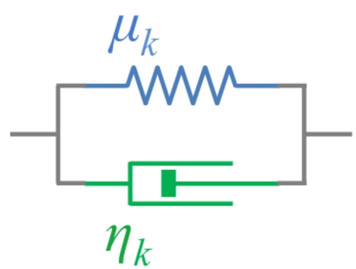

$$t_c = \frac{h_k}{m_k}$$

  - Standard linear solid

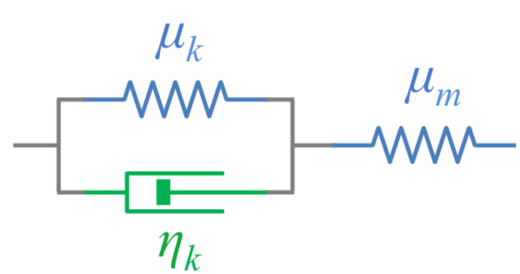

$$t_r = \frac{h_k}{m_k + m_m}$$

$$t_c = \frac{h_k}{m_k}$$

Tools

- **PSGRN/PSCMP**

  -FORTRAN code for calculating of co- and post-seismic deformation in multi-layered viscoelastic half-space based on the viscoelastic-gravitational dislocation theory (Wang et al. 2006)

  -The software can be downloaded

  ftp://ftp.gfz-potsdam.de/pub/home/turk/wang/psgrn+pscmp-2008a.zip

  Or email to wang_AT_gfz-potsdam.de

- **Visco1D**

  -A Program package to calculate quasi-static deformation on a layered spherical Earth

  -The software can be downloaded from

  https://earthquake.usgs.gov/research/software/#VISCO1D

Simulation using PSGRN/PSCMP

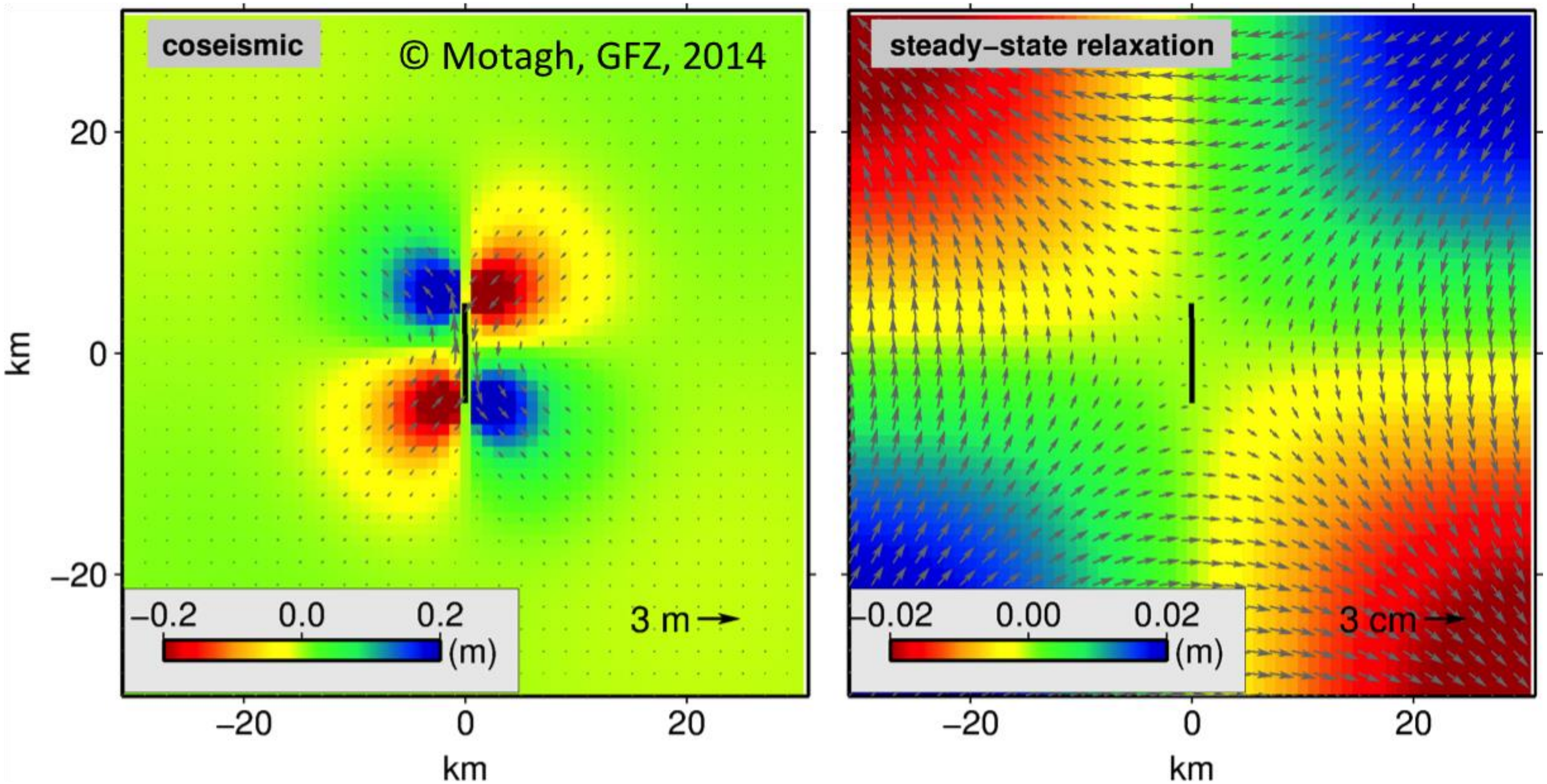

Coseismic and postseismic surface displacement due to stress perturbation of a vertical right-lateral strike-slip fault 10 km long, extending from the surface to a depth of 10 km and slips 5 m. The brittle-ductile transition occurs at a depth of 30 km with Maxwell viscosity of 10^{19} Pa.s. The color shows vertical deformation.

SAREDU Remote Sensing Education Initiative

Simulation: May 1960 (M_w=9.5) Valdivia, Chile, earthquake

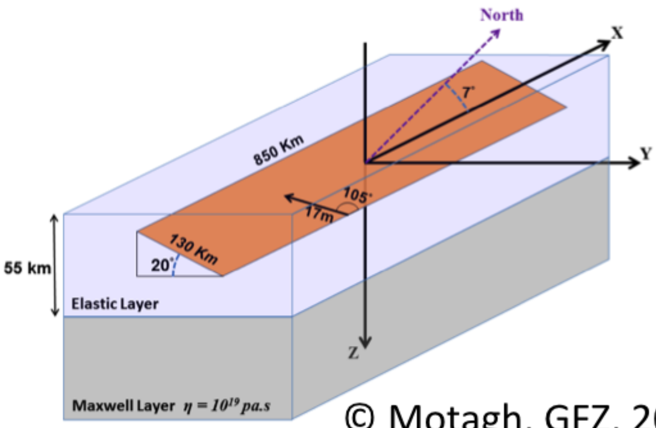

© Motagh, GFZ, 2014

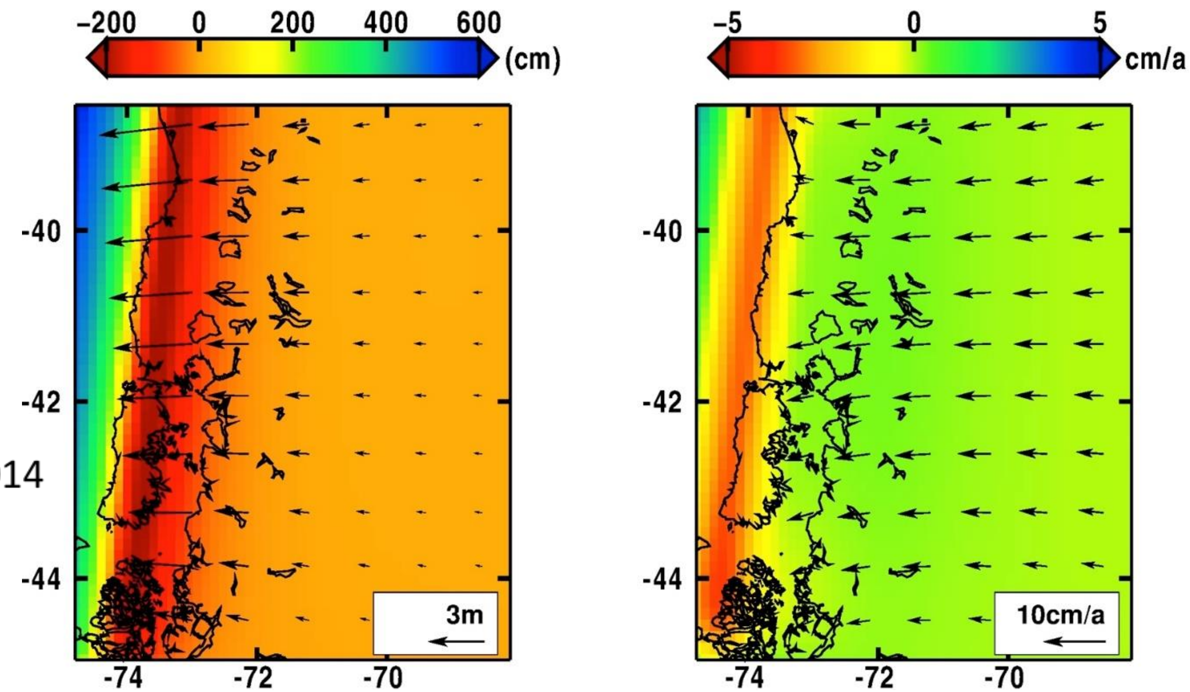

➘ Fault and rheology parameters used in the simulation (Wang et al. 2006)

(left) Coseismic displacement in a layered half-space earth model with 55 km elastic layer over a Maxwell viscoleastic half-space. The color shows vertical deformation. (right) Simulated postseismic deformation 50 years after the event.

SAREDU Remote Sensing Education Initiative

Viscoelastic relaxation after the 1999 Hector Mine earthquake

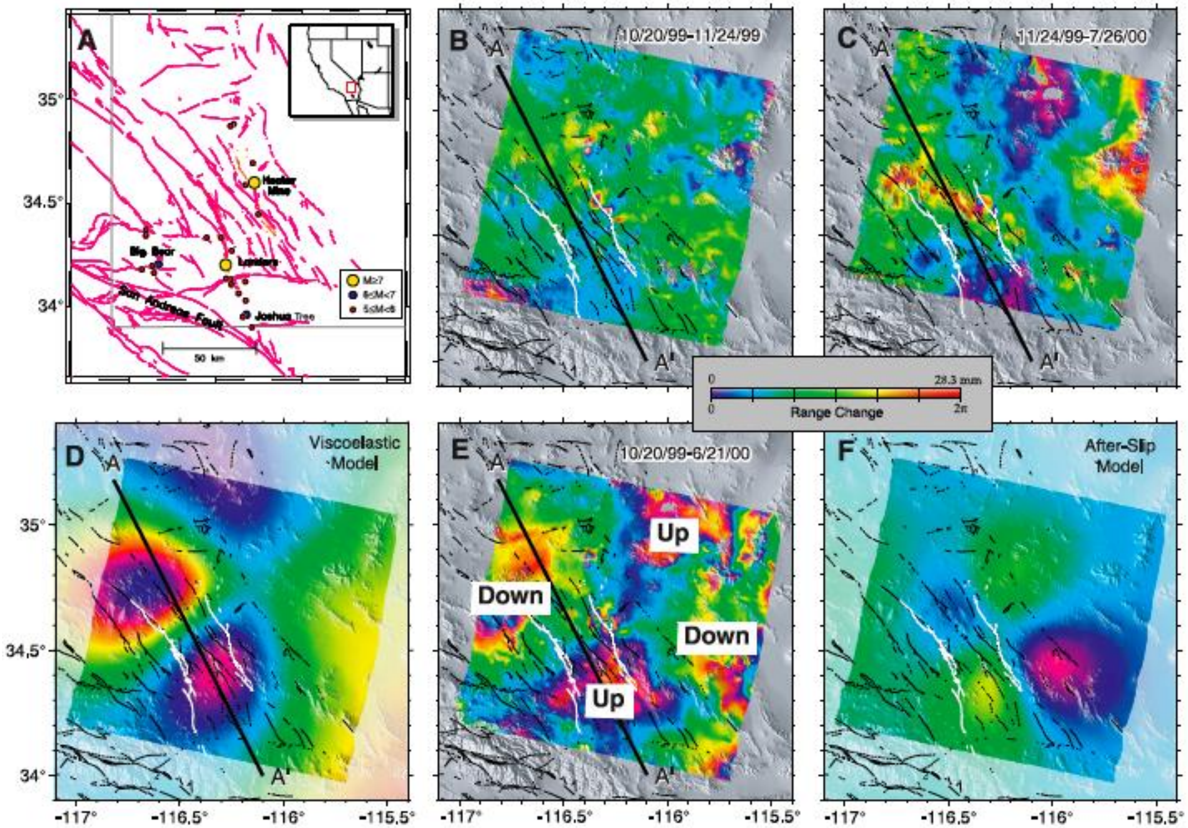

- Quadrant long-wavelength (> 30 km) LOS pattern, opposite to the sense of right-lateral coseismic fault slip, suggesting a deep transient source.
- Interpreted and modelled as the viscoelastic response of the upper mantle to the sudden stress changes caused by the earthquake

(A) Study area in the Mojave Desert, California. (B, C, E) Observed (wrapped) interferograms for various time periods after the Hector Mine earthquake. (D and F) are simulated interferograms from viscoelastic and afterslip models, respectively, for the time period 20.10.1999 to 21.06.2000.

Pollitz et al., 2001

Postseismic ground deformation after 2002, M 7.9, Denali Fault earthquake

Stacking

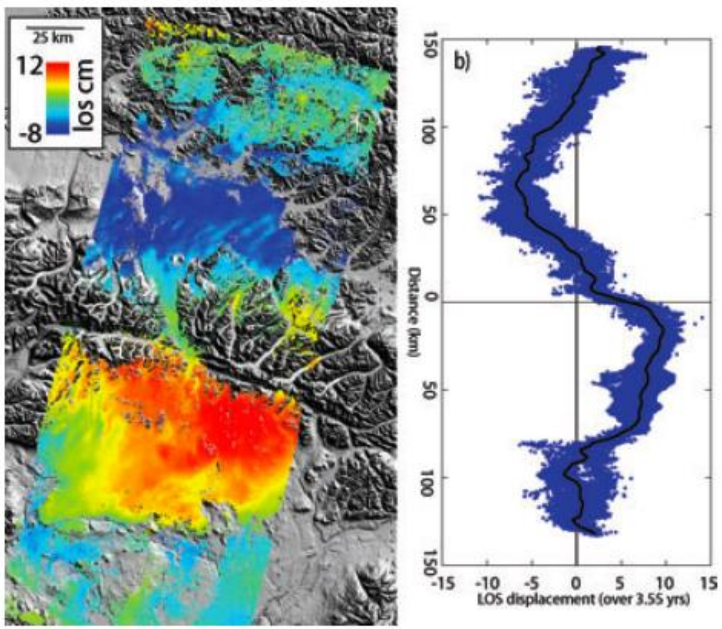

Stack of four interferograms from the time period summer 2003 – summer 2004. Total duration is 3.55 yr, giving a peak range change velocity of ~2–3 cm/yr in the satellite line-of-sight (b) Profile taken perpendicular to the fault. Peak displacement is located ~50–60 km from the fault in the north.

Time-series analysis

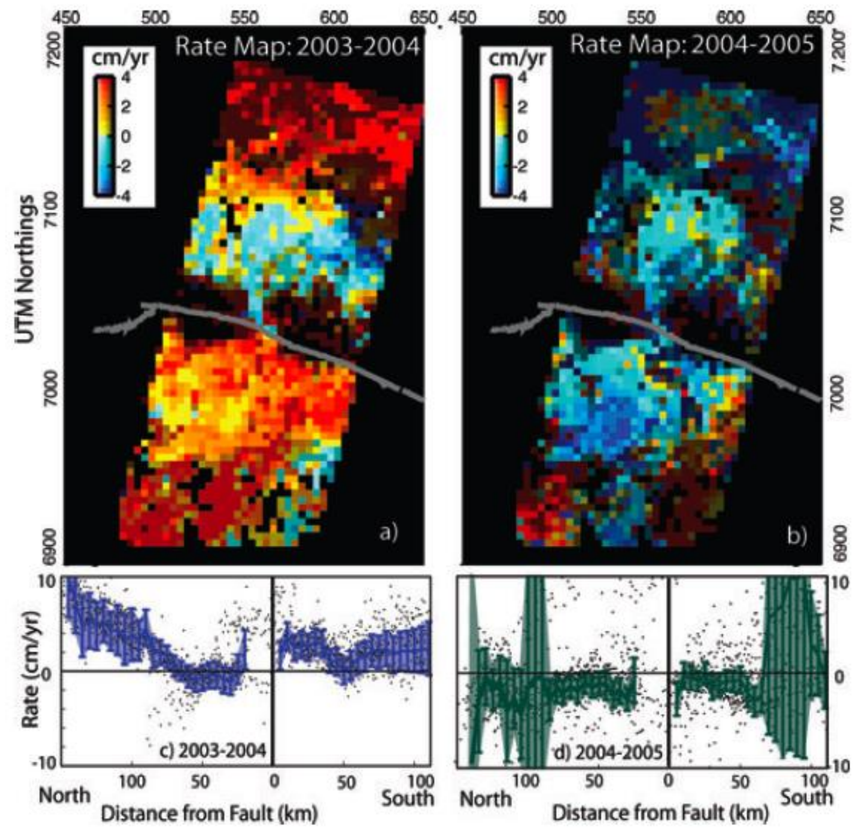

Rate maps for (a) 2003–2004 and (b) 2004–2005. Profiles through the postseismic rate maps for (c) 2003–2004 (d) 2004–2005.

Biggs et al., 2009

SAREDU Remote Sensing Education Initiative

Postseismic mechanism: 2002, M 7.9, Denali Fault earthquake

After-slip model

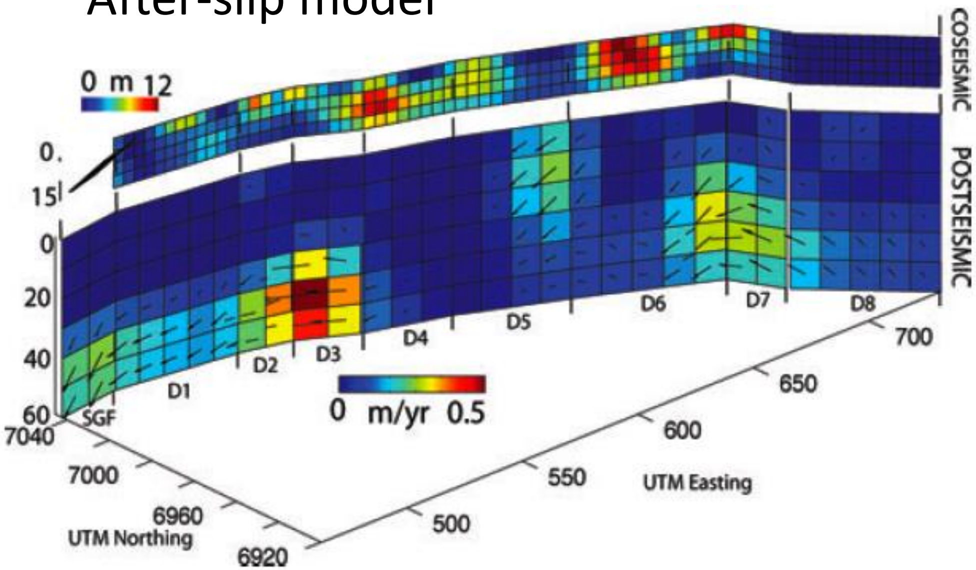

Combined afterslip_viscoelastic model

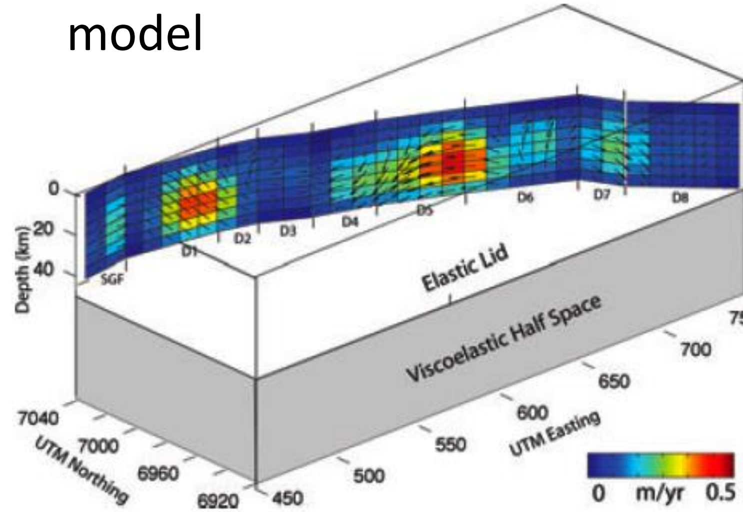

- Postseismic response to the coseismic stress occurred in the upper mantle (depths > 50 km)
- Both afterslip and Maxwell viscoelastic relaxation are able to explain InSAR observations

Biggs et al., 2009

Poroelastic deformation

- **Process definition:**
  - **Deformation due to pore pressure diffusion**
    - Coseismic dislocation in a poroelastic medium which is in the undrained condition (i.e. stationary fluid flow) causes pore fluid pressure changes in the upper crust
    - Fluid flow induced by excess pore-pressure gradient causes deformation, resulting in time-dependent postseismic deformation
    - As time passes fluid flow allows pore pressure gradients to vanish, and the volume of rock eventually reaches a drained condition
- **Deformation pattern**
  - Short wavelength as compared to the viscoelastic relaxation
- **Time-scale**
  - Months to years

Poroelastic deformation

- Governing equation in linear poroelasticity

$$(\lambda + 2\mu)\nabla(\nabla \cdot \mathrm{u}) - \mu\nabla \times (\nabla \times \mathrm{u}) - \alpha\nabla p = \nabla \cdot \Gamma$$

λ, μ: Lamé coefficients

Γ: stress tensor

u: displacement vector

p: excess pore pressure

α: dimensionless coefficient of effective stress, i.e. the change in pore pressure per unit change in bulk volume under drained conditions

Wang & Kümpel, 2003

SAREDU Remote Sensing Education Initiative

Poroelastic deformation

- The fully relaxed (time infinity after the earthquake) postseismic poroelastic response can be approximated by subtracting coseismic deformation using undrained moduli from the coseismic deformation using drained moduli

$$\nu = \frac{3K - 2\mu}{6K + 2\mu}$$

$$\frac{\partial \nu}{\partial K} = \frac{18\mu}{(6K + 2\mu)^2}$$

$$K_u > K_d \Rightarrow \nu_u > \nu_d$$

Undrained (coseismic)

Drained (postseismic)

- Some typical values $\nu_u = 0.3 \quad \nu_d = 0.27$

Rice & Cleary, 1976

Simulation: strike-slip fault

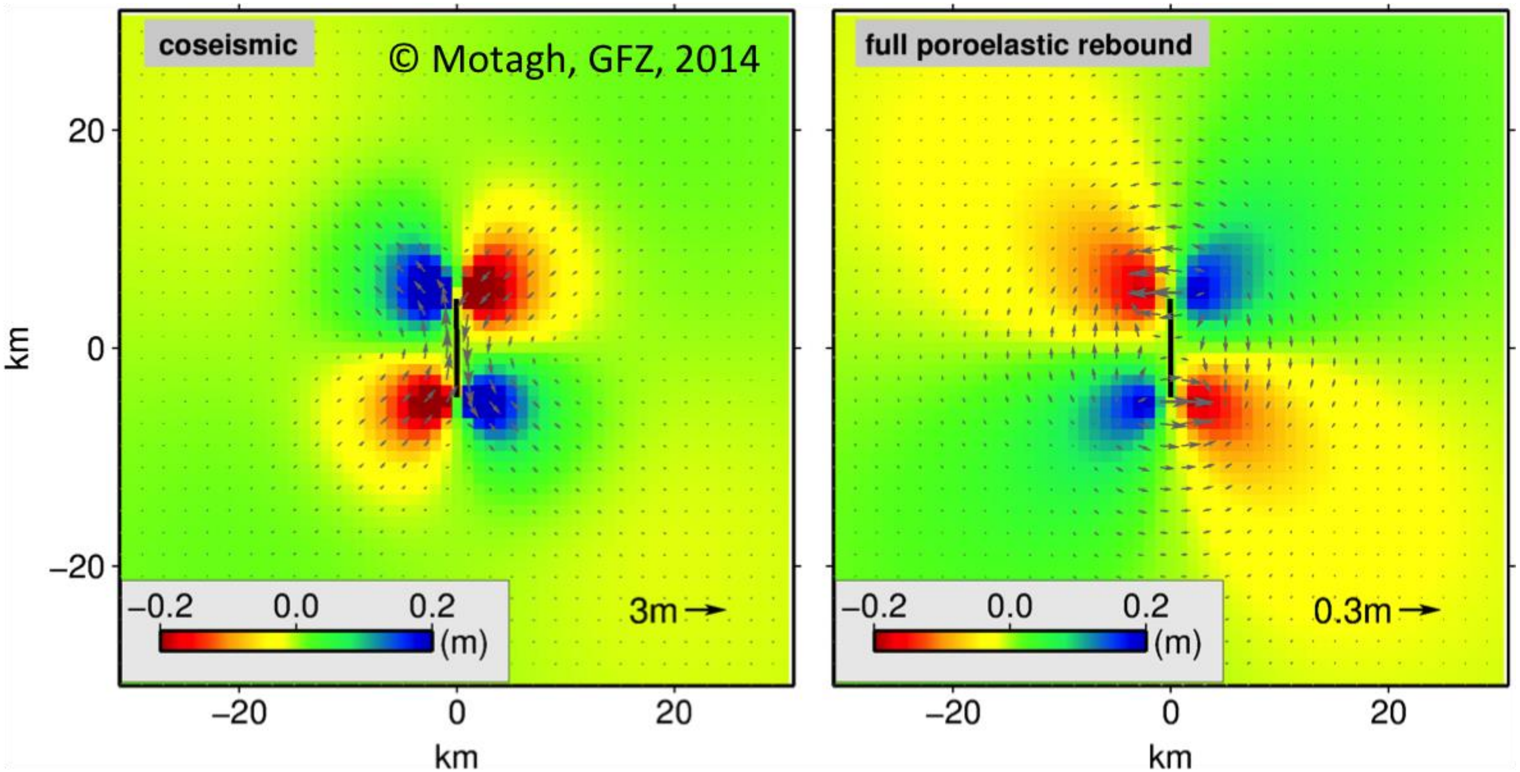

Coseismic (undrained conditions, i.e. no fluid flow) and full poroelastic rebound due to a vertical right-lateral strike-slip fault 10 km long, extending from the surface to a depth of 10 km and slips 5 m. The color shows vertical deformation. Zones of coseismic uplift turn into subsidence in the postseismic period and vice versa.

Simulation: Strike-slip faults with step-over

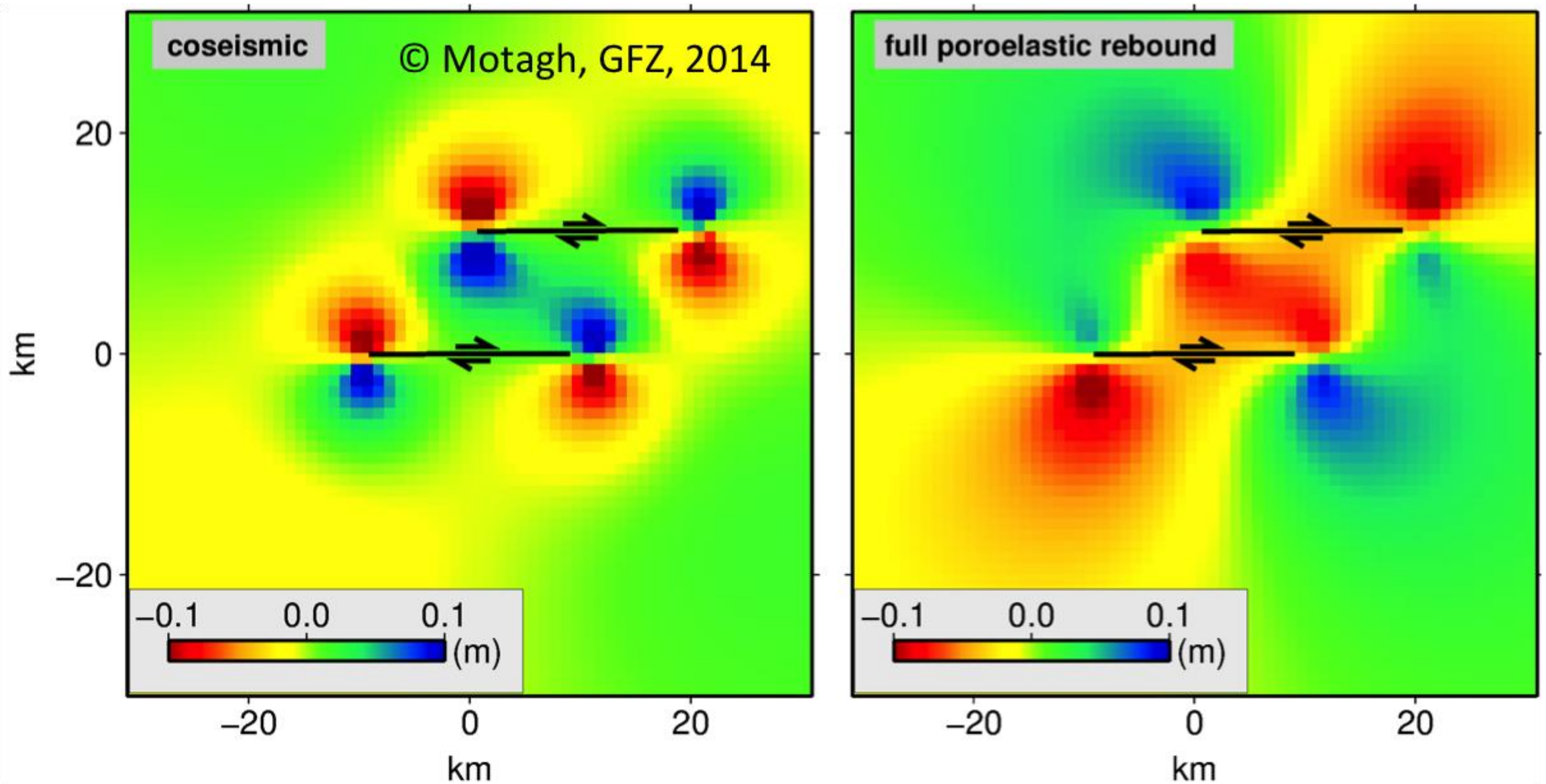

Coseismic and full poroelastic rebound due to two vertical right-lateral strike-slip faults with step-over (left-step). The faults are 20 km long, extending from the surface to a depth of 10 km and slip 2 m. The coseismic uplift at the fault step-over turns into subsidence during postseismic deformation period. The color shows vertical deformation.

Poro-elastic deformation after 17 June 2000 earthquake in South Iceland

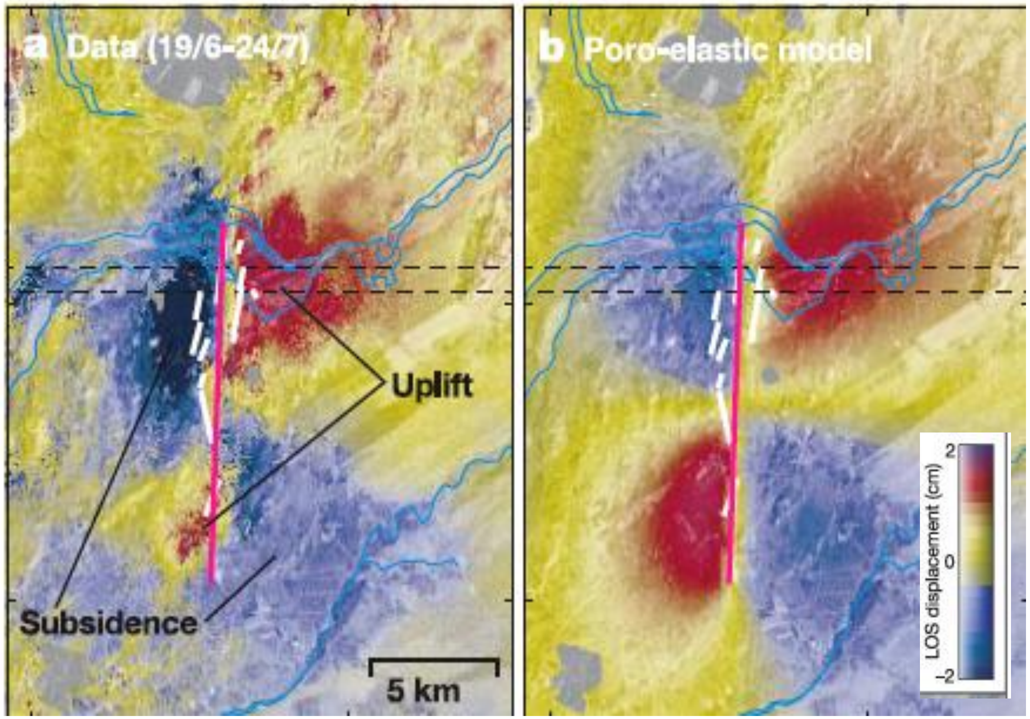

(a) Postseismic deformation (unwrapped) map after 17 June 2000 earthquake in South Iceland, spanning 19 June to 24 July 2000. (b) Synthetic map using a poro-elastic model. Purple line is the model fault trace of 17 June earthquake.

- LOS uplift in the quadrants of coseismic extension and LOS subsidence in quadrants of coseismic compression (opposite to the sense of right-lateral coseismic fault slip)
- Explained by poro-elastic rebound in the first 1-2 months after the earthquake

Jónsson et al., 2003

Postseismic rebound along the 28 June, 1992 Landers earthquake

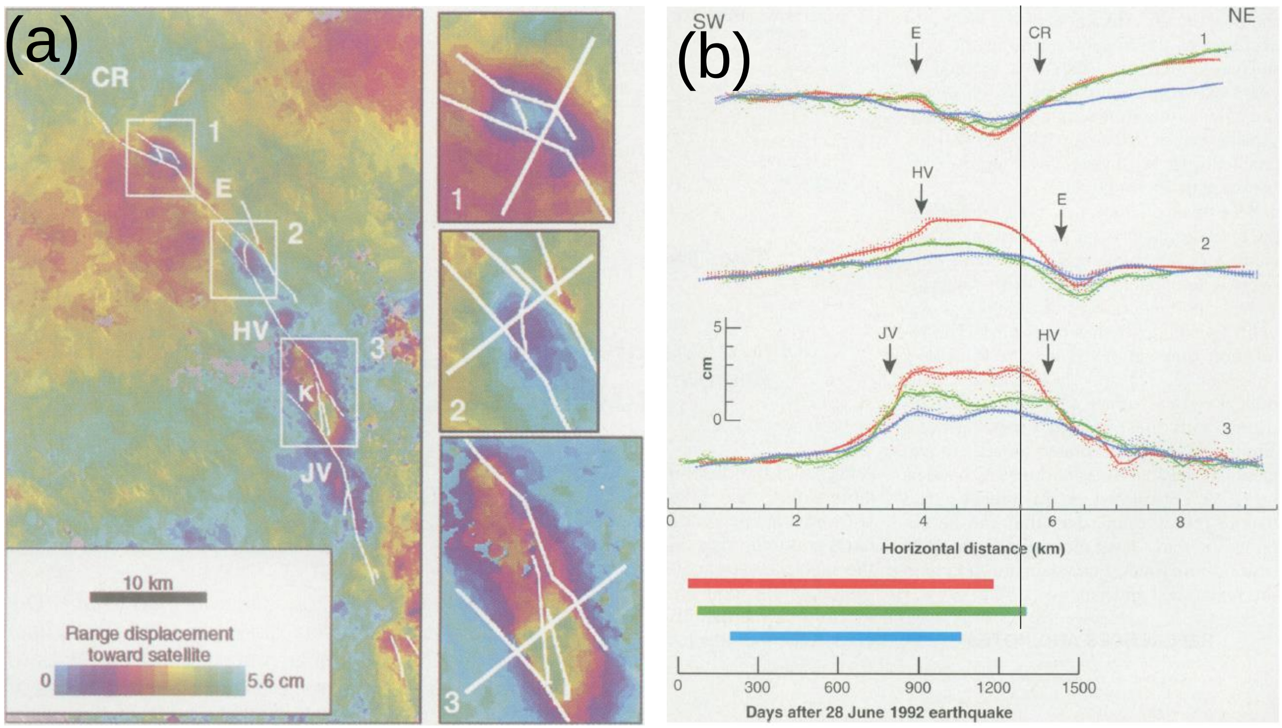

- Local strains in the fault step-overs: uplift in the pull-apart structures and subsidence in a compressive jog along the 1992 Landers earthquake

- Explained by poro-elastic rebound due to pore fluid pressure gradients in the shallow crust

(a) Postseismic deformation map covering 41 days after the 1992 Landers earthquake starting on 7 August 1992. (b) Line-of-Sight (LOS) displacement along profiles 1,2, and 3 in the left figure.

Peltzer et al., 1996

SAREDU Remote Sensing Education Initiative

Structure

- Introduction to Plate Tectonics
- InSAR and earthquakes
- InSAR and postseismic deformation
- InSAR and interseismic deformation
- InSAR and volcano deformation
- InSAR and landslides
- InSAR and anthropogenic deformation

  [see also Module 3101: Anthroposphere – SAR Interferometry]

InSAR and interseismic deformation

- **Goal**
  - To quantify strain accumulation and amount of interseismic loading on locked segments of active faults for a better understanding of earthquake cycle and assessing seismic hazards
- **Data requirement and methodology**
  - Data: SAR images in single polarization
  - Techniques: Stacking or advanced time-series methods to improve signal to noise ratio in measuring large-scale deformation
- **Main analytical models**
  - Screw dislocation embedded in a homogenous elastic half-space
  - Viscoelastic relaxation

InSAR and interseismic deformation

- **Advantages**
  - Under favorable interferometry conditions, high spatial resolution and temporal sampling of InSAR observations allow for quantifying variation and distribution of strain rate along active faults at an unprecedented level of detail
- **Error sources**
  - Atmospheric noise and orbital error limit the capability of InSAR observations to study large-wavelength tectonic signal caused by interseismic strain
- **Outlook for future satellites**
  - Regular data acquisition by future SAR missions (e.g. Sentinel) allows for a more accurate estimation of long-wavelength interseismic deformation around active faults

SAREDU Remote Sensing Education Initiative

Sketch of some interseismic models

Screw-dislocation for a very long vertical strike-slip fault

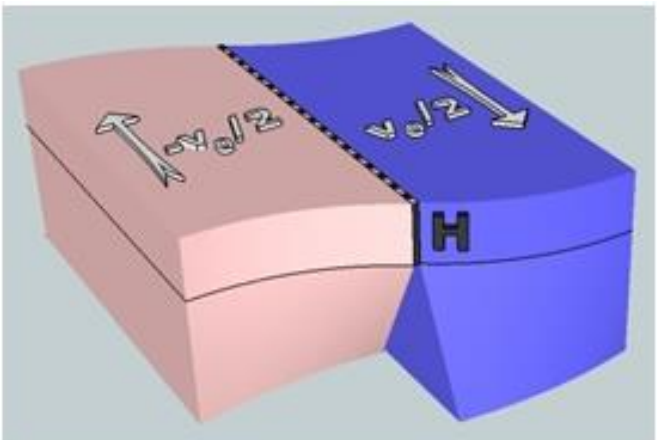

Parameters:

H= Locking depth

V_0=Slip rate

Viscoelastic model for a very long vertical strike-slip fault

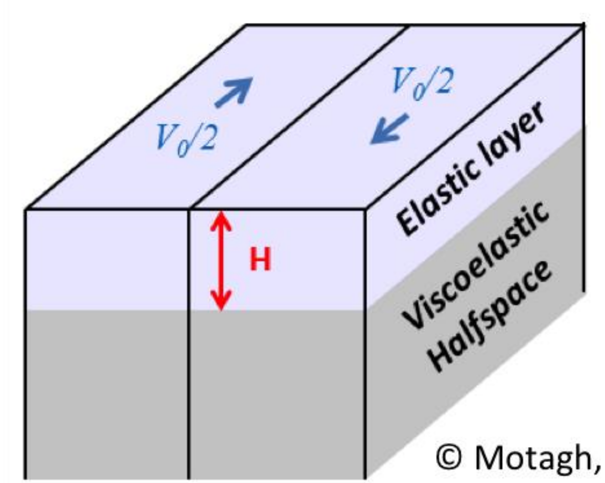

© Motagh, GFZ, 2014

Parameters:

H=Elastic thickness or Locking depth

T= Earthquake period

$t_R = 2\eta/\mu$; t_R Relaxation time,

η: Viscosity, μ: Shear modulus

V_0 : Far field velocity

Segall, 2002

SAREDU Remote Sensing Education Initiative

Screw-dislocation for a very long vertical strike-slip fault

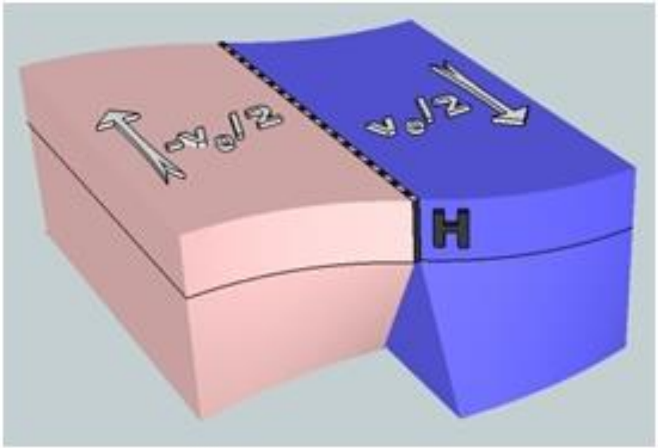

Parameters:
H= Locking depth
V_0=Slip rate

- The assumed earth model consists of a elastic half-space rheology
- No slip takes place on the upper portion of the fault (H) between earthquakes, but the lower part creeps continuously at a constant rate V0
- The fault-parallel velocity is given by:

$$v(x) = (v_0/p)\tan^{-1}(x/H)$$

v : fault parallel velocity

x : distance normal to the fault

v_0 : fault slip rate

Segall, 2002

- Interseismic velocity plot using screw-dislocation model for a very long vertical strike-slip fault with a fixed locking depth

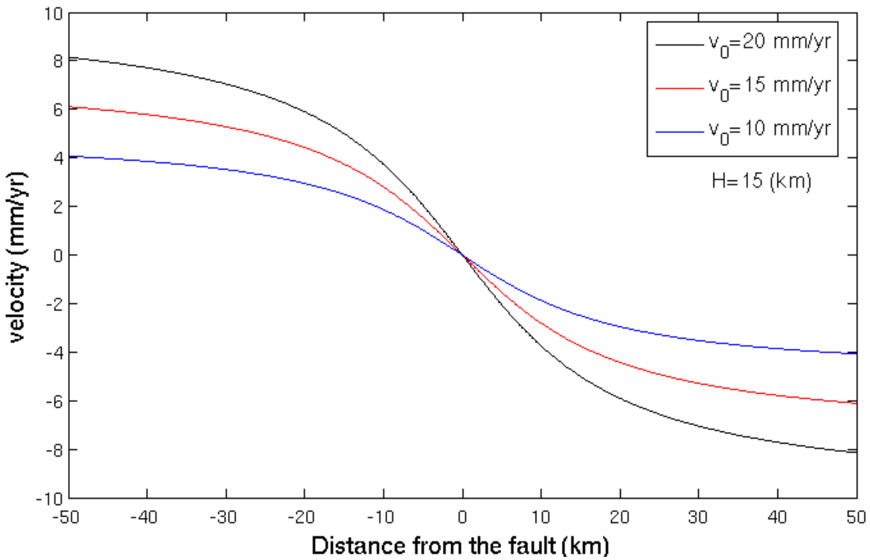

- Interseismic velocity plot using screw-dislocation model for a very long vertical strike-slip fault with a fixed slip rate

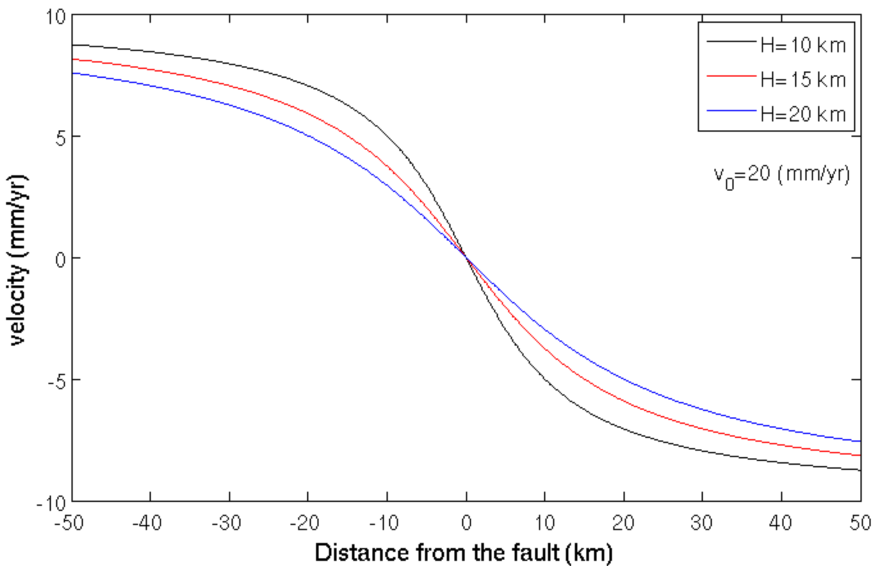

SAREDU Remote Sensing Education Initiative

Viscoelastic model for a very long strike-slip fault

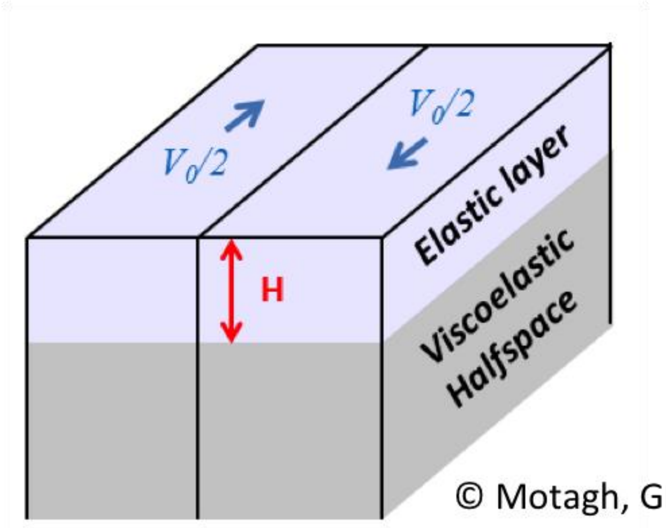

- The assumed earth model consists of an elastic layer (lithosphere/schizosphere) of thickness H, overlying a Maxwell viscoelastic half-space (asthenosphere/plastosphere).
- Each coseismic slip event in the lithosphere causes instantaneous stress changes in the underlying half-space which will then relax over time via viscoelastic flow at depth.
- The interseismic fault-parallel velocity as a function of distance across strike, x, is given by:

$$v(x,t) = (v_0/\pi) \sum_{n=1}^{\infty} \phi(t/\tau_R, T/\tau_R) F_n(x,H)$$

Where: $$\phi(t/\tau_R, T/\tau_R) = \frac{T}{\tau_R} \frac{e^{-t/\tau_R}}{(n-1)!} \sum_{k=0}^{\infty} e^{-kT/\tau_R} \left(\frac{t+kT}{\tau_R}\right)^{n-1}$$

$$F_n(x,H) = \tan^{-1}\left[\frac{2xH}{x^2 + (2nH)^2 - H^2}\right]$$

Segall, 2002

Parameters:

H=Elastic thickness or Locking depth

T= Earthquake period

$t_R = 2h/m$; t_R relaxation time,

h: viscosity, m: shear modulus

V_0 : Far field velocity

SAREDU Remote Sensing Education Initiative

- Interseismic velocity distribution for a very long strike-slip fault using visco-elastic model for $T/\tau_R=1$ (A) and $T/\tau_R=5$ (B)

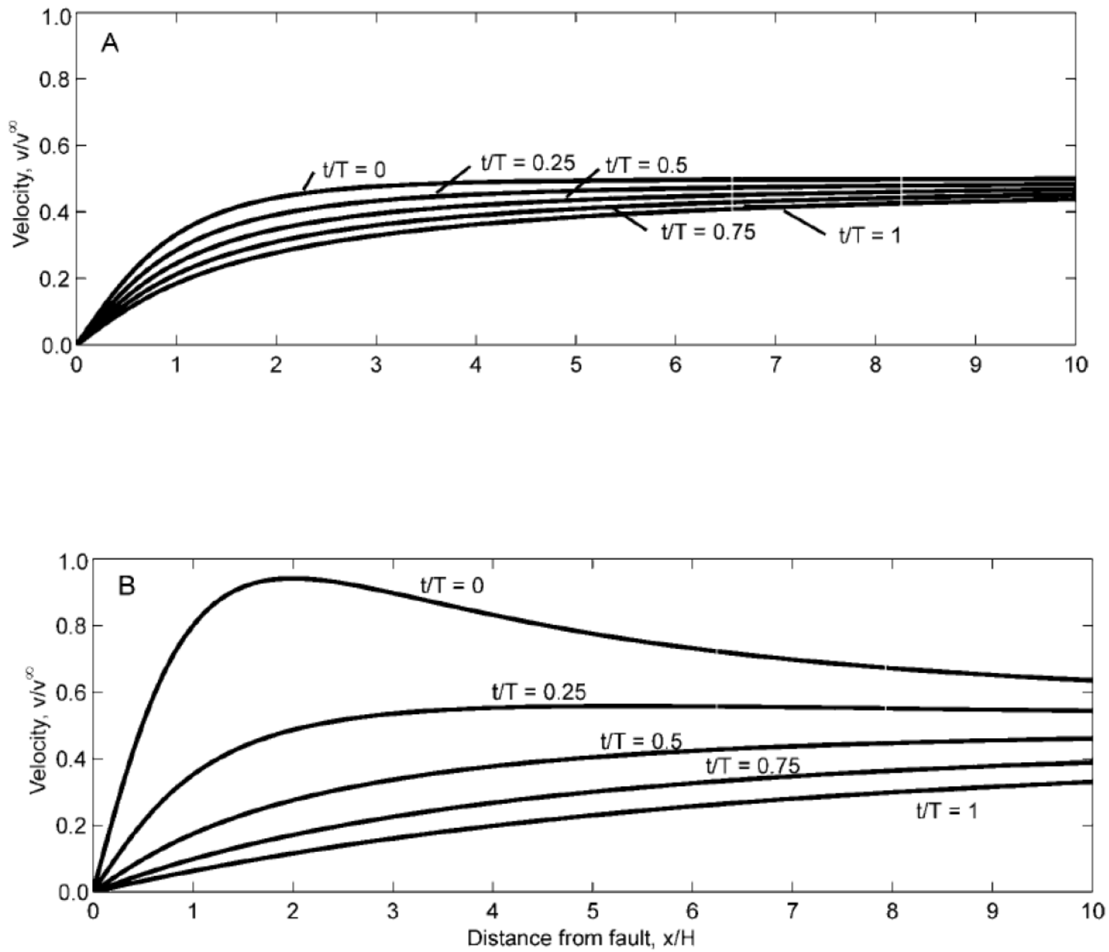

Segall, 2002

SAREDU Remote Sensing Education Initiative

Example: North Anatolian Fault, Turkey

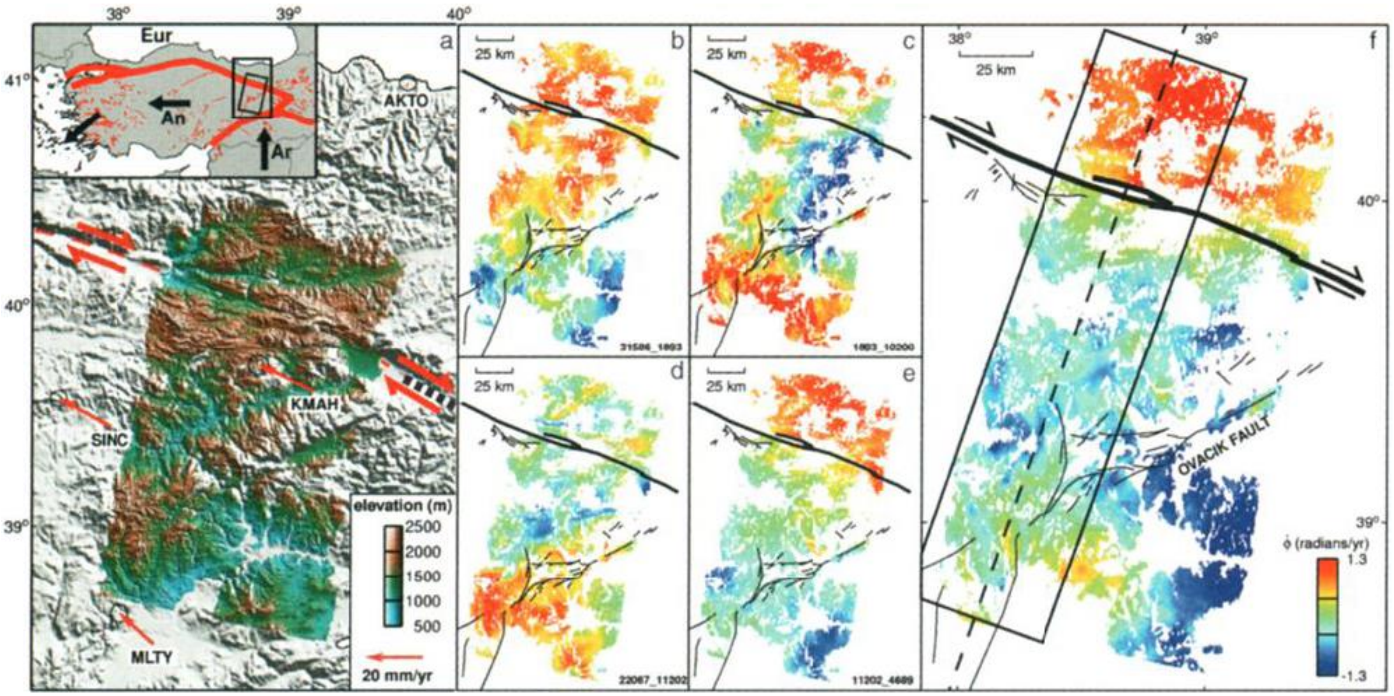

Strong phase gradient on the surface trace of the NAF, distributed over ~ 70 km, obtained by the stacking technique using ERS1/2 data

(a) Map of eastern end of the North Anatolian Fault. (b-e) Four inter-seismic unwrapped interferograms constructed using repeat-pass interferometry. The interferograms are scaled by the time interval so that each is an estimate of yearly phase change. (f) The stacked interferogram calculated by summing the individual unwrapped interferograms and dividing by the total time of 7.4 years.

Wright et al., 2001

SAREDU Remote Sensing Education Initiative

Example: North Anatolian Fault, Turkey

Stacked interferogram

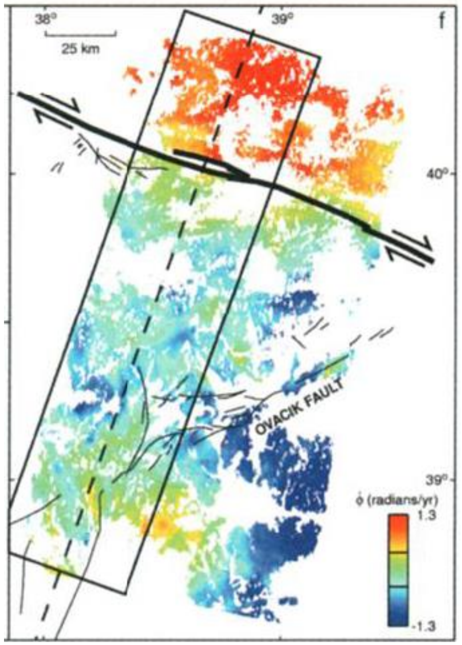

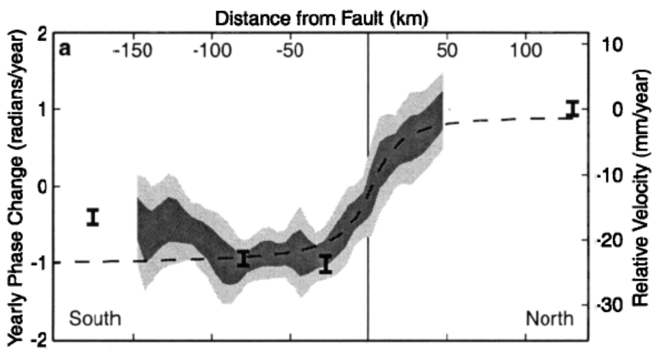

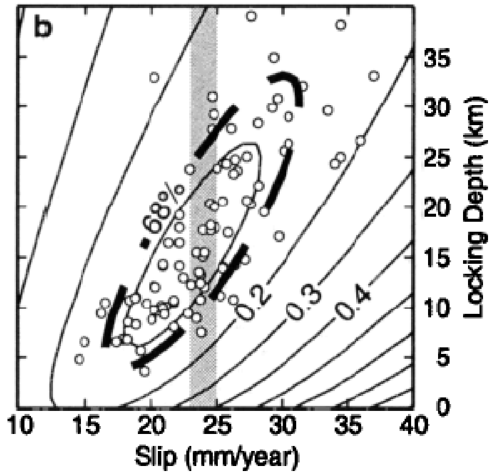

Wright et al., 2001

(a) Phase profile perpendicular to the North Anatolian Fault. The thick grey bands are 1- and 2-σ error bounds on the phase, measured in the box shown on the left. Black bars indicate GPS velocities and error bounds. The dashed line indicates velocities predicted by the best-fitting screw-dislocation model (slip rate of 22 mm/yr under a 14 km elastic lid). (b) A-posteriori errors on the slip ate and locking depth derived using a Monte-Carlo simulation technique. The dashed ellipse illustrates 68% confidence region. Contours correspond to rms misfit.

SAREDU Remote Sensing Education Initiative

NAF Interseismic from Envisat

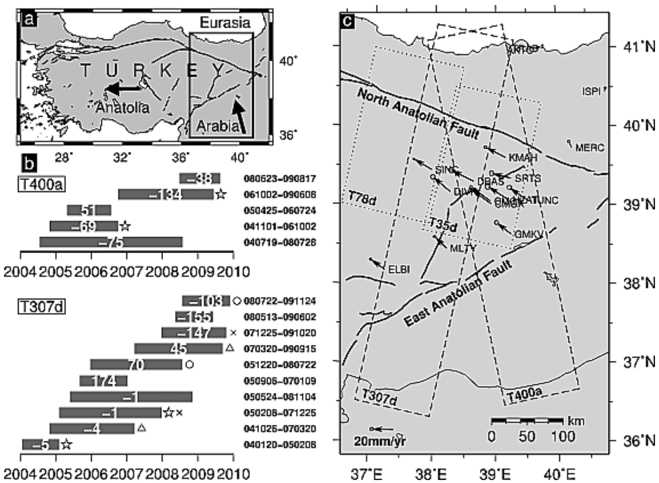

- (a, c): Study area on the North Anatolian Fault. Black box in (a) is the location of (c)
- (b): Ascending (T400a) and descending (T307d) ASAR images from Envisat

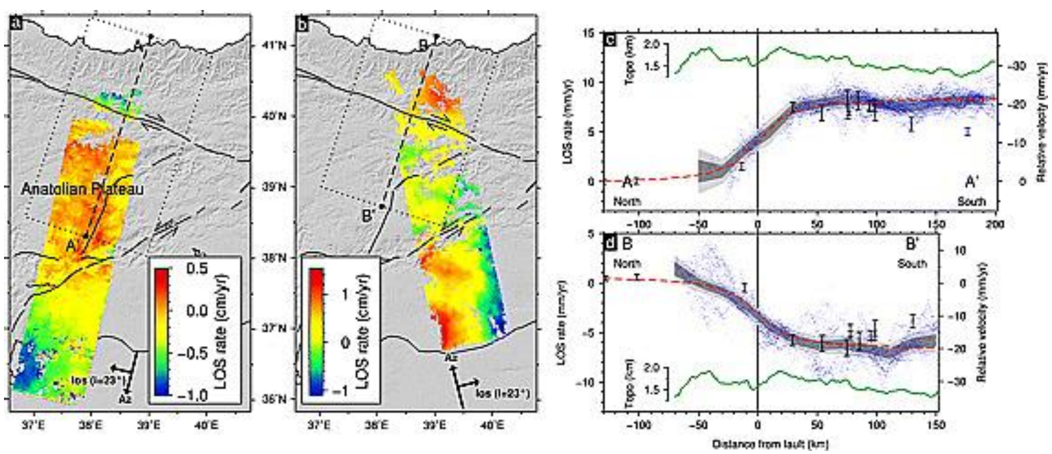

- (a, b): Interseismic LOS velocity map from descending (a) and ascending (b) Envisat data
- (c, d): LOS profile for descending (T307d) and ascending (T400a) with 1- and 2σ error bounds as grey bands. Red dashed line is the best fit slip model (slip rate: 20-26 mm/yr below a locking depth of 13.5-25 km).

SAREDU Remote Sensing Education Initiative

Walters et al., 2011

San Andreas Fault, California

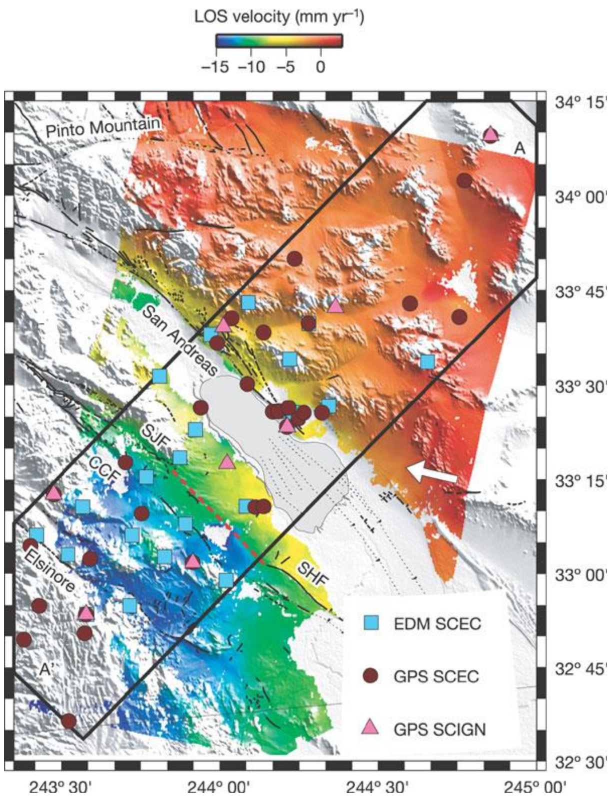

- Asymmetric pattern of interseismic velocity with respect to fault traces
- Possibly caused by rigidity contrasts across the fault

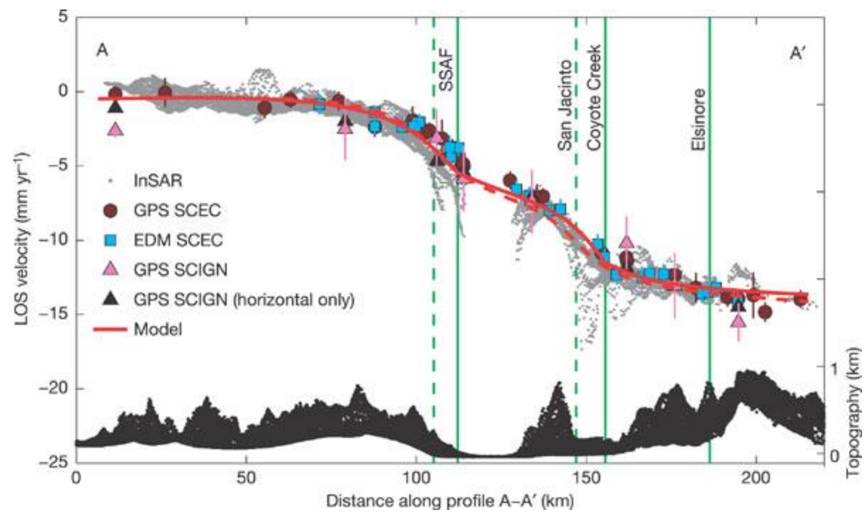

(left) Line of sight (LOS) interseismic velocity across the southern San Andreas fault system from a stack of ERS interferograms spanning a time interval between 1992 and 2000. (right) Average LOS velocities (grey dots) along the profile A-A' shown on the left. Solid and dashed red lines are theoretical interseismic models with and without lateral variations in the rock rigidity across the fault, respectively.

Fialko, 2006

SAREDU Remote Sensing Education Initiative

Interseismic deformation inferred from Persistent Scatterer analysis: Ganos Fault, Turkey

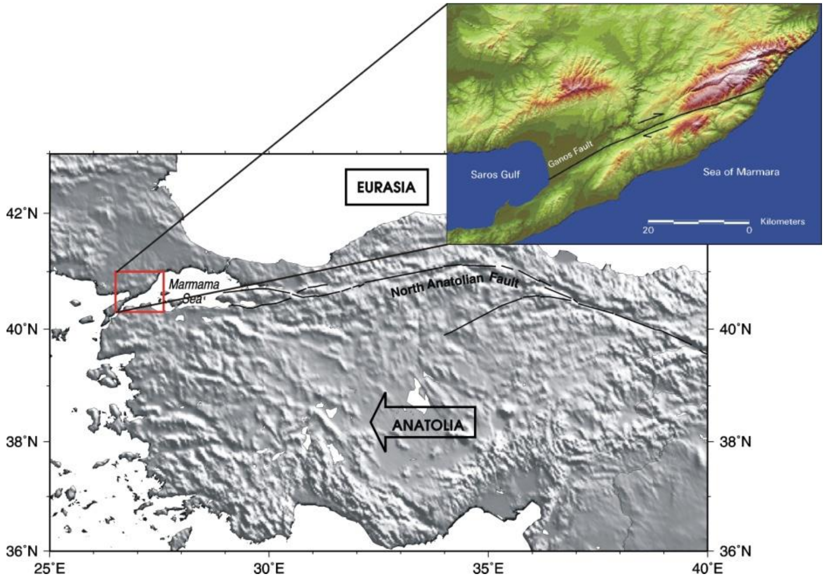

- Data: 44 ERS1/2 SAR image in descending orbit
- Methodology: PSI-GENESIS software developed at DLR (German Aerospace Agency)

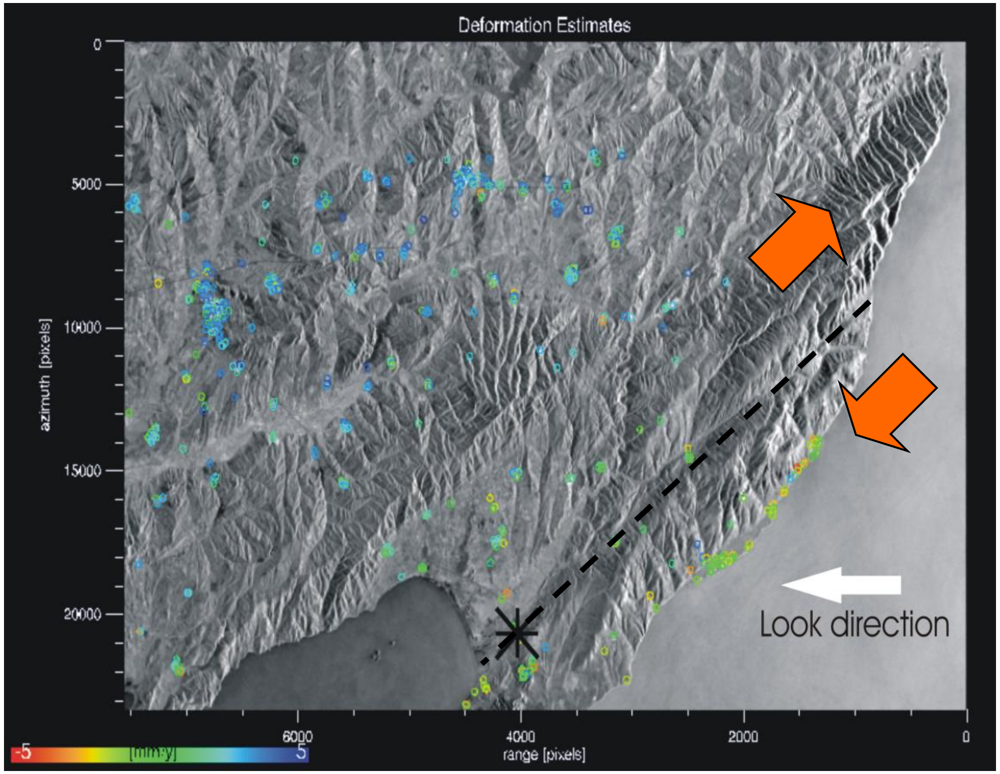

Motagh et al., 2007

Interseismic model inferred from inversion of deformation data

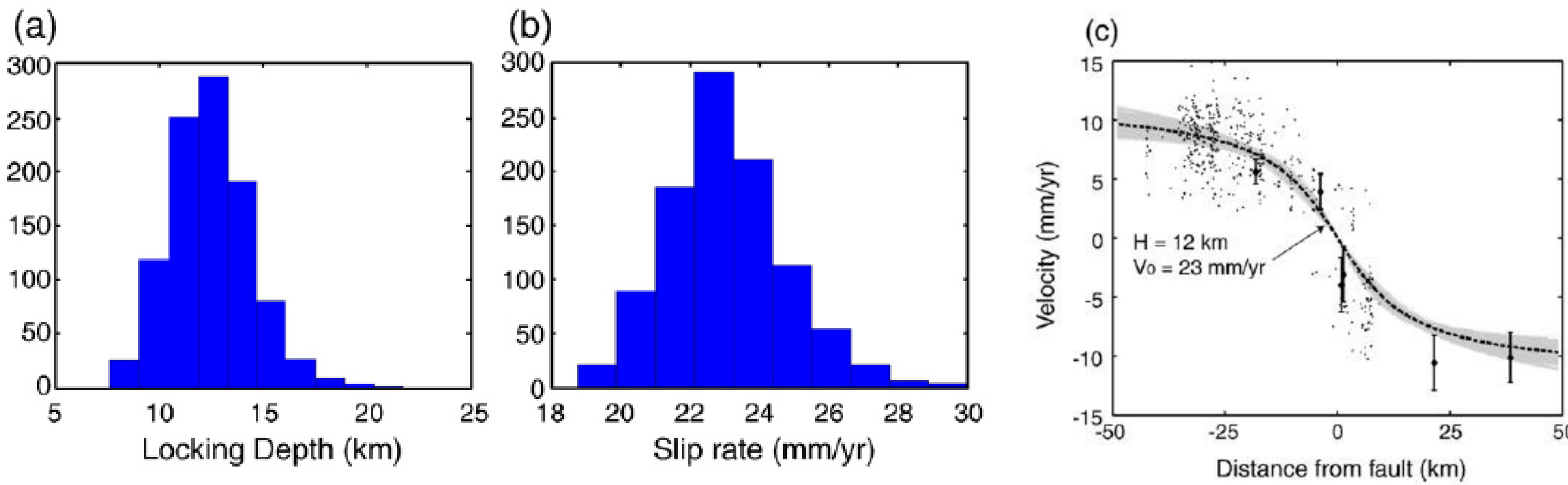

(a,b) Probability distribution for the locking depth and slip rate from bootstrap results using PS and GPS data. (c) Fit to PS and GPS (points with error bars) data using elastic half-space model for the range of parameters determined from the bootstrap method. The best fit model is represented by a dashed line.

The profile shows fault-parallel velocity of deformation data in a transect perpendicular to the strike of the Ganos fault.

Motagh et al., 2007

Longitudinal Valley, eastern Taiwan: PS-InSAR analysis

North LV

Center LV

South LV

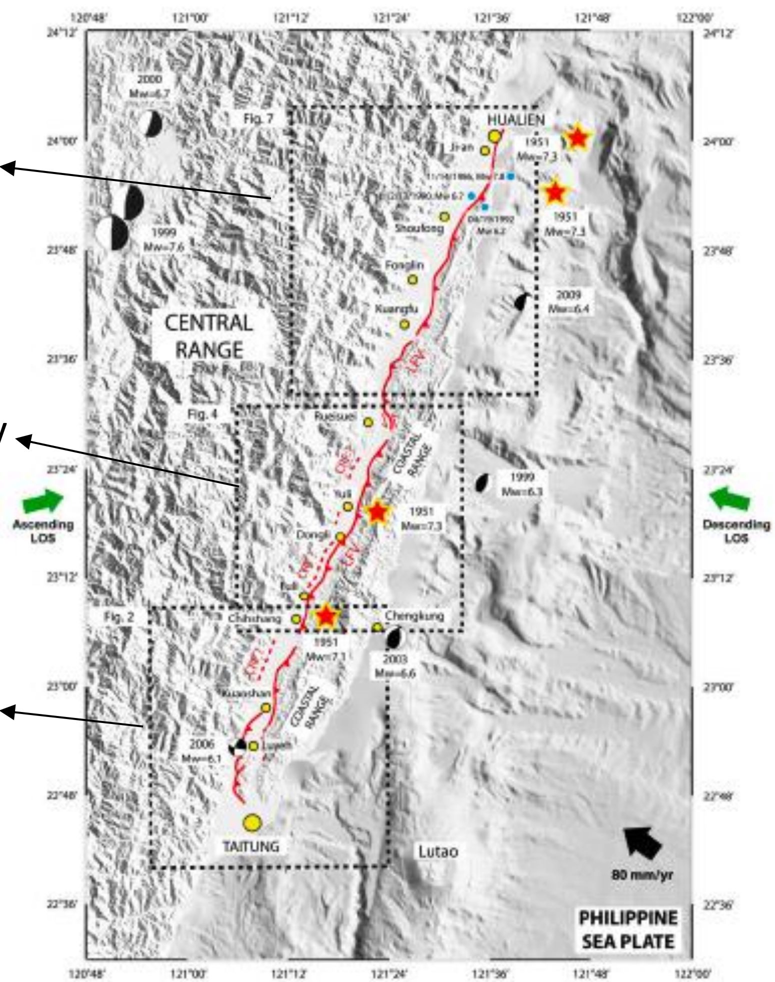

- Seismotectonic map of the Longitudinal Valley (LV) and Coastal Range (CR). Red lines are fault traces. Blue circles stand for earthquakes with magnitude higher than 6 between 1973 and 1993
- Data: ERS1/2 during 1993-1999 in both ascending and descending orbits
- Methodology: PS-InSAR

Peyret et al., 2011

South Longitudinal Valley

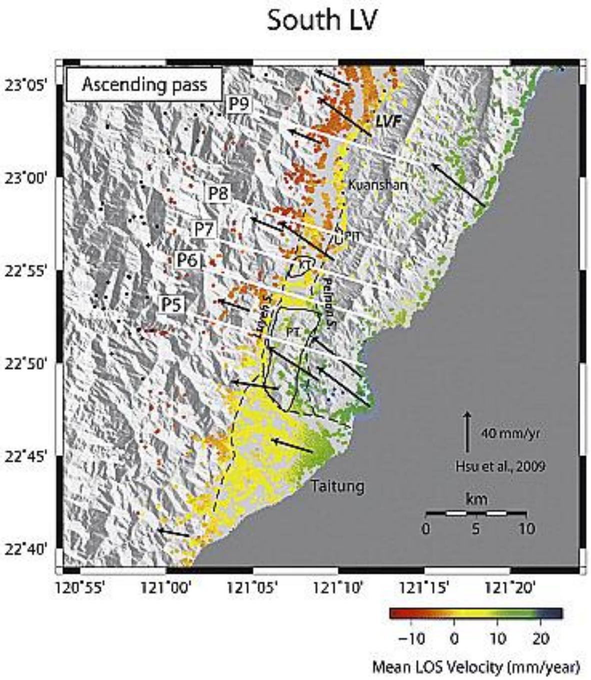

PS mean velocity map in the ascending (left) and descending (right) in South LV between Taitung plain and Kuanshan. Black dotted lines show the location of significant gradient changes in the PS velocity map. White lines show the location of the profiles presented in the right panel. Black vectors are GPS velocities.

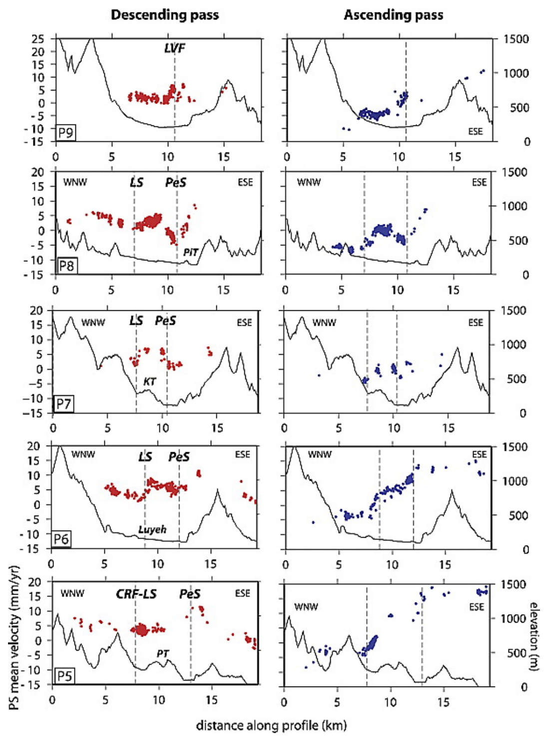

Some profiles of mean velocity in South LV, superimposed on the topographic profile. Black dotted lines correspond to the location of the faults as estimated from PS velocity map.

Peyret et al., 2011

SAREDU Remote Sensing Education Initiative

Center Longitudinal Valley

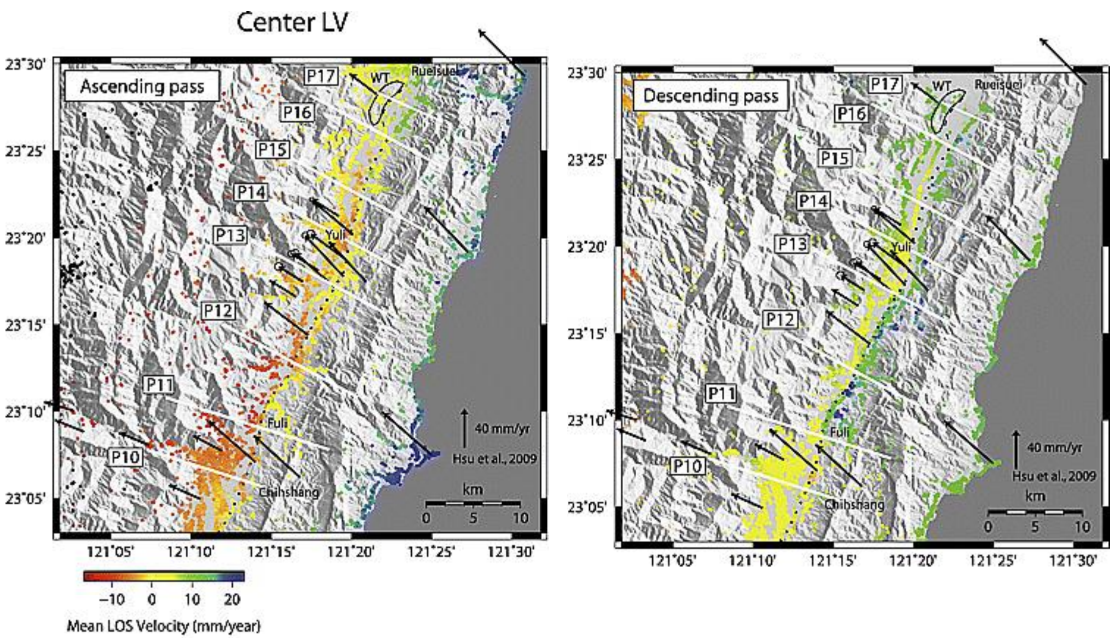

PS mean velocity map in the ascending (left) and descending (right) in Center LV between Chihshang and Rueisuei. Black dotted lines show the location of significant gradient changes in the PS velocity map. White lines show the location of the profiles presented in the right panel.

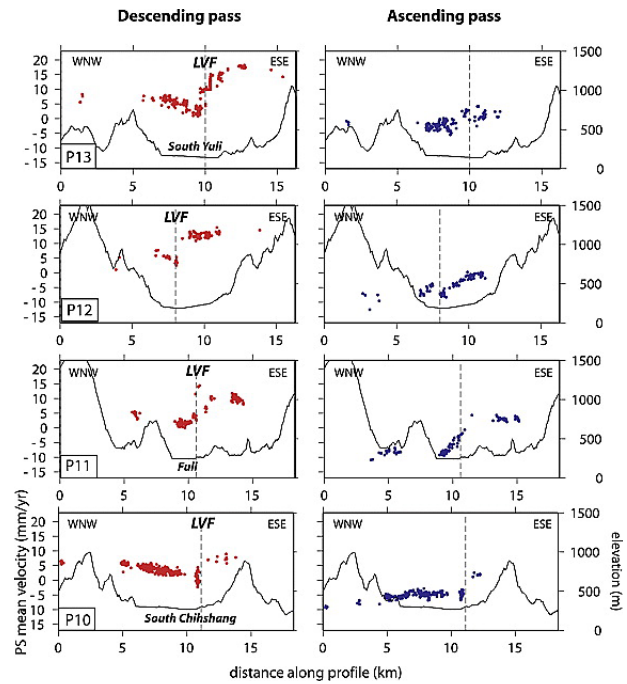

Some profiles of PS mean velocities in Center LV, superimposed on the topographic profile. Black dotted lines correspond to the location of the fault as estimated from PS velocity map.

Peyret et al., 2011

North Longitudinal Valley

North LV

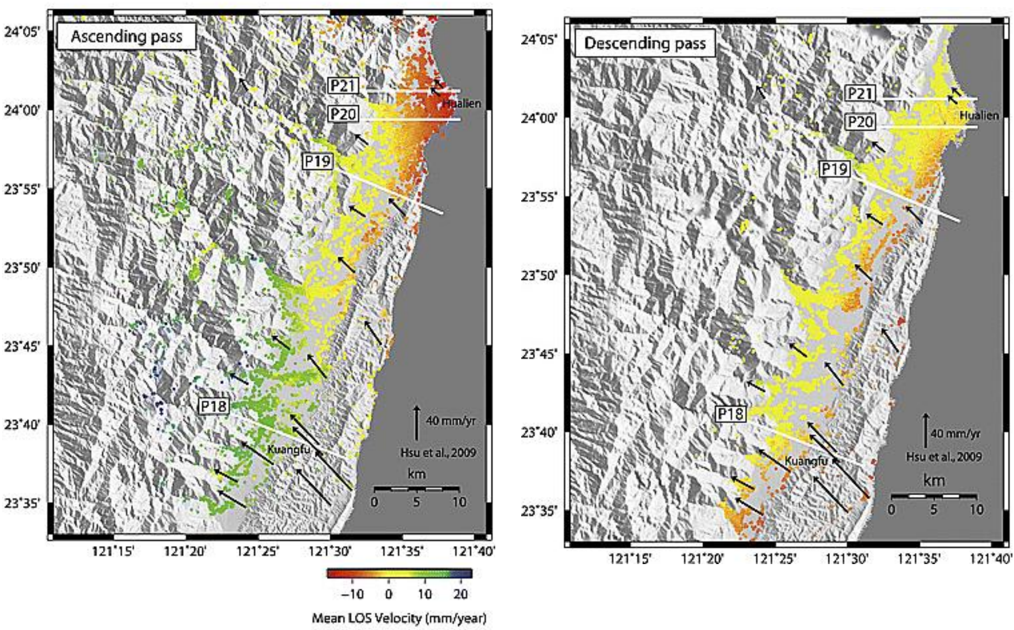

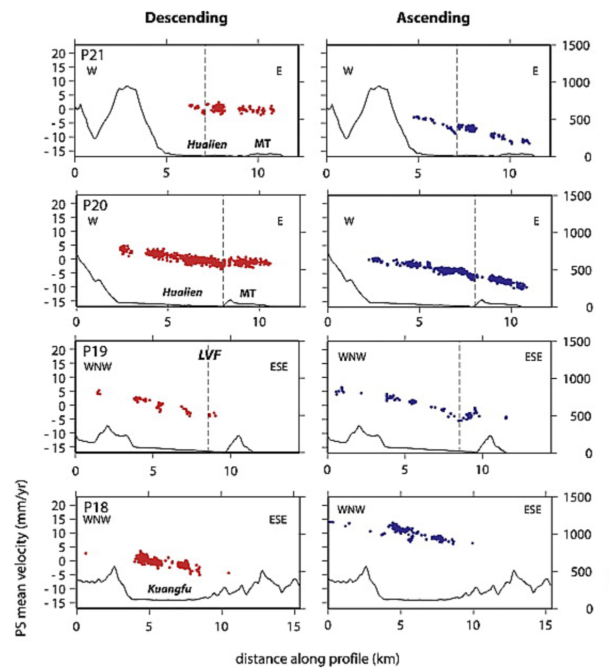

PS mean velocity map in the ascending (left) and descending (right) in North LV between Rueisuei and Hualien. White lines show the location of the profiles presented in the right panel. No significant change across the LV, completely locked fault!

Some profiles of PS mean velocities in North LV, superimposed on the topographic profile. Black dotted lines show the location of small localized changes in the velocity map.

Peyret et al., 2011

Structure

- Introduction to Plate Tectonics
- InSAR and earthquakes
- InSAR and postseismic deformation
- InSAR and interseismic deformation
- InSAR and volcano deformation
- InSAR and landslides
- InSAR and anthropogenic deformation

  [see also Module 3101: Anthroposphere – SAR Interferometry]

InSAR and volcano deformation

- **Goal:**
  - To measure ground deformation caused by pressure change of a magma chamber (influx/outflux of magma), intrusion of sills and dikes, changes in local hydrothermal system or gravitational spreading
  - To map the spatial extent and thickness of lava flows during an eruption

- **Methodology:**
  - Repeat-pass interferometry (e.g. for co-eruption analysis) and time-series methods such as SBAS and PS (for pre-eruption and post-eruption monitoring)

- **Main models:**
  - Mogi source (Mogi, 1958), finite sphere (McTigue, 1987), dislocation source (sill or dike source) (Okada, 1985), ellipsoid source (Davis, 1986; Yang et al , 1988), penny-crack source (Fialko et al., 2001)

Volcano deformation

- Many volcanic eruptions are commonly preceded by periods of inflation resulting from magma chamber pressurization caused by magma intrusion

- After an eruption the magma chamber deflates and ground surface subsides (deflation period)

- Monitoring inflation and deflation periods provides important clues about the structure and the sate of active volcanoes

- Monitoring typical background surface deformation at volcanoes also helps detects the first sign of increase in the level of volcano activity, seismic precursors and magma ascent

SAREDU Remote Sensing Education Initiative

Volcano deformation

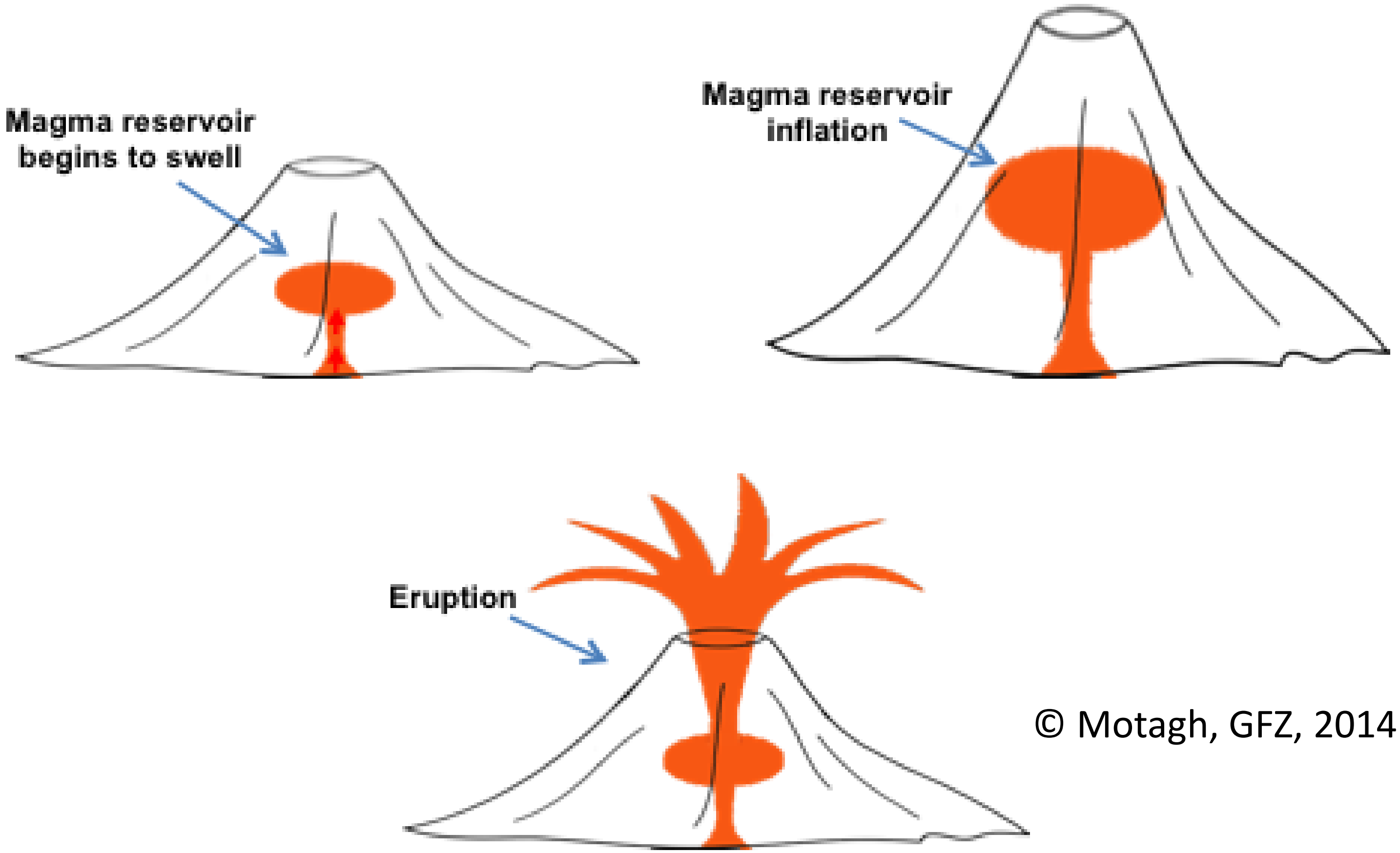

© Motagh, GFZ, 2014

Error sources

- Atmospheric noise over cloud-prone and rainy regions
- Baseline uncertainty
- DEM errors in volcanoes with steep topography
- Coherence loss due to snow/ice melting, vegetation cover, freezing/thawing of surface material, erosion and deposition of volcanic ash and lava

(a) (b)

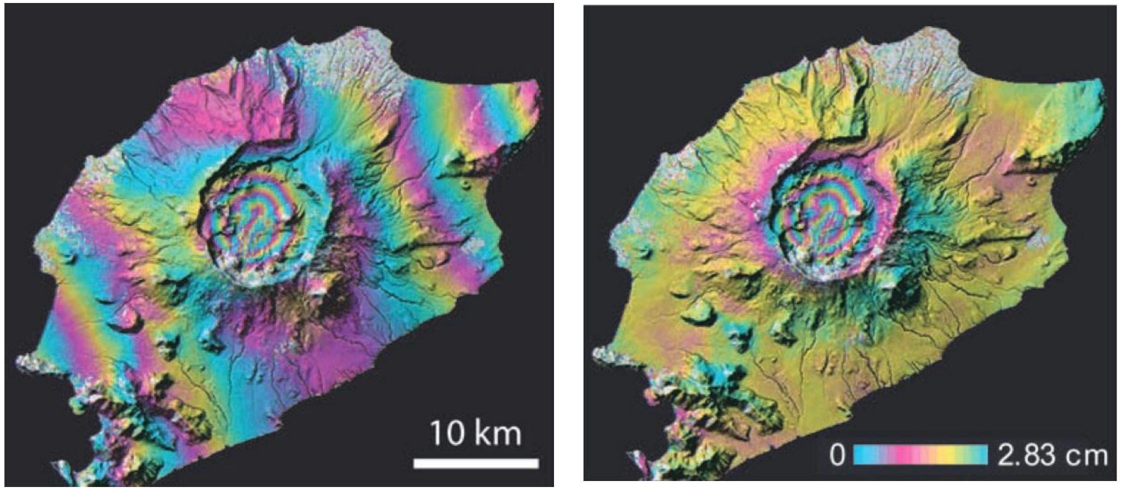

- Differential ERS2 interferogram of Okmok Volcano in the Aleutian island (Alaska) before (a) and after (b) orbital error correction

Lu, 2007

Error sources

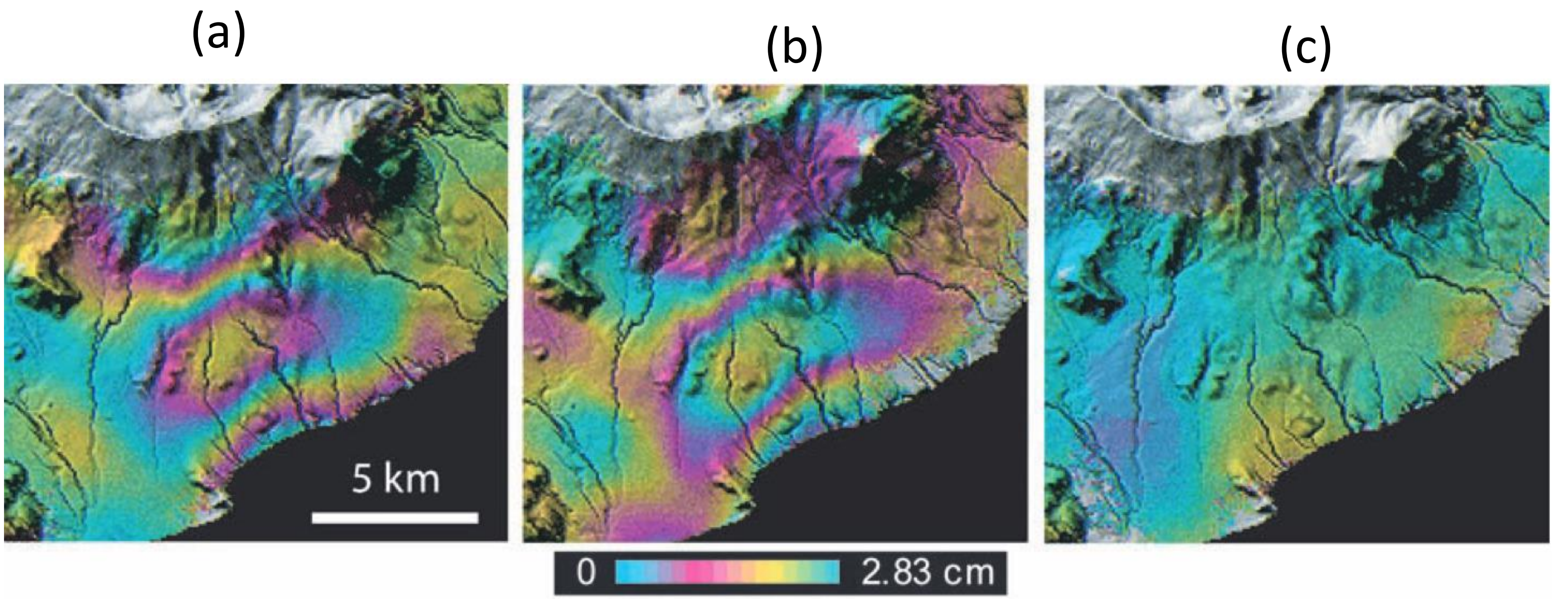

- Atmospheric water vapour effects on southeastern part of the of Okmok Volcano, Alaska. (a) May to July 1997, (b) July to September 1997, (c) May to September 1997

Lu, 2007

Deformation Modeling

- Similar to the earthquake source parameter estimation, the relation between observed surface deformation and source geometry parameters in volcanoes can generally be expressed by a non-linear equation:

$$d = G(m) + e$$

d=observed deformation
m= source parameters
G= Green function relating surface displacement to the source geometry (e.g. Mogi, McTigue, Okada,…)
ε= observation error

SAREDU Remote Sensing Education Initiative

Some analytical sources for volcano deformation modeling

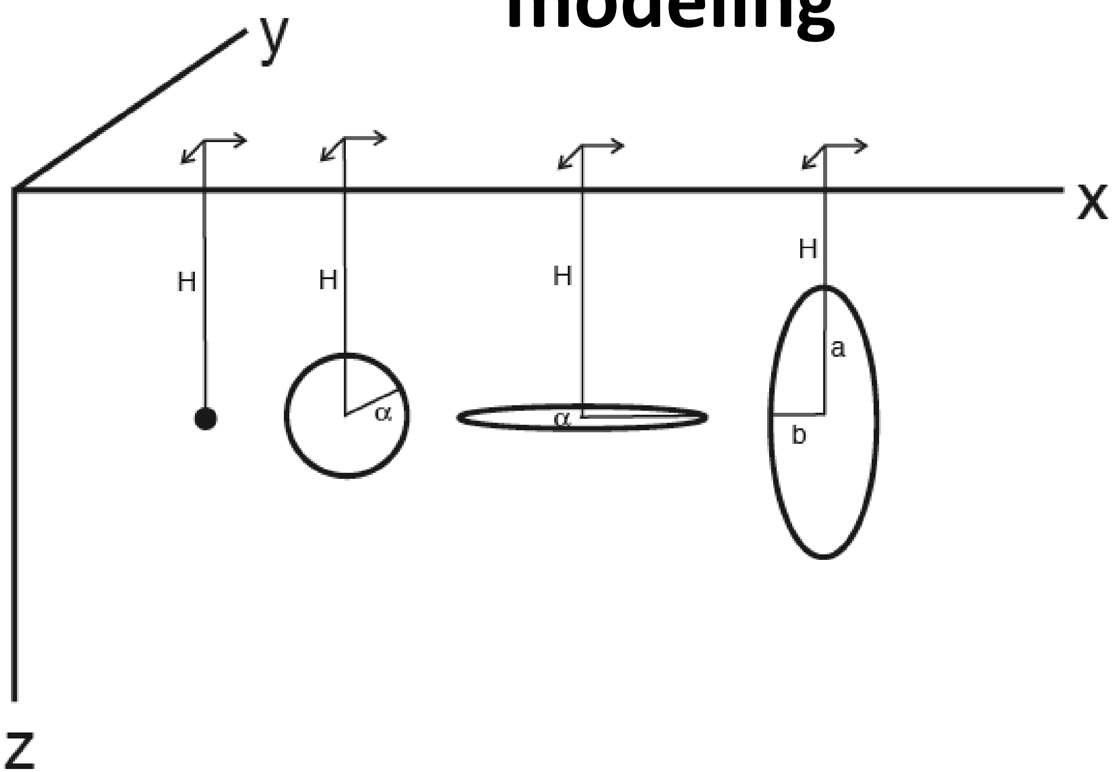

Sketch of some source geometries typically employed for source inversion from geodetic data. From left: Mogi-type point (Mogi, 1958), finite sphere (McTigue, 1987), penny-shaped crack (Fialko et al., 2001) and prolate spheroid source (Yang et al., 1988).

Gottsmann et al., 2006

SAREDU Remote Sensing Education Initiative

Deformation Modeling

- The source characteristics and parameters can be estimated using both forward (trial and error) and inverse models (nonlinear inversion)

Forward Model

$$d = G(m)$$

displacement

Green function (Mogi, penny, etc..)

Source parameters

Inverse Model

$$m = G^{-1}(d)$$

SAREDU Remote Sensing Education Initiative

Pressure point source (Mogi, 1958)

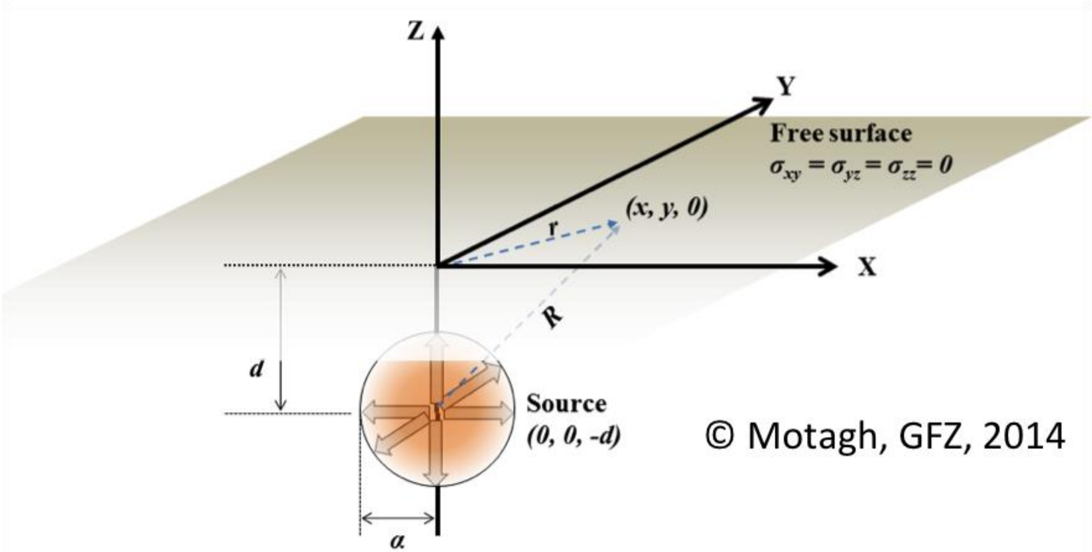

© Motagh, GFZ, 2014

$$a/d \rightarrow 0$$

$$\begin{pmatrix} u \\ v \\ w \end{pmatrix} = a^3 \Delta P \frac{1-\nu}{G} \begin{pmatrix} \frac{x}{R^3} \\ \frac{y}{R^3} \\ \frac{d}{R^3} \end{pmatrix}$$

$$\Delta V = \frac{\pi a^3 \Delta P}{G}$$

α= radius of sphere
ΔP= pressure change
d= source depth
G= shear modulus
ν= Poisson's ratio
R= radial distance from the source ($\sqrt{x^2+y^2+d^2}$)
u,v,w= surface displacement in east, north and vertical directions
ΔV=Volume change

Dzurisin, 2007

Pressure point source (Mogi, 1958)

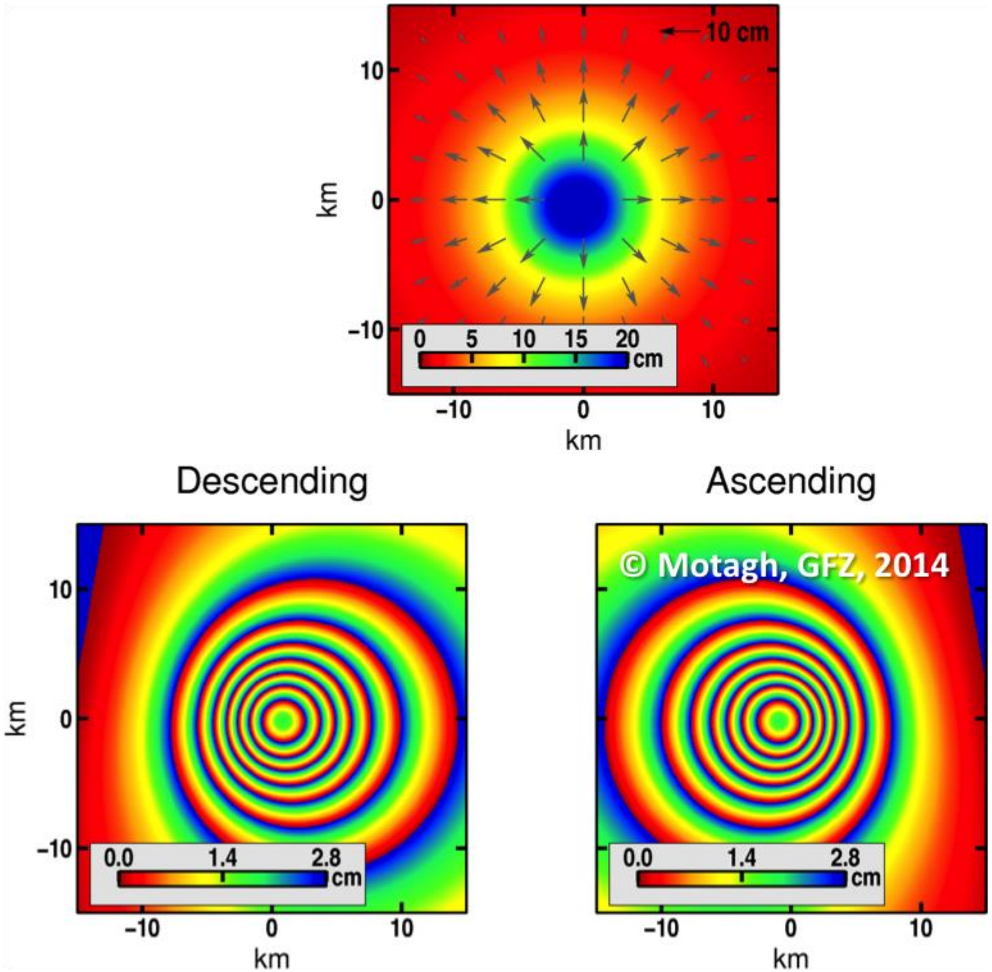

- Surface deformation due to a mogi source 6.5 km deep and a volume change of 0.04 km^3. The color shows vertical deformation

- Simulated descending (heading=190°, incidence angle=23°) and ascending (heading=350°, incidence angle=23°) interferogram.

SAREDU Remote Sensing Education Initiative

Finite spherical pressure source (McTigue, 1978)

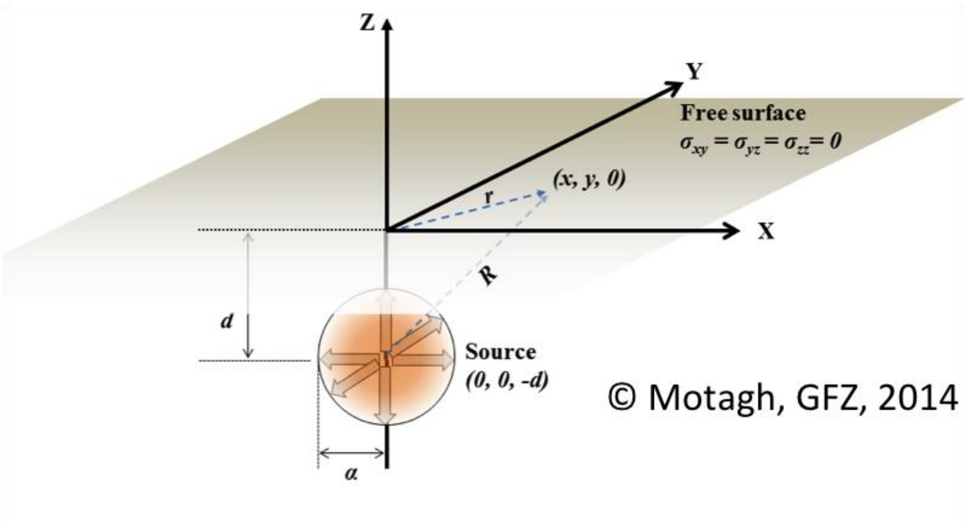

$$a/d > 0$$

$$\begin{pmatrix} u \\ v \\ w \end{pmatrix} = \left(\alpha^3 \Delta P \frac{(1-\nu)}{G} \left(\left(1 + \left(\frac{\alpha}{d}\right)^3 \times \left(\frac{(1+\nu)}{2(-7+5\nu)} + \frac{15d^2(-2+\nu)}{4R^2(-7+5\nu)}\right)\right)\right)\right) \begin{pmatrix} \frac{x}{R^3} \\ \frac{y}{R^3} \\ \frac{d}{R^3} \end{pmatrix}$$

α= radius of sphere
ΔP= pressure change
d= source depth (α/d > 0)
G= shear modulus
ν= Poisson's ratio
R= radial distance from the source ($\sqrt{x^2+y^2+d^2}$)
u,v,w= surface displacement in east, north and vertical directions

Dzurisin, 2007

Dipping point and finite rectangular tension cracks

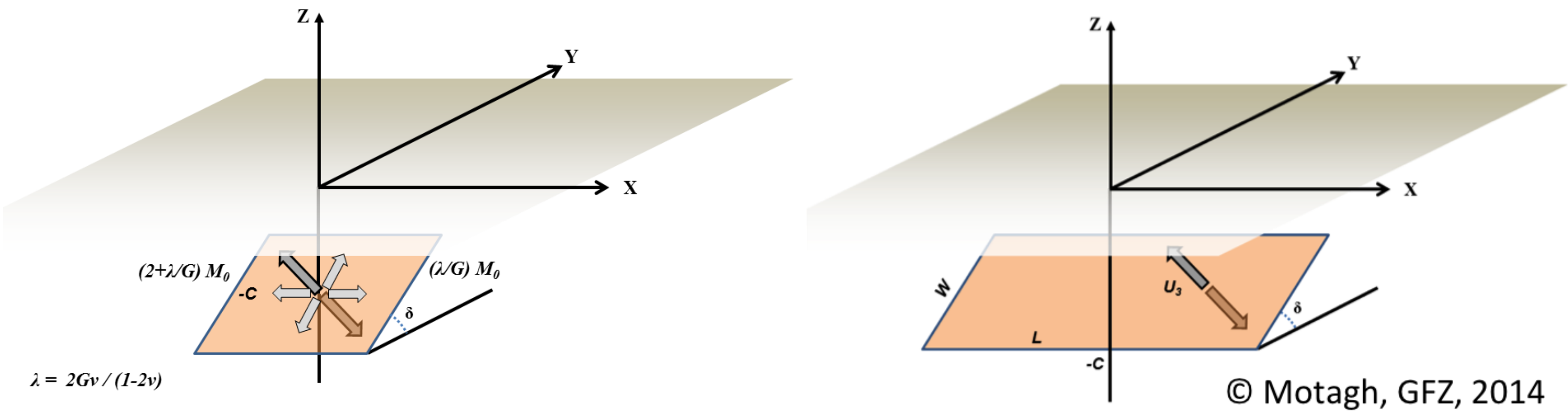

Dipping point (Left) and rectangular tension cracks (right) are used to approximate surface deformation caused by a tabular intrusions such as dikes or sills embedded in an elastic half space. M_0 in the left figure is the moment, equivalent to the amount of opening multiplied by the area and the shear modulus G.

(Okada, 1992) **(Dzurisin, 2007)**

SAREDU Remote Sensing Education Initiative

Tools

- **dMODELS**

  -A MATLAB code for modeling deformation near active faults and volcano centers (Battaglia et al. 2013)

  -The software can be downloaded

  http://pubs.usgs.gov/tm/13/b1/

  Or email to mbattaglia_AT_usgs.gov

- **A series of MATLAB codes developed by Prof. Yuri Fialko**

  Sioviz.ucsd.edu/~fialko/software.html

Example: Galapagos Islands

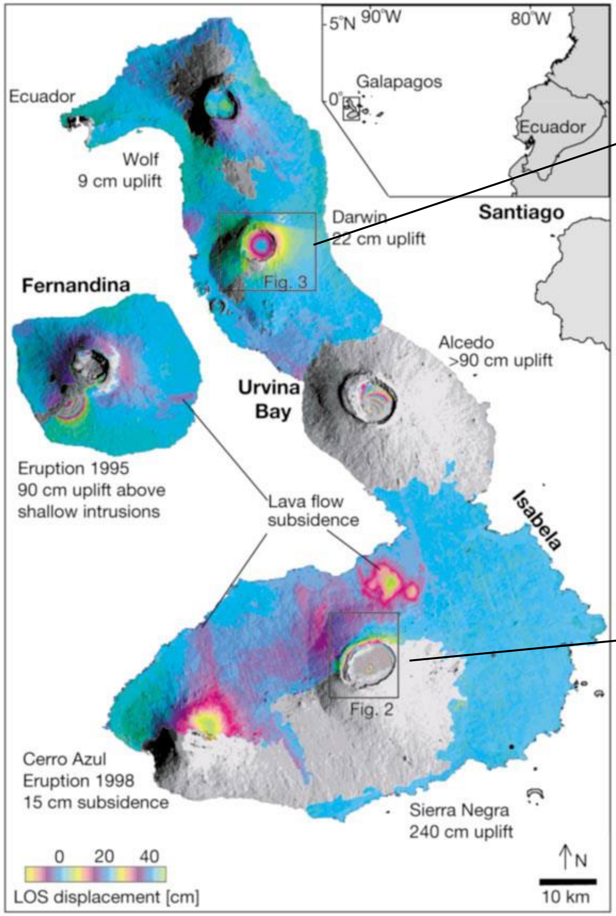

Semi-circular fringe pattern on the southwest flank of Fernandina volcano is due to the 1995 eruption

Darwin volcano

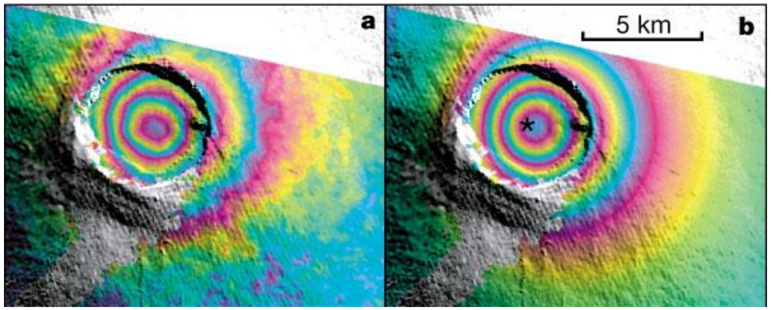

(a) 1992-98 uplift. (b) predicted deformation from a Mogi model with source location in the center of the caldera and depth of 3 km. Each color cycle represents 5 cm of LOS deformation

Transient deformation at Sierra Negra volcano

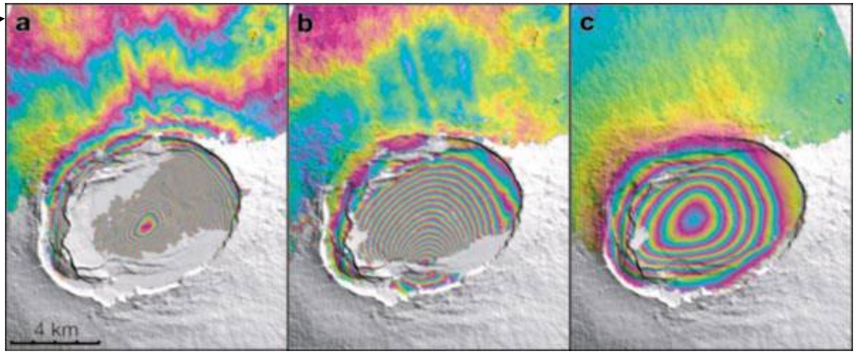

(a) 1992-97 (5.3 years) uplift. (b) 1997-98 (1.1 years) deformation, interpreted as trapdoor faulting. (c) 1998-99 (0.5 years) uplift. Each color cycle represents 5 cm of LOS deformation

SAREDU Remote Sensing Education Initiative

Amelung et al., 2000

Different deformation models for 1998-99 uplift period at Sierra Negra

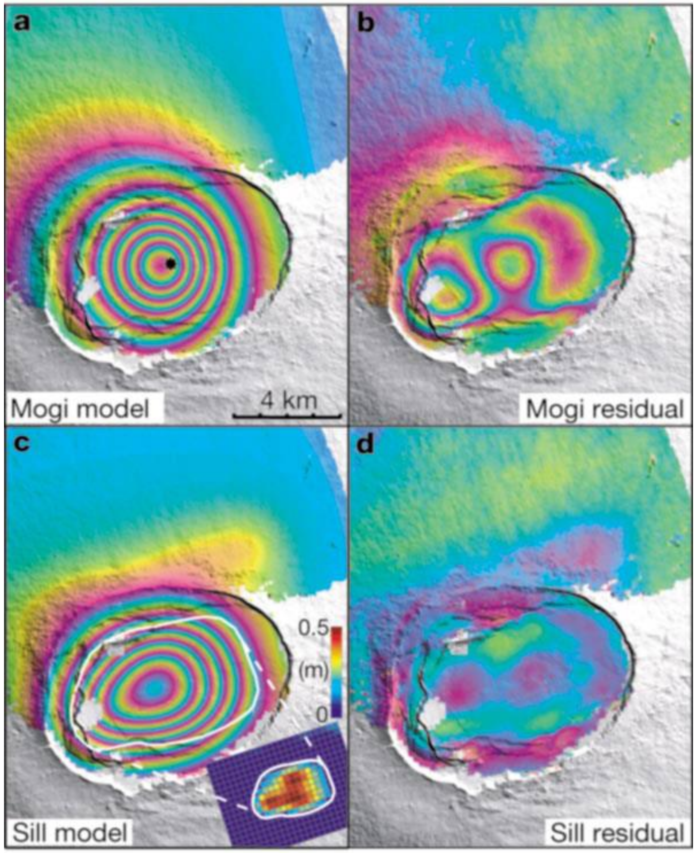

- a, b:

  Best-fit Mogi model leaves large residuals

- c, d:

  Horizontal sill at about 2 km depth with variable openings up to 0.5 m

Amelung et al., 2000

SAREDU
Remote Sensing Education Initiative

2005 Afar dyking episode

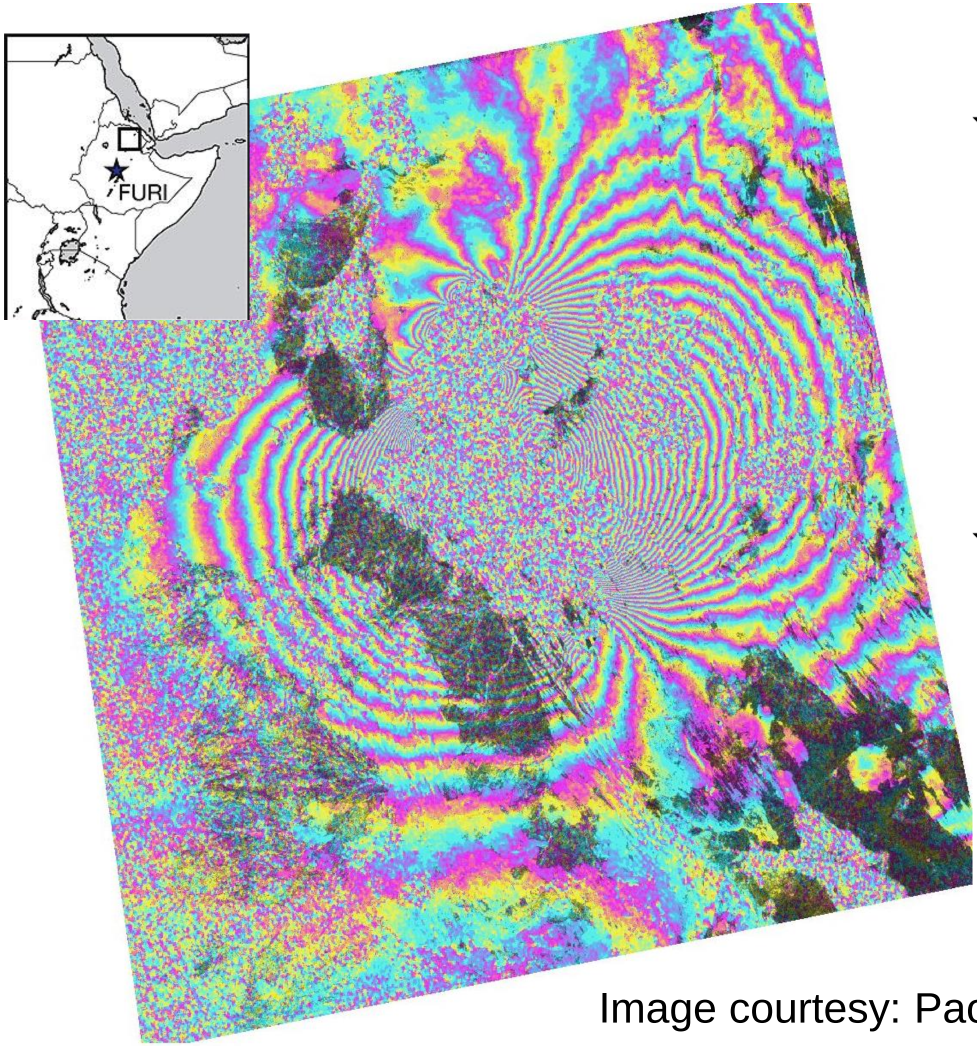

- More than 160 earthquakes (magnitude greater than 3.9) between 14 September and 4 October 2005
- Envisat Wide-Swath interferogram showing large deformation during the 2005 rifting period

Image courtesy: Paolo Pasquali

Source model for the 2005 Afar rifting event

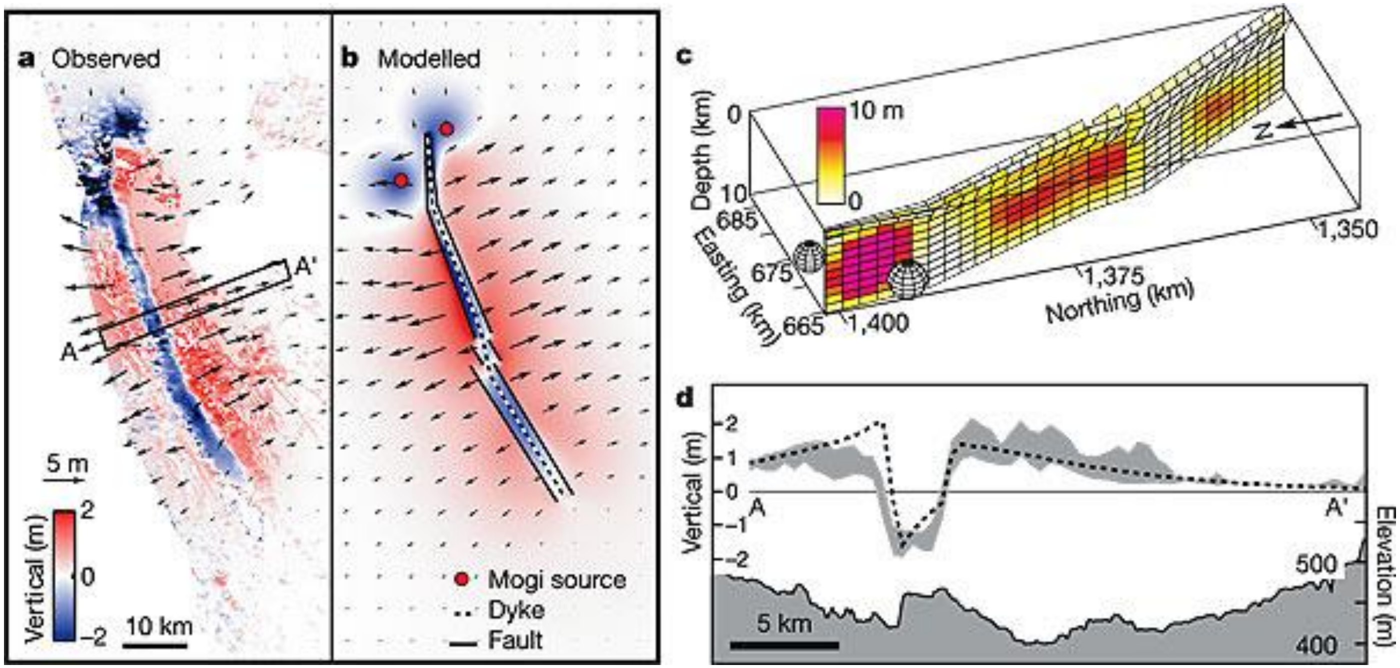

- 8 m of opening
- Dyke injection between depths of 2 and 9 km
- Intrusion volume of 2.5 km³

(a-b) Observed and modelled three-dimensional deformation field of 2005 Dabbahu rifting episode. (c) Source model of the deformation consisting of two deflating Mogi sources, shown as spheres, beneath Gabho and Dabbahu volcanoes and a vertical tensile dislocation (dyke intrusion) with variable openings of up to 8 m. (d) Profile across the dyke showing observed (Gray band, 1 σ error) and modelled (dashed line) vertical deformation.

Wright et al., 2006

Westdahl Volcano, Alaska: 29 November 1991 eruption

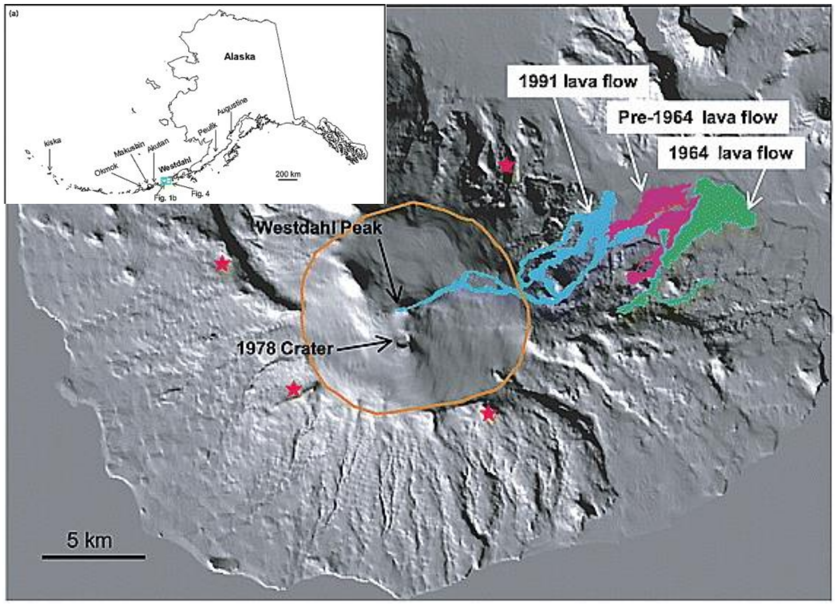

Shaded-relief map of Westdahl Volcano (Green square in the inset), Alaska. The orange line outlines the glacier on the volcano.

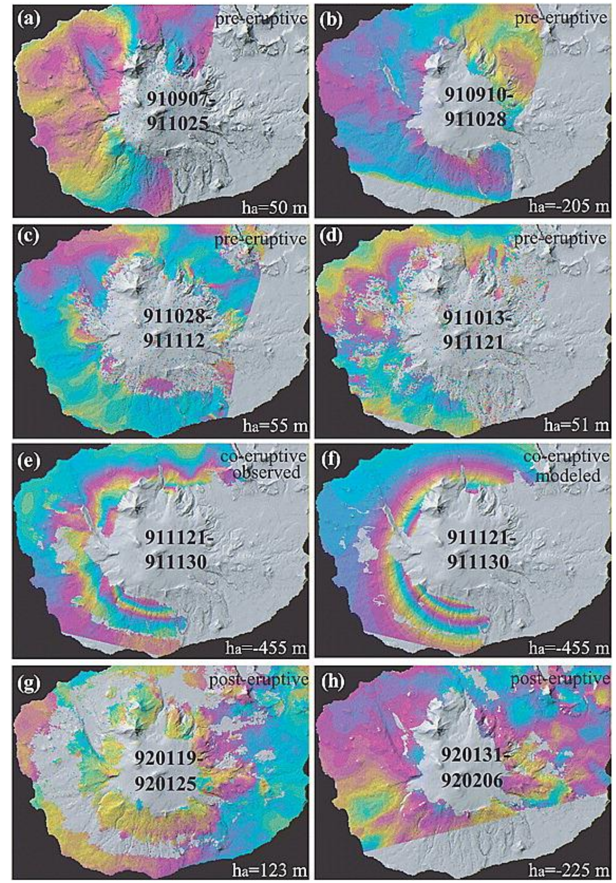

Several examples of transient deformation (a-e, g, h) of Westdahl volcano before, during and after the November 1991 eruption. (f) Modelled deformation for the 1991 eruption using a Mogi source. 1 color cycle = 2.8 cm of deformation.

Lu et al., 2003a

SAREDU Remote Sensing Education Initiative

Lava thickness estimation: 1997 eruption of Okmok Volcano, Alaska

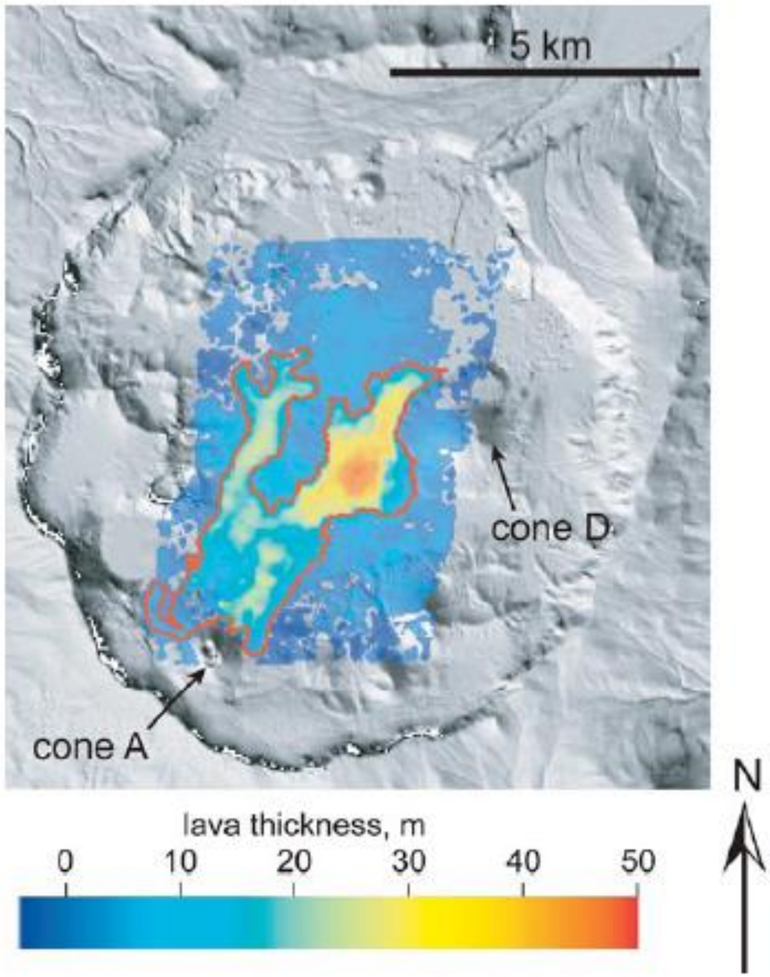

- Lava thickness derived from height difference between pre-eruption DEM (produced using ERS interferograms) and post-eruption DEM (produced using TOPSAR data)
- Red line is lava perimeter from field survey
- Aerial extent of lava ~ 9.8 km^2

Lu et al., 2003b

C-band and L-band interferometry: March 1996 earthquake swarm at Akutan Island, Alaska

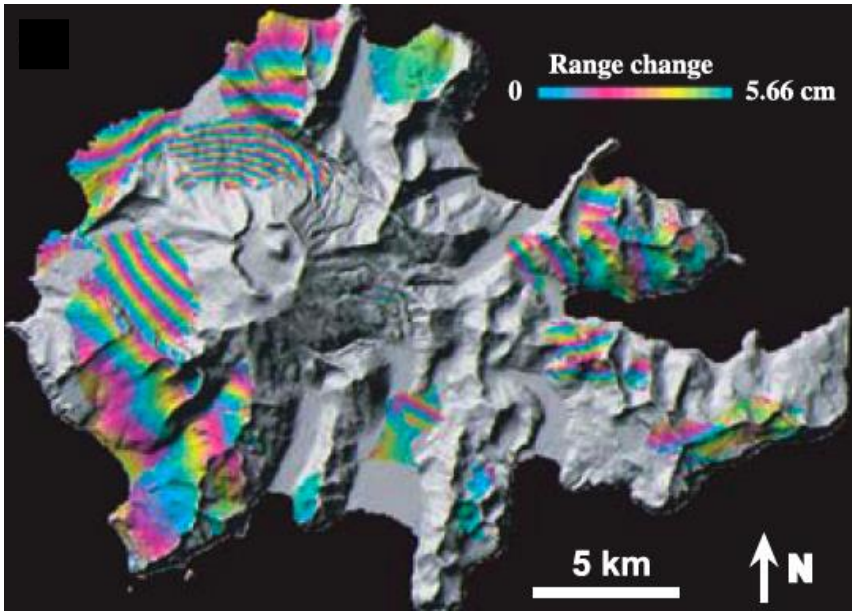

C-band ERS1/2 interferogram: June 1995-June 1997

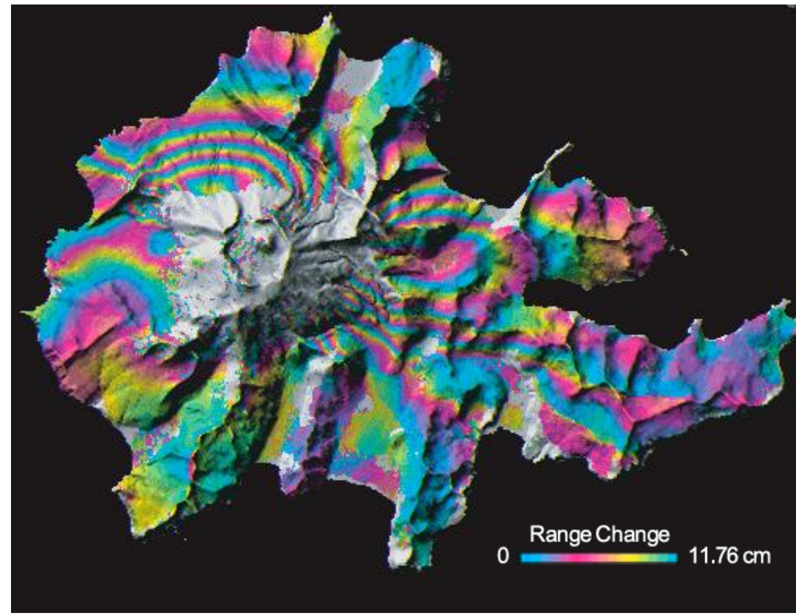

L-band JERS-1 interferogram: October 1994-June 1997

- L-band interferogram shows higher coherence than C-band interferogram in areas with loose surface material or thick vegetation
- As much as 60 cm of uplift associated with March 1996 earthquake swarm, but no eruption

Lu et al., 2005

SAREDU Remote Sensing Education Initiative

InSAR survey of volcanic centers in the central Andes

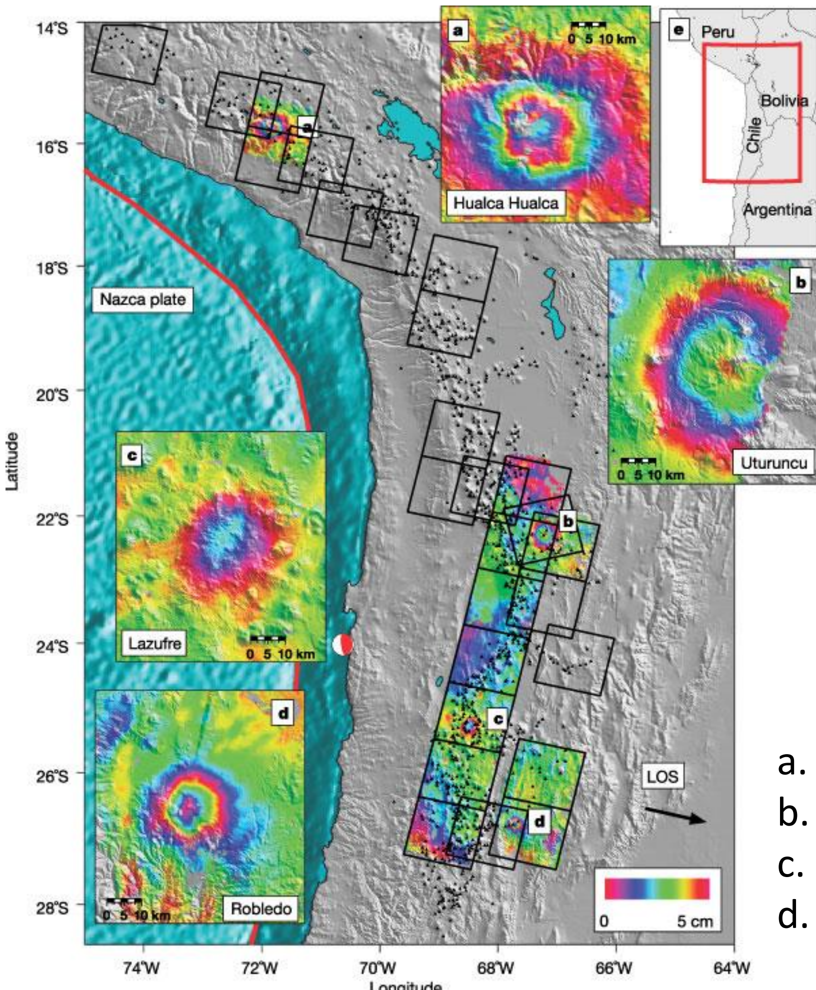

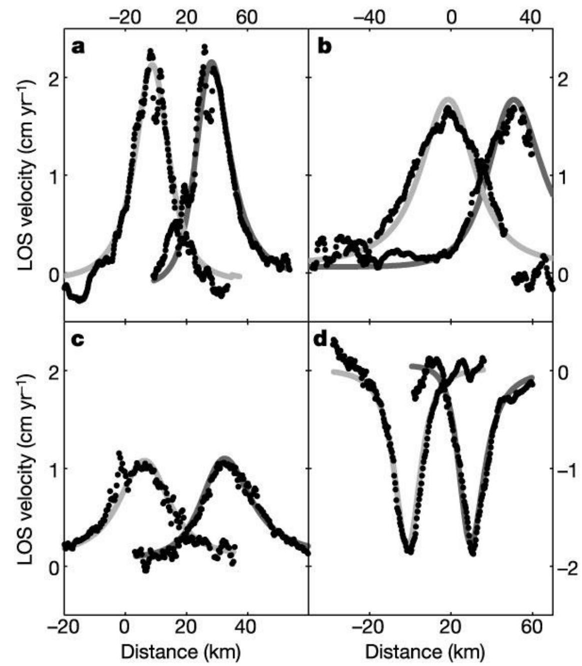

Light grey and dark grey correspond to SN and WE profiles, respectively, through the deformation areas

a. Hualca Hualca, Peru: uplift, June 1992-April 1996
b. Uturuncu, Bolivia: uplift, May 1996-December 2000
c. Lazufre, Chile: uplift, May 1996-December 2000
d. Robeldo, Argentina: subsidence, May 1996-October 2000

Pritchard & Simons, 2002

InSAR time-series analysis at Lazufre system

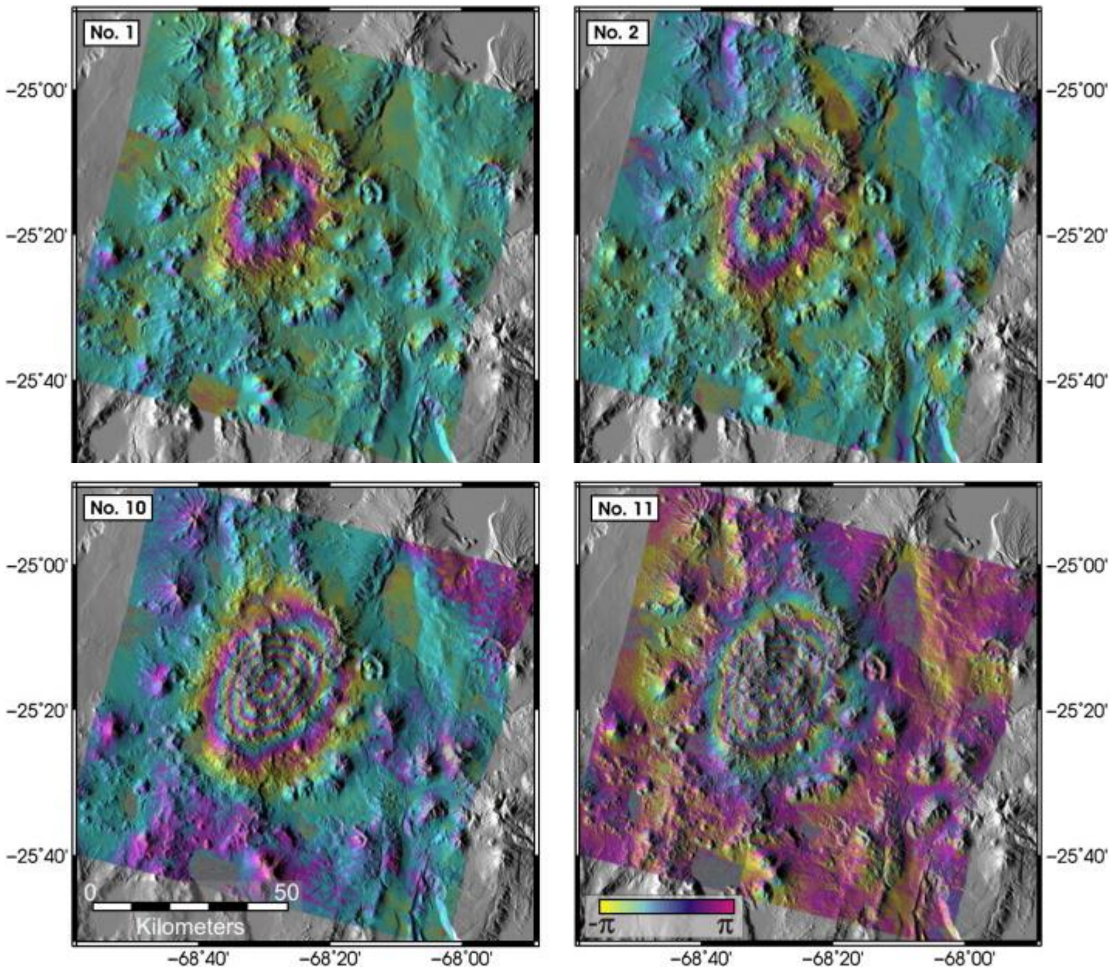

4 wrapped Envisat interferograms with respect to the master date on 9 March 2003:

No. 1: 630 d
No. 2: 805 d
No. 10: 1750 d
No. 11: 1820 d

Anderssohn et al., 2009

SAREDU Remote Sensing Education Initiative

InSAR time-series analysis at Lazufre system with SBAS method

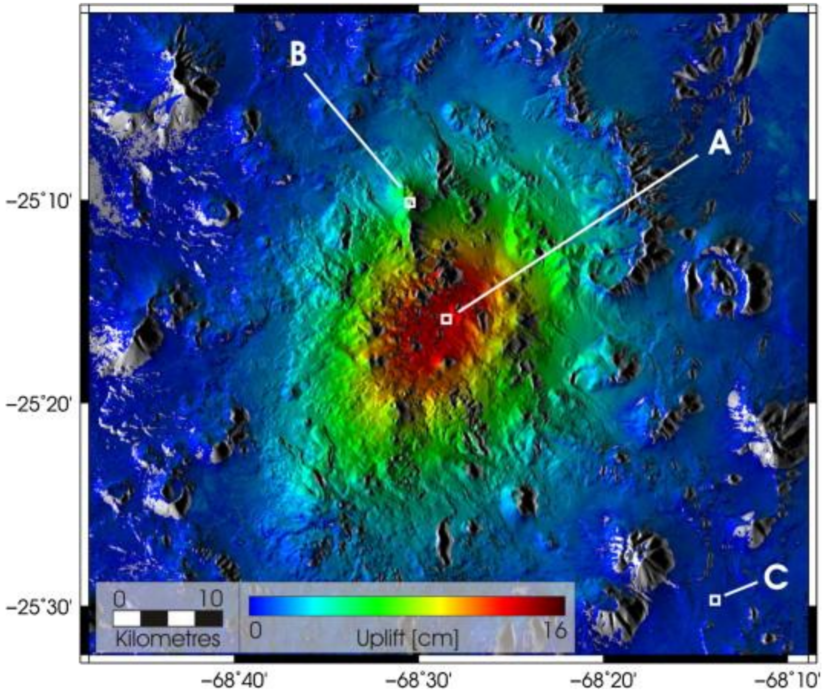

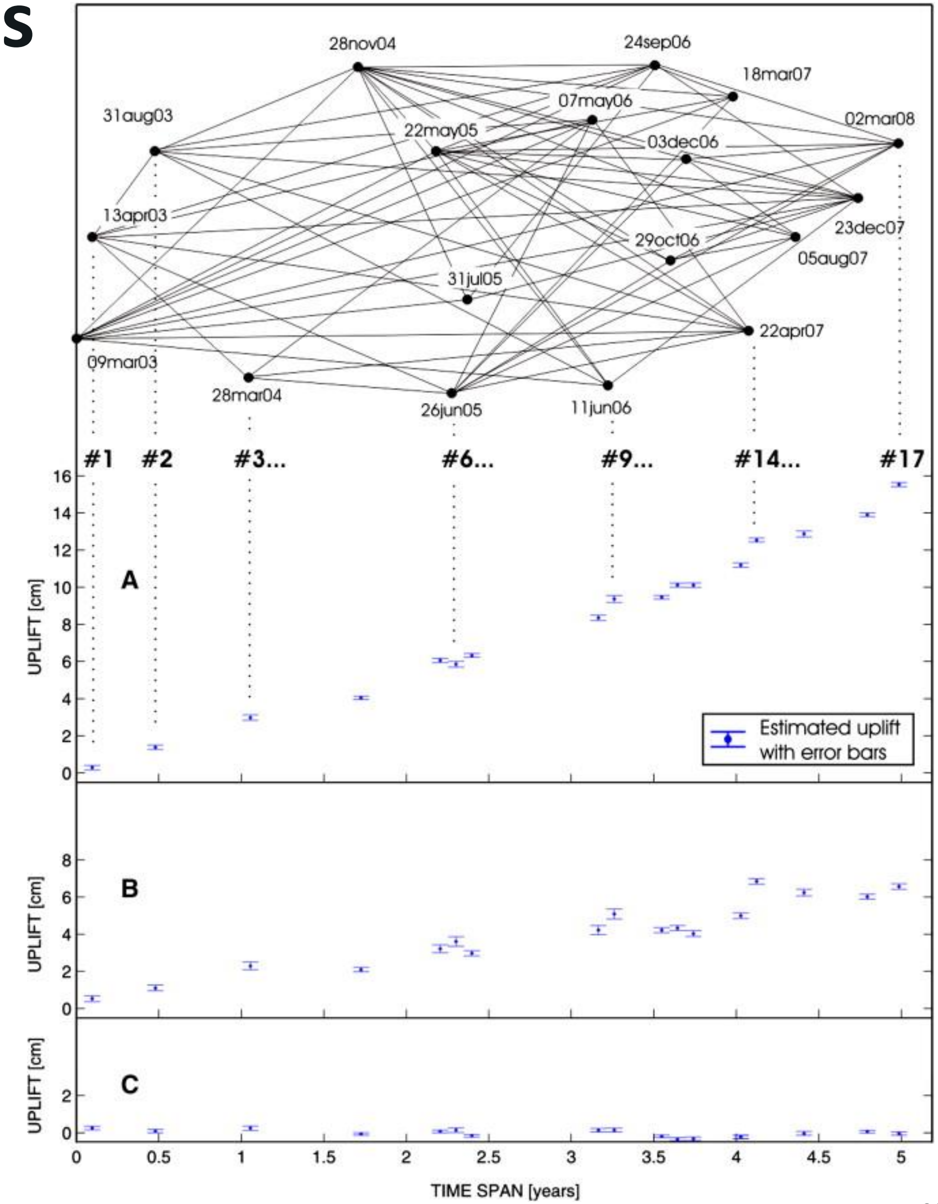

Anderssohn et al., 2009

Source modeling of the Lazufre system

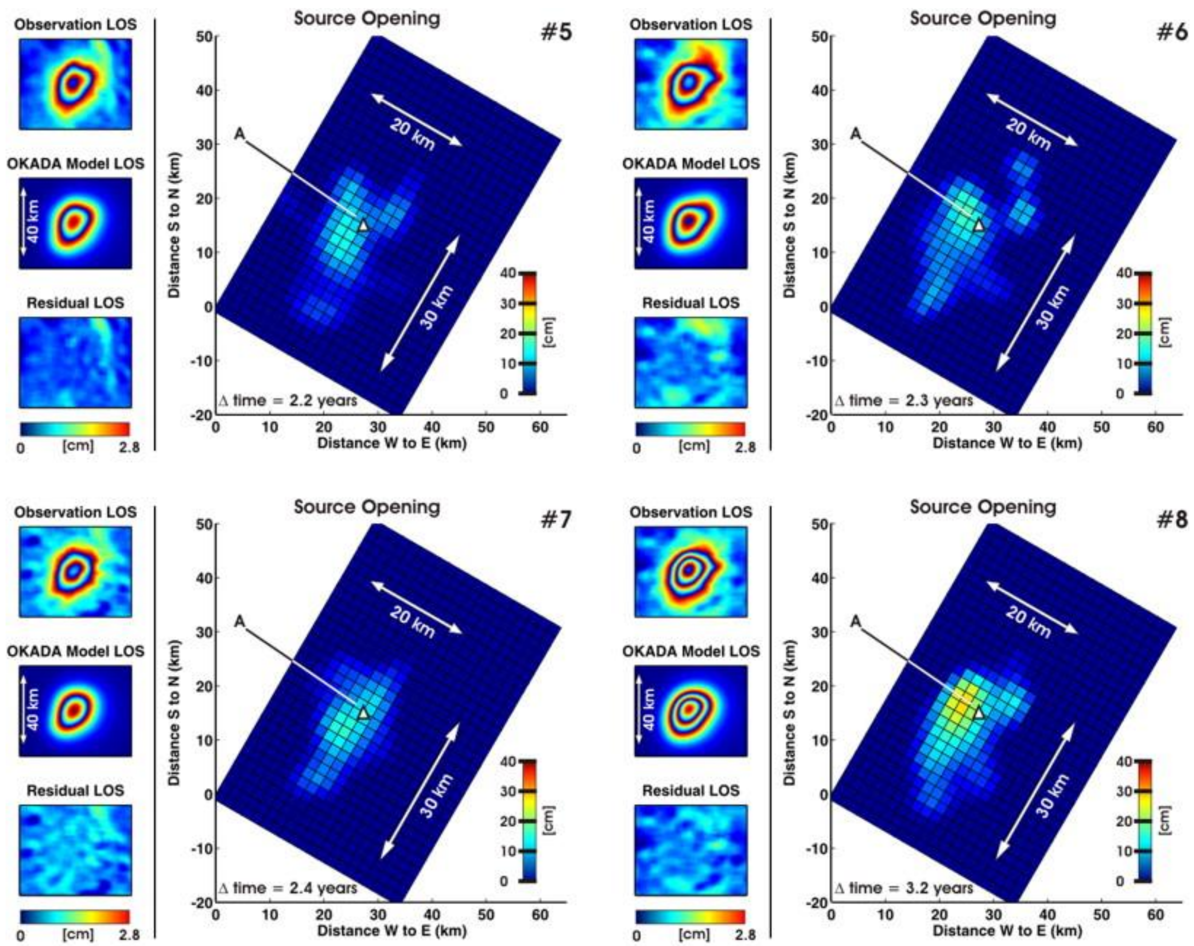

Plot of Okada modeling results (horizontally extended pressurized source, 10 km deep) for 4 selected displacement maps with respect to 9 March 2003.

No. 5: 1190 d
No. 6: 1295 d
No. 7: 1330 d
No. 8: 1470 d

Anderssohn et al., 2009

SAREDU Remote Sensing Education Initiative

Gravity-driven deformation of Tenerife (Canary Islands)

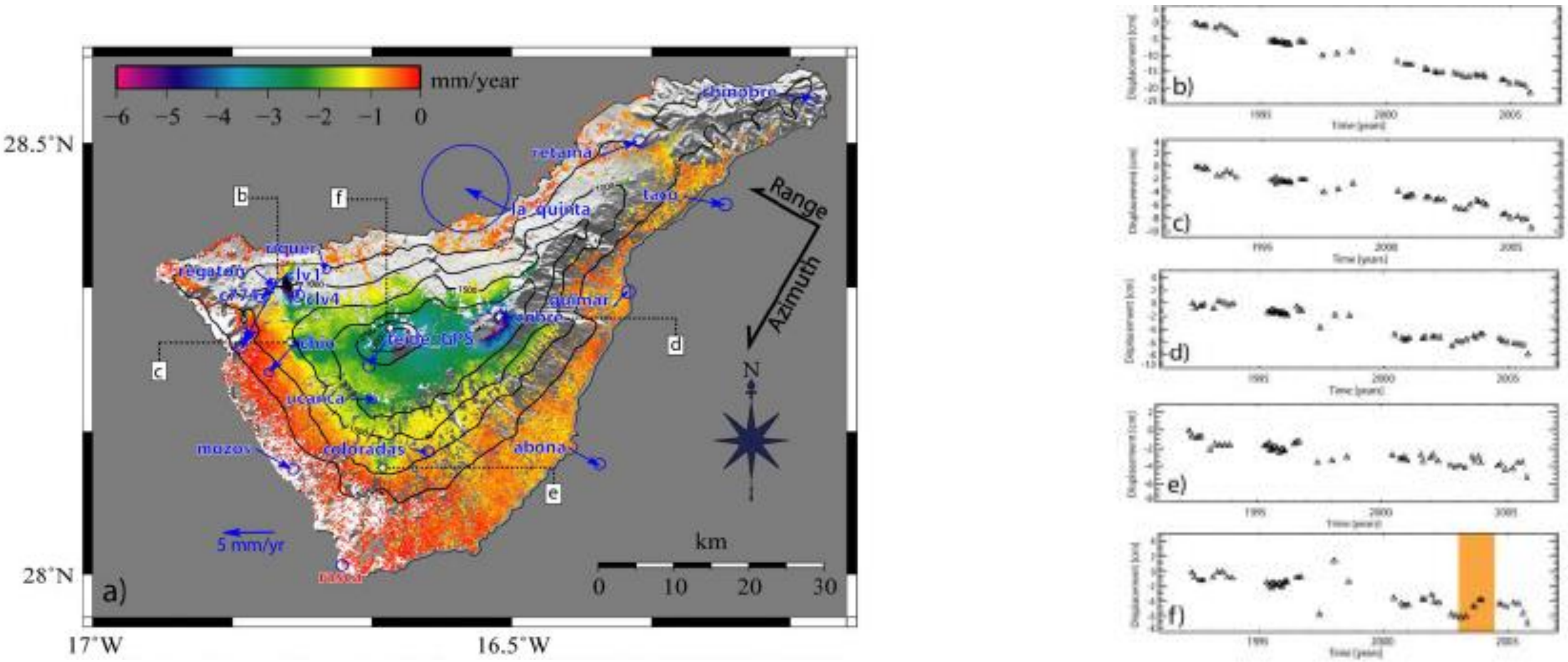

(left) Geocoded mean deformation rate map superimposed on the DEM of the island, computed from SBAS analysis of 55 ERS1/2 data during 1992-2005. Blue arrows show the horizontal displacement measured using GPS observations between 2000 and 2006. The white stars, labeled as ''b'', ''c'', ''d'', ''e'' and ''f'', identify pixels whose DInSAR LOS deformation time series are shown in panels (b–f) on the right. The subsidence has been attributed to gravitational sinking of the dense core of the island into a weak lithosphere.

Fernàndez et al., 2009

Structure

- Introduction to Plate Tectonics
- InSAR and earthquakes
- InSAR and postseismic deformation
- InSAR and interseismic deformation
- InSAR and volcano deformation
- InSAR and landslides
- InSAR and anthropogenic deformation

[see also Module 3101: Anthroposphere – SAR Interferometry]

InSAR and landslides

- **Goal:**
  - To measure small progressive slips (a few millimeter per year to some centimeters per day) associated with mass movement phenomena
  - To detect signs of post-failure reactivation associated with known or previously unmapped landslides
  - Slope instability assessment

- **Data requirement and methodology:**
  - At least two SAR images
  - For regional assessment in mountainous regions, preferably combination of ascending and descending pairs in order to reduce the effect of shadowing and layover
  - Multi-temporal time-series analysis to derive spatio-temporal evolution of slow-moving landslides with better accuracy

Suitability analysis: Example from ERS sensor

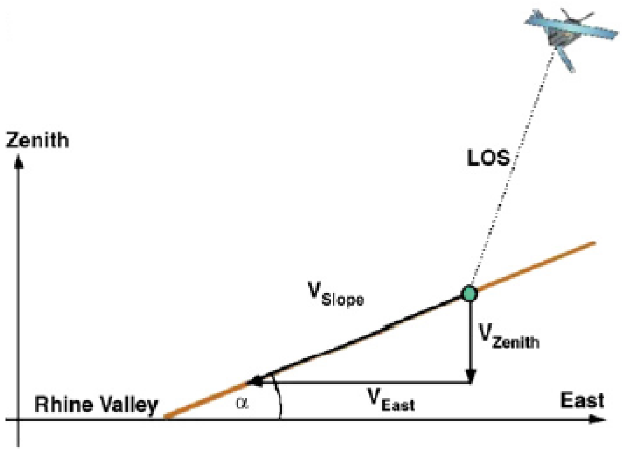

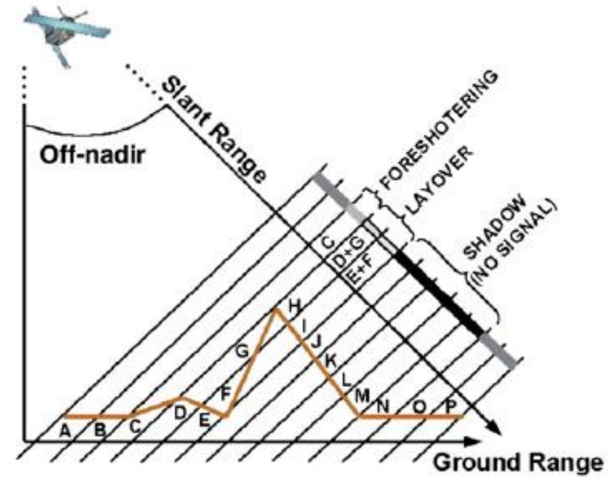

Slope aspect	Ascending ERS passes	Descending ERS passes	Notes
Slope facing East	Enhanced range resolution if $\|\alpha\|<67°$ Shadow if $\|\alpha\|>67°$	Foreshortening if $\|\alpha\|<23°$ Layover if $\|\alpha\|>23°$	Only ascending data suitable for SAR interferometry and feature extraction by means of image interpretation. Slopes exceeding 67° are not covered. 1D LOS deformation data.
Slope facing West	Foreshortening if $\|\alpha\|<23°$ Layover if $\|\alpha\|>23°$	Enhanced range resolution if $\|\alpha\|<67°$ Shadow if $\|\alpha\|>67°$	Only descending data suitable for SAR interferometry and feature extraction by means of image interpretation. Slopes exceeding 67° are not covered. 1D LOS deformation data.
Slope facing North or South	–	–	Both ascending and descending data are suitable for interferometry and feature extraction by means of image interpretation. 2D deformation analysis feasible. Low system sensitivity with respect to translational displacements along the North–South direction.

Colesanti & Wasowski , 2006

Geometry limitation for slopes facing away from the SAR sensor

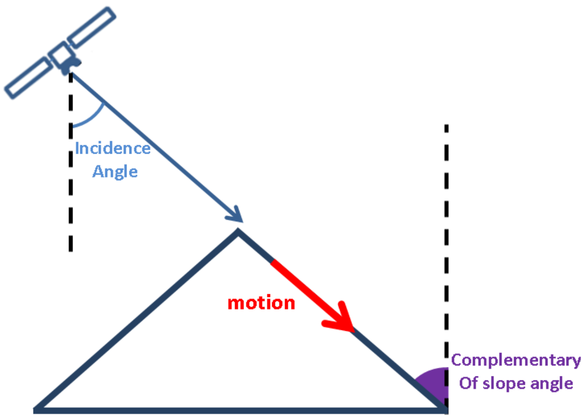

Perfect geometry
(incidence angle= complementary of the slope angle)

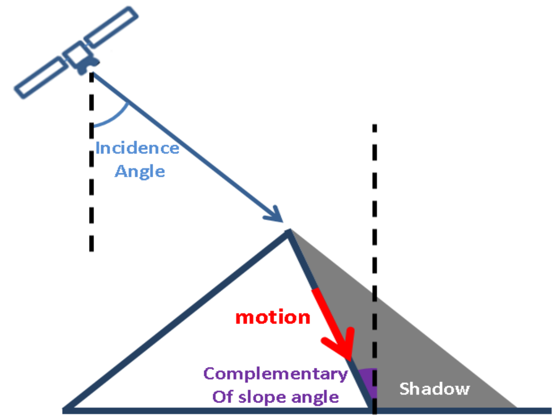

Bad geometry
(incidence angle > complementary of the slope angle)

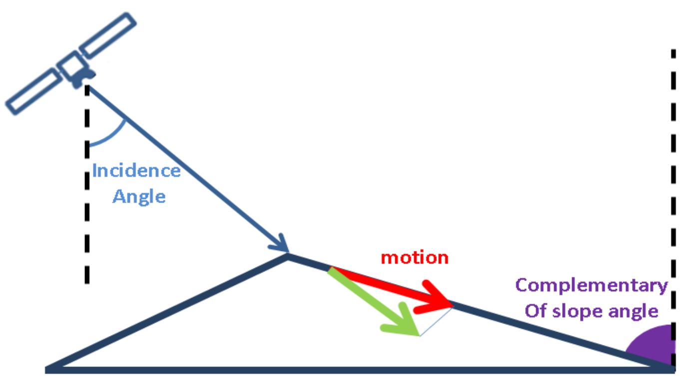

Suitable geometry
(incidence angle < complementary of the slope angle)

Requirements for practical applications of landslide monitoring using InSAR

- **Slide size**
  - approximately an order of magnitude larger than the resolution of the imaging SAR sensor
- **Surface type**
  - bare or low vegetation to mitigate temporal decorrelation
- **Low to moderate slope inclination**
- **Orientation with respect to the SAR geometry**
- **Very slow movements**
  - velocity less than a few centimeters per year. For moderately rapid displacements the use of InSAR is not feasible due to signal decorrelation!

Colesanti & Wasowski, 2006

SAREDU Remote Sensing Education Initiative

La Clapière landslide, SE France: results from ERS-1 InSAR

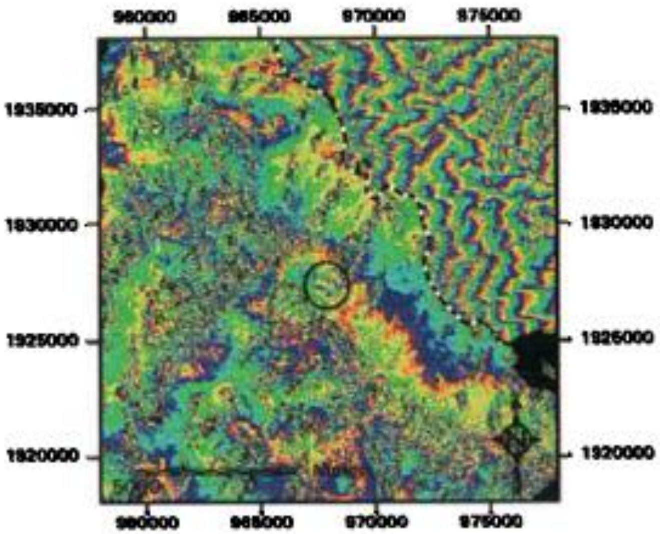

An example of ERS-1 interferogram of La Clapière landslide (circled), SE France. The temporal baseline is 9 days. The master date is August 20, 1991. The result has been projected on the geometry of the IGN 50-m-grid topographic model using a Lambert II projection.

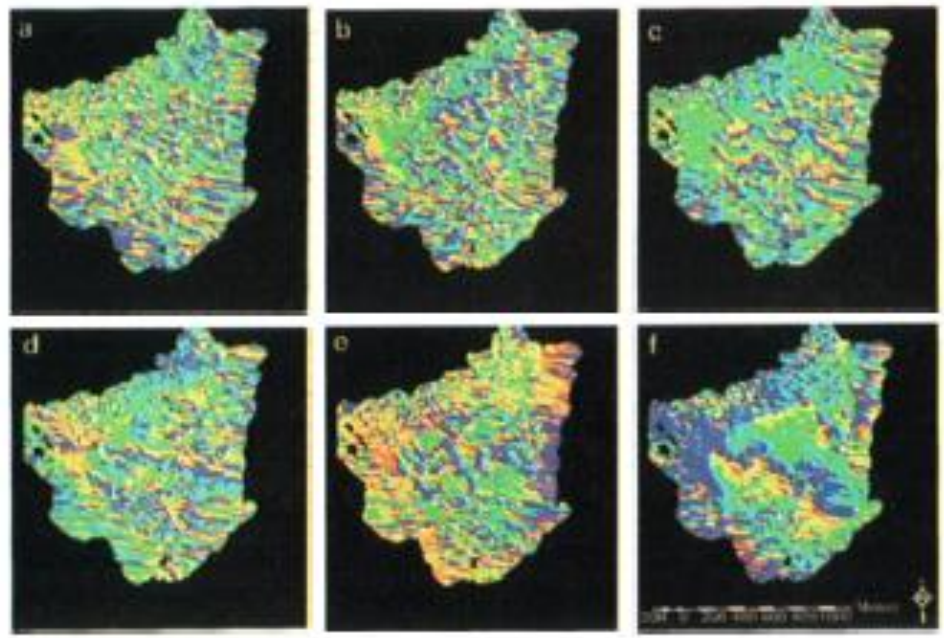

Six examples of ERS-1 interferograms on La Clapière landslide projected using the Lambert II topographic model (one full color cycle corresponds to 28 mm of range changes. The interferograms (a) to (f) are, (15 , 0, -31m), (15, 3, 32 m), (15, 6,-38 m), (15, 9,-31 m), (0, 9, 2200 m), (3, 6, 216 m), respectively: the first two numbers refer to the number of days since August 20, 1991, and the last number is the height ambiguity of interferograms.

Carnec et al., 1996

The Alta Badia region, Italy

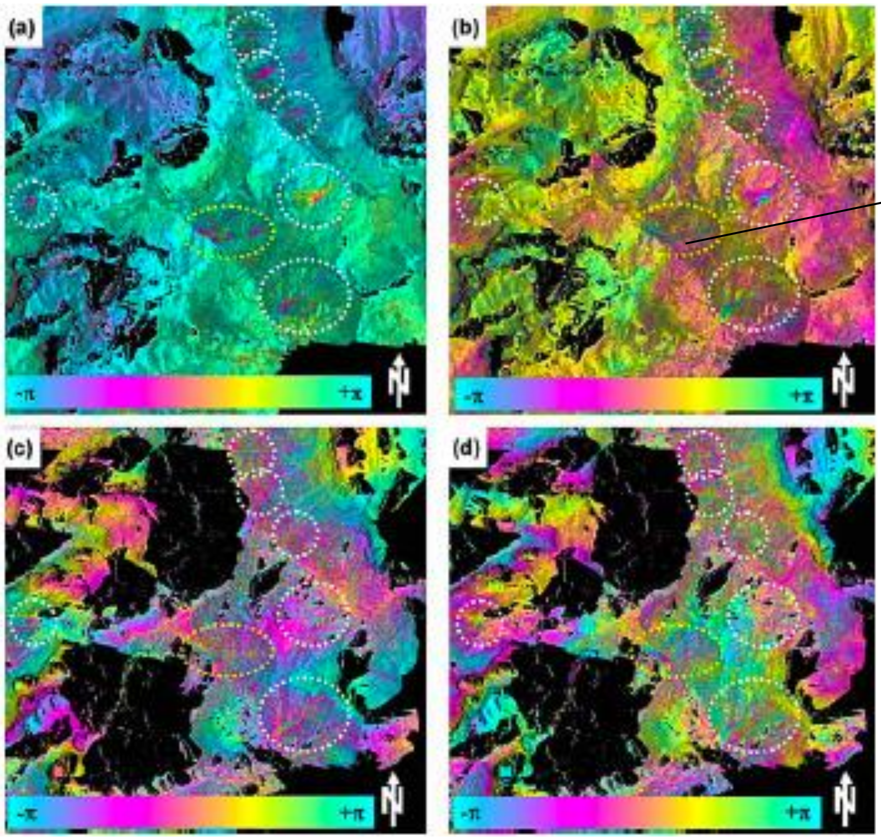

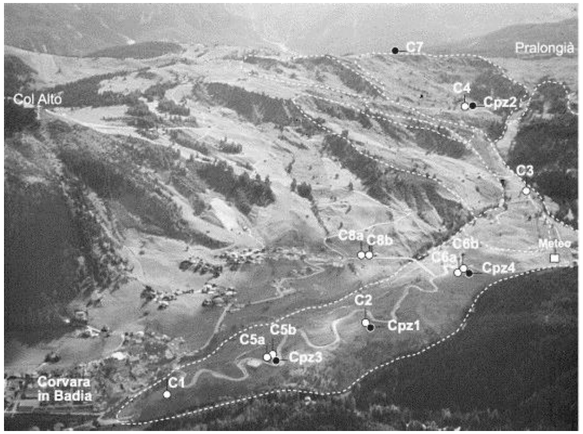

(a, b): JERS interferograms for 2 July-28 September 1998 and 11 August-7 November 1995, respectively
(c, d): ERS interferograms for 9 August-13 September 1997 and 13 September-18 October 1997, respectively

Yellow ellipse in the interferograms corresponds to Corvara landslide, a previously known landslide in the Alta Badia region, while white ellipses show evidence for ground deformation at other landslides in the region. Black is layover.

Strozzi et al., 2005

Triesenberg-Triesen landslide: deformation analysis using PS technique

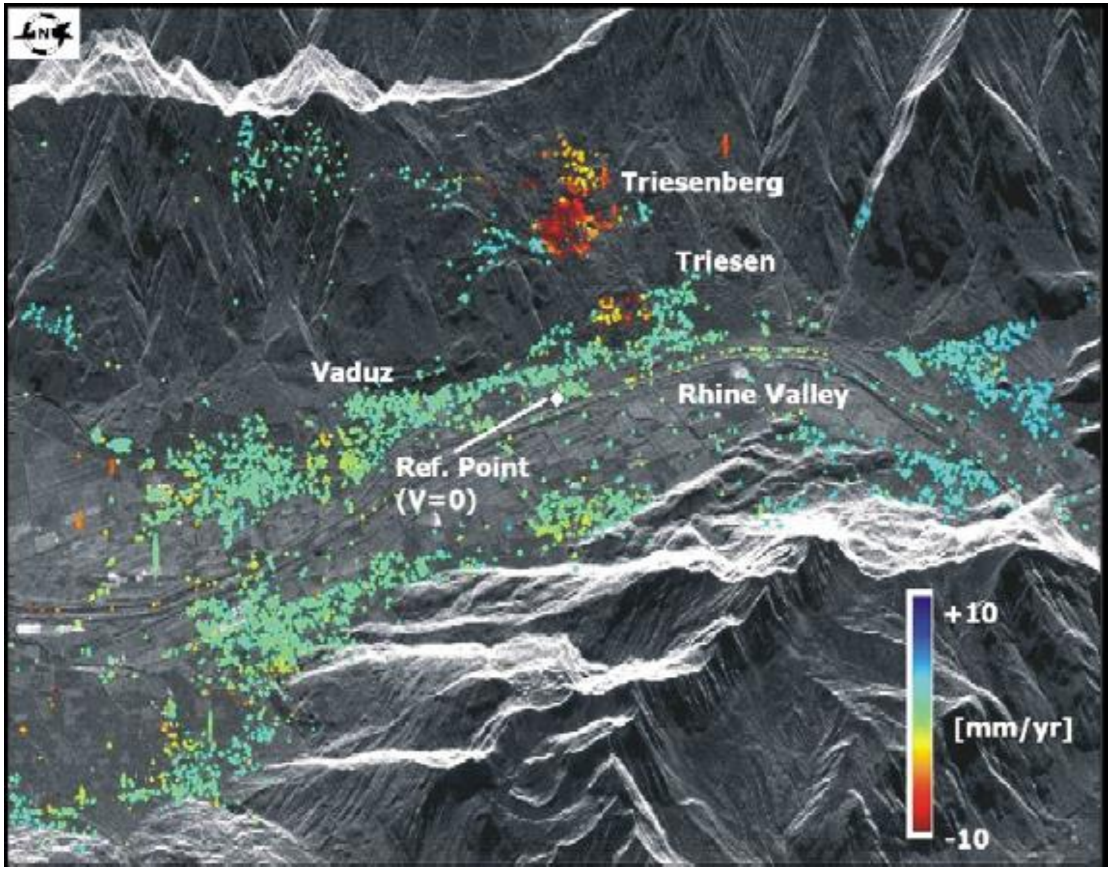

- Data: 38 descending ERS images during August 1992-August 2001
- Methodology: Permanent Scatterer (PS) technique

Colesanti & Wasowski, 2006

Aletschwald landslide: multi-sensor InSAR

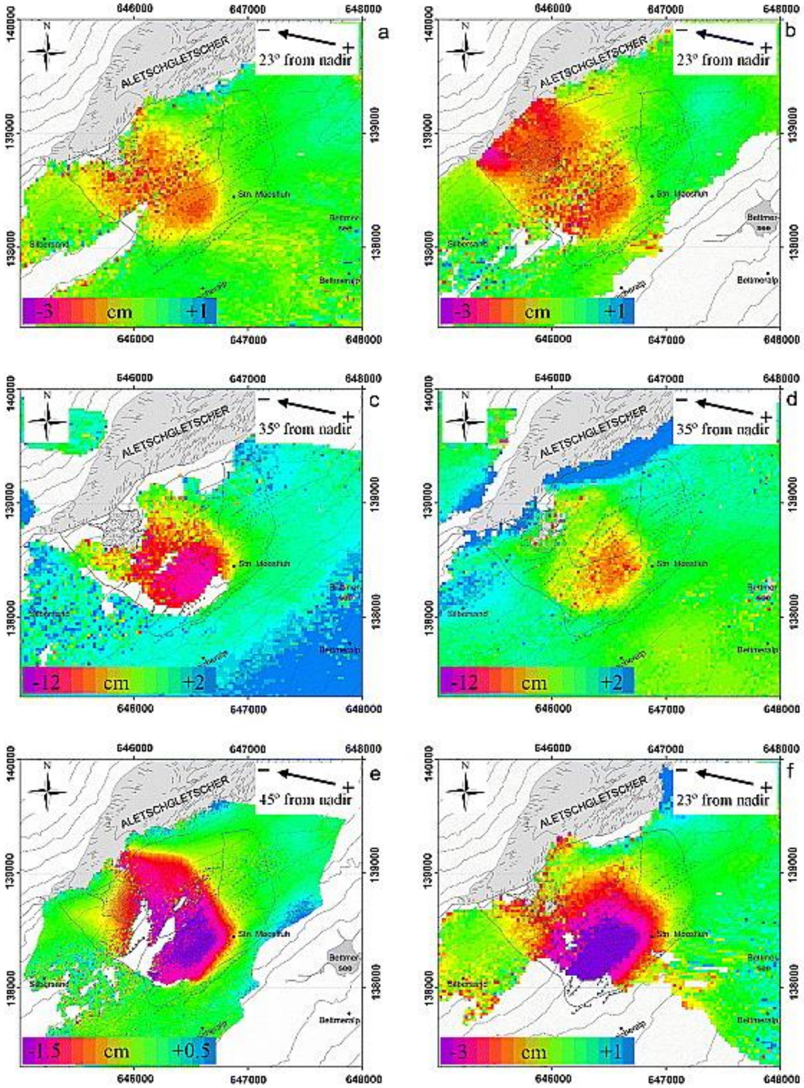

Aletschwald landslide in the Swiss Alps

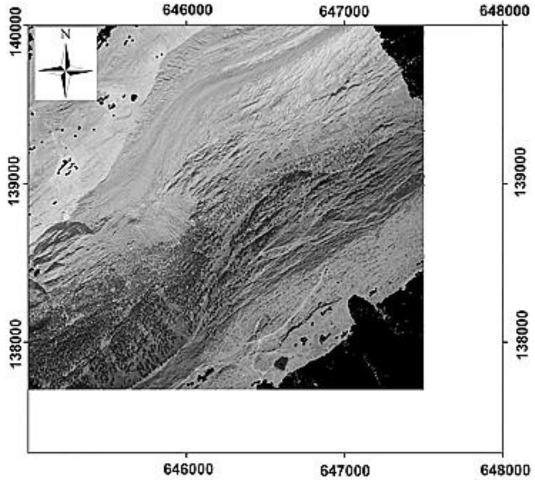

a: ERS SAR, 19921006_19930921
b: Envisat ASAR, 20070629_20070803
c: JERS SAR, 19930617_19960804
d: ALOS PALSAR, 20060613_20061029
e: TerraSAR-X, 20080822_20080913
f: ERS SAR, 19950811_19960726
(deformation in the LOS direction, negative sign is direction away from the satellite)

Strozzi et al., 2010

Structure

- Introduction to Plate Tectonics
- InSAR and earthquakes
- InSAR and postseismic deformation
- InSAR and interseismic deformation
- InSAR and volcano deformation
- InSAR and landslides
- InSAR and anthropogenic deformation

[see also Module 3101: Anthroposphere – SAR Interferometry]

InSAR and anthropogenic deformation

- **Goal:**
  - To measure ground surface deformation associated with anthropogenic phenomena (e.g. deformation due to withdrawal/injection of ground water or other fluids; for further application examples see also Module 3101 Anthroposphere – SAR Interferometry)
  - To understand hydrological properties of the aquifer system and their temporal and spatial variability

- **Data requirement and methodology:**
  - At least two SAR images
  - Multi-temporal time-series analysis to make maps of deformation time-series

Subsidence due to groundwater over-exploitation

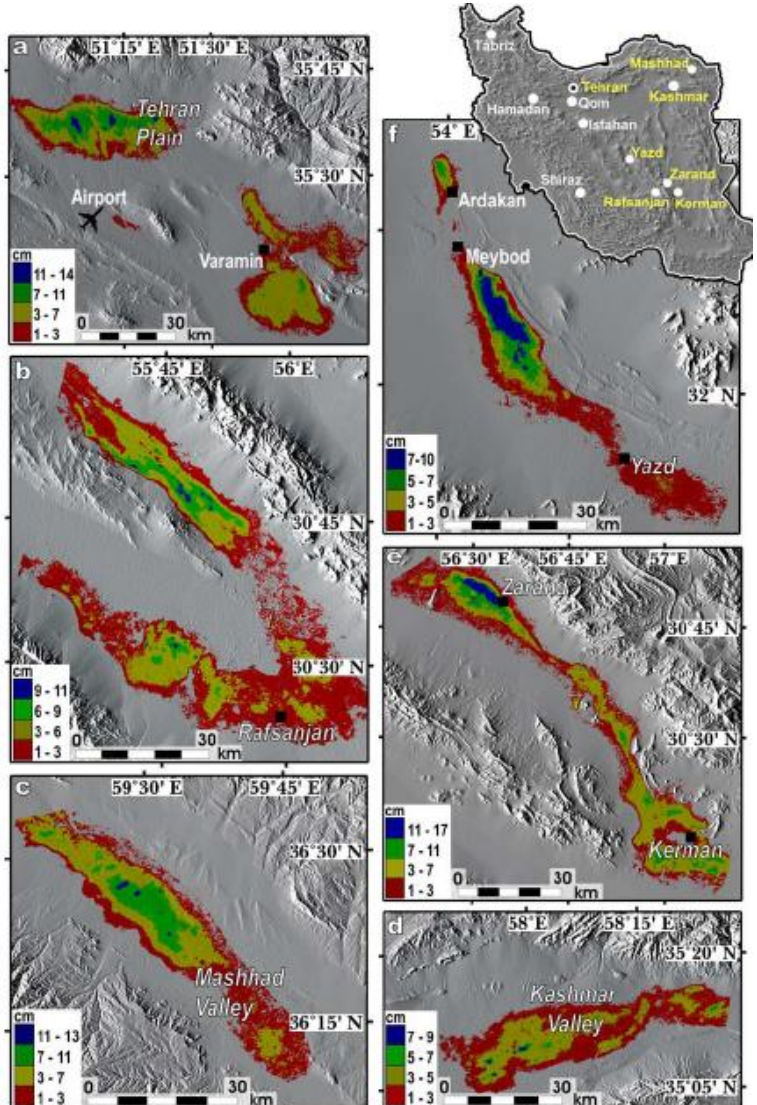

InSAR-derived subsidence maps (unwrapped, geocoded) showing ground-water related deformation in 6 regions of Iran, marked with yellow color in the upper inset.

(a) Tehran, time span: June - October 2004 (140 d)
(b) Rafsanjan, time span: May - July 2005 (70 d)
(c) Mashhad, time span: June - November 2004 (140 d)
(d) Kashmar, time span: August - December 2004 (105 d)
(e) Zarand-Kerman, time span: July - March 2004 (245 d)
(f) Yazd-Ardakan, time span: Sept. 2003 - Sept. 2004 (350 d)

Motagh et al., 2008b

Influence of geology on groundwater-related subsidence: Kashmar Valley, Iran

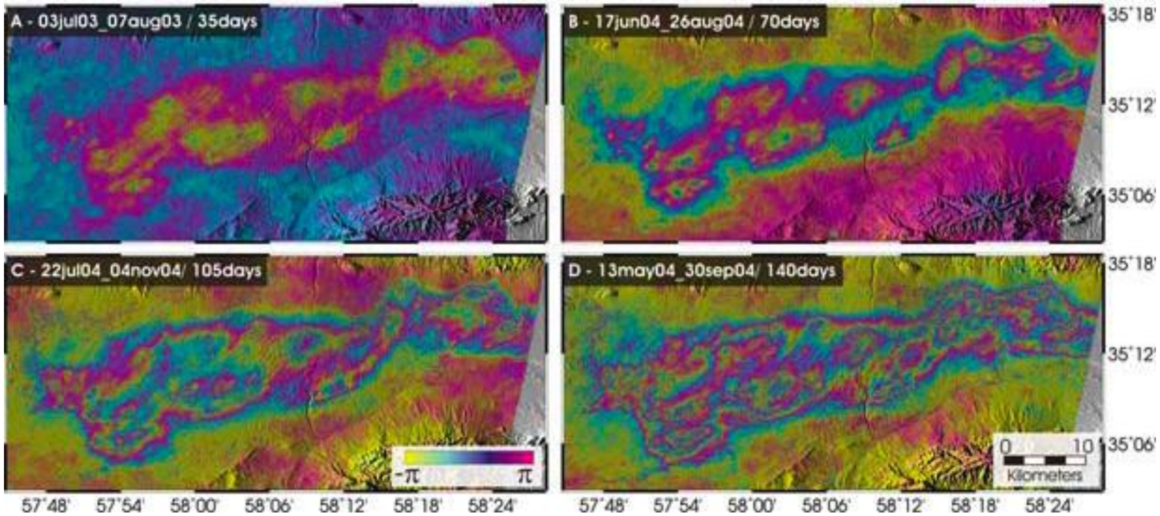

Four examples of Envisat interferograms (wrapped) showing the evolution of land subsidence in the valley

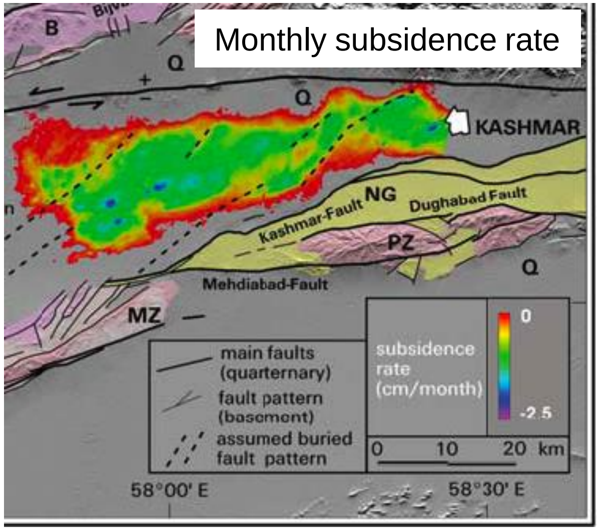

Average monthly velocity obtained by stacking of 22 interferograms covering 2003-2006 time period. Subsidence was interpreted as being influenced by old alpine basement faults.

Anderssohn et al., 2008

Groundwater-related surface deformation in Los Angeles, California

- Data: 42 ERS-1/-2 SAR data between 1995 and 2000
- Technique: Small BAseline Subset (SBAS)

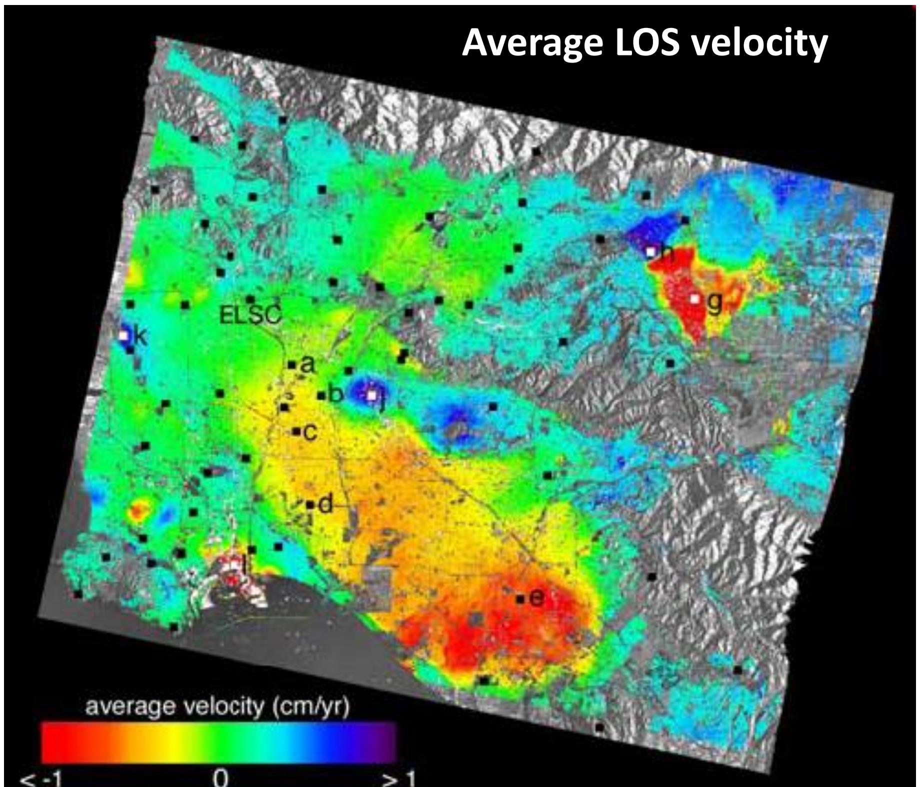

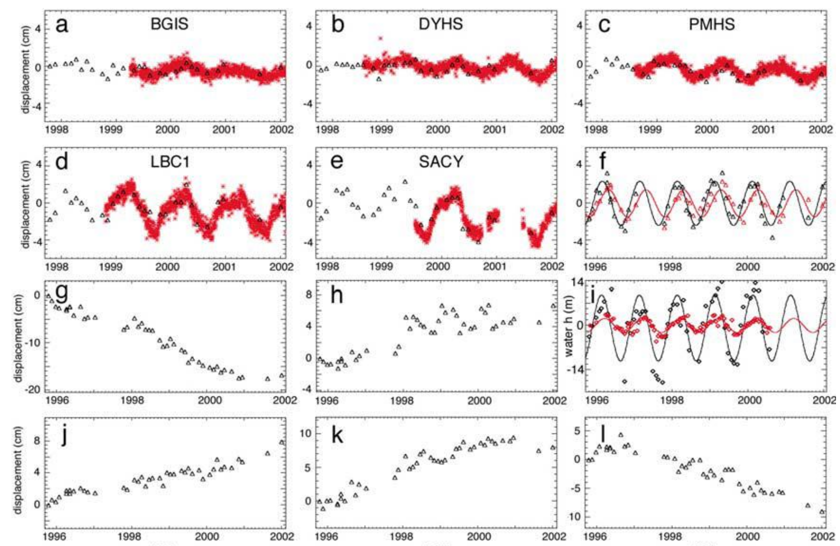

InSAR time-series at selected points shown on the left. Red stars are GPS data from Southern California Integrated GPS Network (SCIGN), shown by black squares on the left figure.

Lanari et al., 2004

New Orleans subsidence map

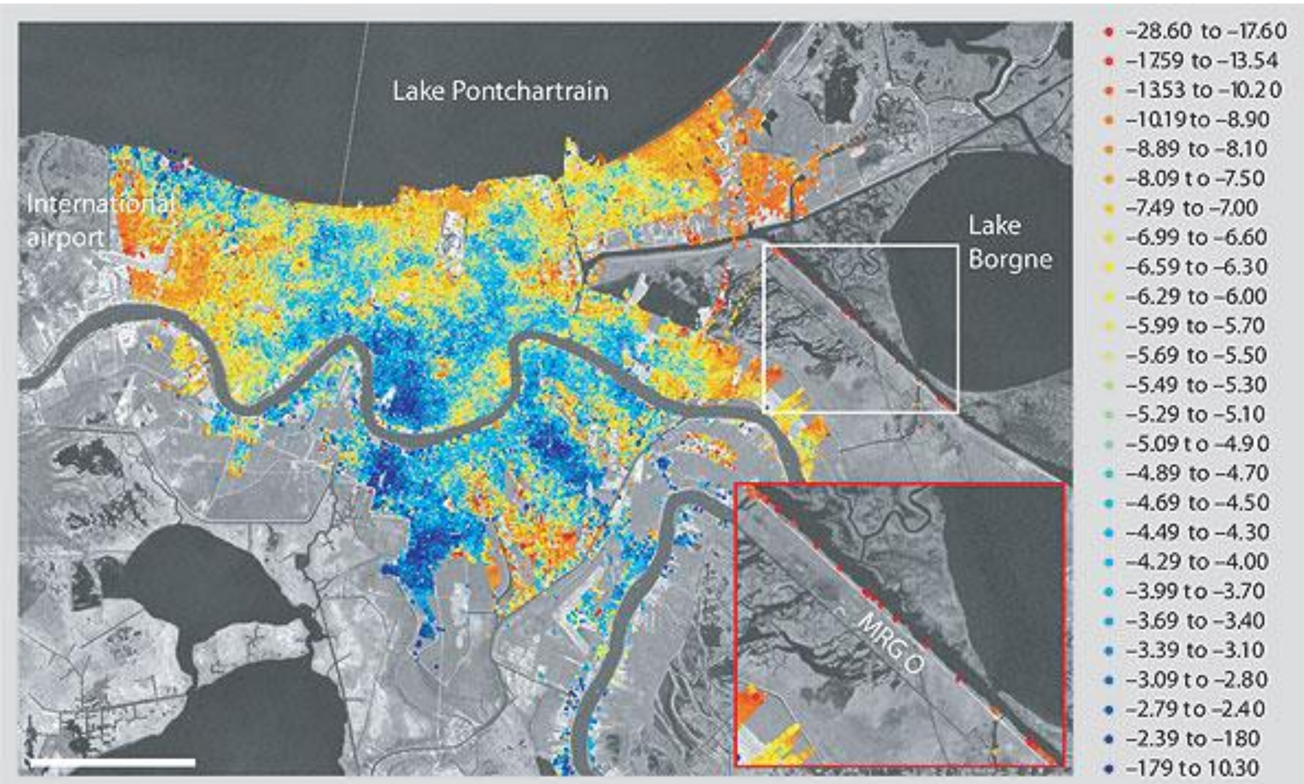

Dixon et al., 2006

- Subsidence map in New Orleans and vicinity during 2002-05 derived from permanent scatterer (PS) processing of 33 RADARSAT data
- High subsidence rate, at locations exceeding 2 cm/yr, west of Lake Borgne (white frame and its magnified view in the red frame)
- Insight into the failure of the levees during 2005 Hurricane Katrina

SAREDU Remote Sensing Education Initiative

PS-InSAR image of London

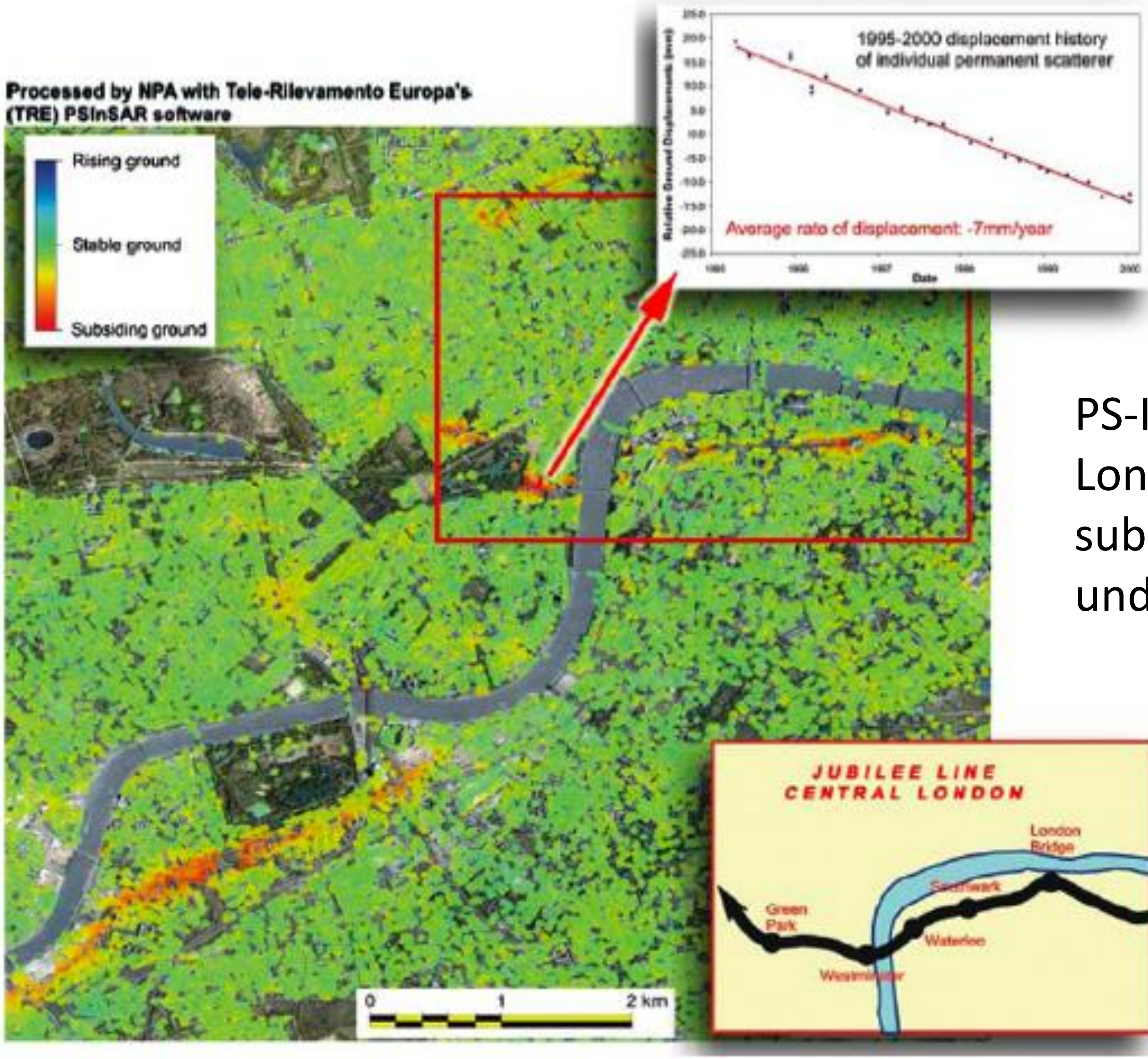

PS-InSAR image of London, showing subsidence due to underground railway

© NPA Group

Amsterdam, Netherlands: TSX InSAR time-series analysis

- **Purpose:**

  Documentation of surface movements in Amsterdam

- **Data:**

  TerraSAR-X

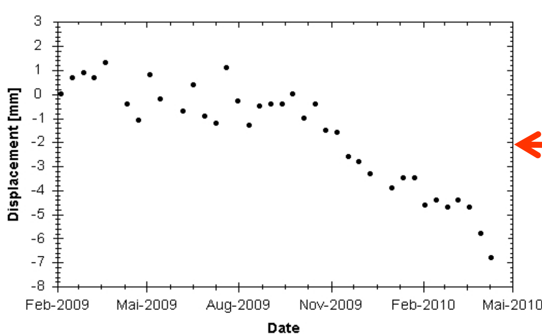

Amsterdam Railway Station

SAREDU Remote Sensing Education Initiative

Airport construction site monitoring (Japan)

- **Purpose:**

  Documentation of surface movements related to runway construction (unconsolidated soil / steel construction)

- **Customer:**

  Airport operator

- **Data:**

  TerraSAR-X

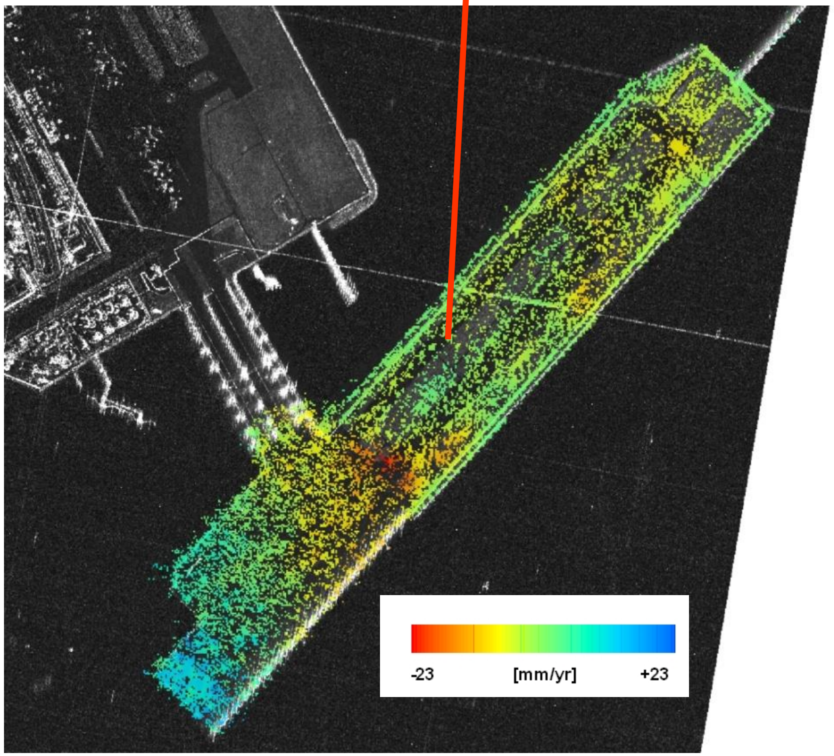

Oil-/gas production in Kuwait

Burghan Oilfield - surface movements derived from SBAS analysis of 16 TerraSAR-X datasets between 01/2008 and 02/2011

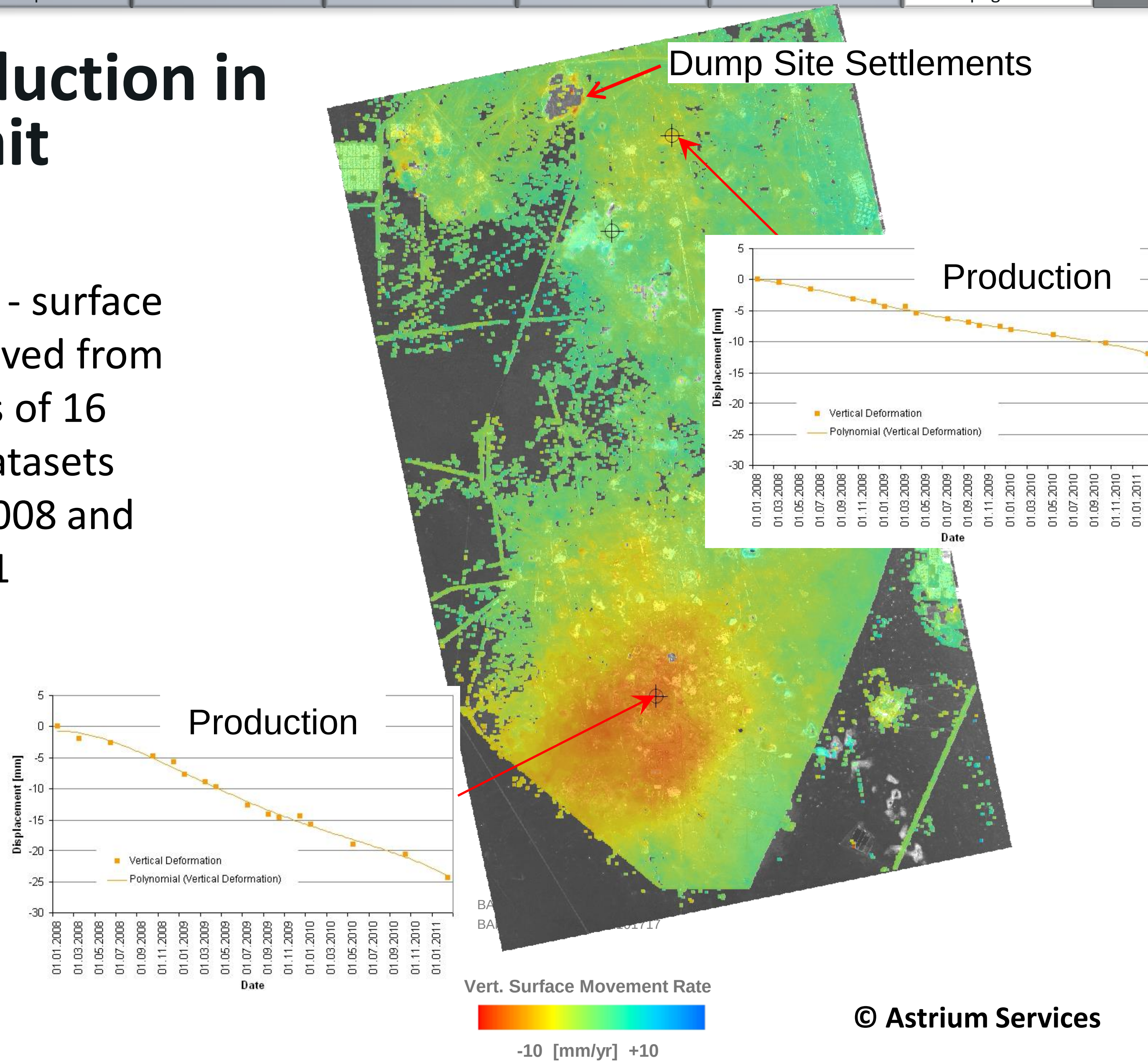

SAREDU Remote Sensing Education Initiative

CO2 storage site in Algeria, Africa

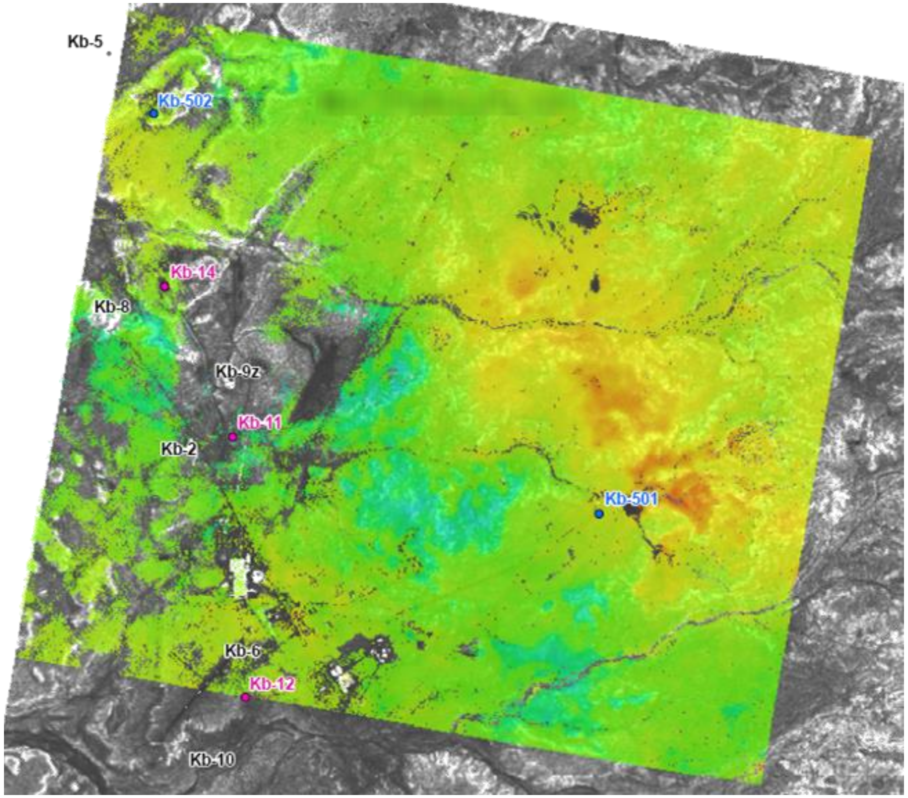

In Salah Gasfield (Algeria) and CO_2 injection/storage - TerraSAR-X surface displacement map based on PSI approach and 35 TSX datasets between 15/03/2008 and 29/05/2009

References

- Aki K., & Richards P. G. (1980): Quantitative Seismology, Vol. 1. W.H. Freeman, San Francisco, 558pp
- Amelung, F., Jonsson, S., Zebker, H. & Segall, P. (2000): Widespread uplift and trapdoor faulting on Galapagos volcanoes observed with radar interferometry. *Nature, 407*, 993-996.
- Anderssohn, J., Wetzel, H.-U., Walter, T. R., Motagh, M., Djamour, Y. & Kaufmann, H. (2008): Land subsidence pattern controlled by old alpine basement faults in the Kashmar Valley, northeast Iran: results from InSAR and levelling. *Geophysical Journal International, 174*, 287-294.
- Anderssohn, J., Motagh, M., Walter, T. R., Rosenau, M., Kaufmann, H. & Oncken, O. (2009): Surface deformation time series and source modeling for a volcanic complex system based on satellite wide swath and image mode interferometry: The Lazufre system, central Andes. *Remote Sensing of Environment, 113*, 2062-2075.
- Atzori, S., Hunstad, I., Chini, M., Salvi, S., Tolomei, C., Bignami, C., Stramondo, S., Trasatti, E., Antonioli, A. & Boschi, E. (2009): Finite fault inversion of DInSAR coseismic displacement of the 2009 L'Aquila earthquake (central Italy). *Geophysical Research Letters, 36*, L15305.
- Battaglia, M, Cervelli, P., & Murray J. R. (2013): dMODELS: A MATLAB software package for modeling crustal deformation near active faults and volcanic centers, *Journal of Volcanology and Geothermal Research,* DOI: 10.1016/j.jvolgeores.2012.12.018.
- Beavan, J., Samsonov, S., Motagh, M., Ellis, S. , Wallace, L., & Palmer, N. (2010): The Darfield (Canterbury) earthquake: geodetic observations and preliminary source model. *Bulletin of the New Zealand Society for Earthquake Engineering*, *43*(4), 228.

References

- Beavan, J., Motagh, M., Fielding, E. J., Donnelly, N. & Collett, D. (2012): Fault slip models of the 2010-2011 Canterbury, New Zealand, earthquakes from geodetic data and observations of postseismic ground deformation. *New Zealand Journal of Geology and Geophysics*, *55*(3), 1-15.
- Biggs, J., Burgmann, R., Freymueller, J. T., Lu, Z., Parsons, B., Ryder, I., Schmalzle, G. & Wright, T. (2009): The postseismic response to the 2002 M 7.9 Denali Fault earthquake: constraints from InSAR 2003–2005. *Geophysical Journal International, 176*, 353-367.
- Cakir, Z., Chabalier, J.B.d., Armijo, R., Meyer, B., Barka, A., Peltzer, G. (2003): Coseismic and early post-seismic slip associated with the 1999 Izmit earthquake (Turkey), from SAR interferometry and tectonic field observations. *Geophysical Journal International* 155, 93–110
- Carnec, C., Massonnet, D. & King, C. (1996): Two examples of the use of SAR interferometry on displacement fields of small spatial extent. *Geophysical Research Letters, 23*, 3579-3582.
- Cervelli, P., Murray, M. H., Segall, P., Aoki, Y. & Kato, T. (2001): Estimating source parameters from deformation data, with an application to the March 1997 earthquake swarm off the Izu Peninsula, Japan. *Journal of Geophysical Research, 106*(B6), 11217-11237.
- Colesanti, C. & Wasowski, J. (2006): Investigating landslides with space-borne Synthetic Aperture Radar (SAR) interferometry: *Engineering Geology*, Volume 88, Issues 3-4, Pages 173–199.
- Davis, P.M. (1986): Surface Deformation due to inflation of an arbitrarily oriented triaxial ellipsoidal cavity in an elastic half-space, with reference to kilauea Volcano, Hawaii, (1986), *Journal of Geophysical Research*, 91, B7, 7429-7438.

References

- D'Agostino, N., Cheloni, D., Fornaro, G., Giuliani, R. & Reale, D. (2012): Space-time distribution of afterslip following the 2009 L'Aquila earthquake. *Journal of Geophysical Research, 117*, B02402.
- Dixon, T. H., Amelung, F., Ferretti, A., Novali, F., Rocca, F., Dokka, R., Sella, G., Kim, S.-W., Wdowinski, S. & Whitman, D. (2006): Space geodesy: Subsidence and flooding in New Orleans. *Nature, 441*, 587-588.
- Du, Y., Aydin, A. & Segall, P. (1992): Comparison of various inversion techniques as applied to the determination of a geophysical deformation model for the 1983 Borah Peak earthquake. *Bulletin of the Seismological Society of America, 82*, 1840-1866.
- Dzurisin, D. (2007): *Volcano Deformation: Geodetic Monitoring Techniques*. Berlin, New York: Springer; Chichester, UK: Praxis Publishing.
- Fernández, J., Tizzani, P., Manzo, M., Borgia, A., González, P. J., Martì, J., Pepe, A., Camacho, A. G., Casu, F., Berardino, P., Prieto, J. F. & Lanari, R. (2009): Gravity-driven deformation of Tenerife measured by InSAR time series analysis. *Geophysical Research Letters, 36*, L04306.
- Fialko, Y., Khazan, Y. & Simons, M. (2001): Deformation due to a pressurized horizontal circular crack in an elastic half-space, with applications to volcano geodesy. *Geophysical Journal International, 146*, 181-190.
- Fialko, Y. (2006): Interseismic strain accumulation and the earthquake potential on the southern San Andreas fault system. *Nature, 441*, 968-971.
- Gottsmann, J, Rymer, H. & Berrino, G. (2006): Unrest at the Campi Flegrei caldera (Italy): A critical evaluation of source parameters from geodetic data inversion. *Journal of Volcanology and Geothermal Research*, 150(1-3) pp. 132–145.

References

- Jónsson, S. N., Zebker, H., Segall, P. & Amelung, F. (2002): Fault slip distribution of the Mw 7.1 Hector Mine, California, earthquake, estimated from satellite radar and GPS measurements. *Bulletin Seismological Society of America, 92*(4), 1377-1389.
- Jónsson, S., Segall, P., Pedersen, R. & Bjornsson, G. (2003): Post-earthquake ground movements correlated to pore-pressure transients. *Nature, 424*, 179-183.
- Lanari, R., Lundgren, P., Manzo, M. & Casu, F. (2004): Satellite radar interferometry time series analysis of surface deformation for Los Angeles, California. *Geophysical Research Letters, 31*, L23613.
- Lohman, R. B., Simons, M. & Savage, B. (2002): Location and mechanism of the Little Skull Mountain earthquake as constrained by satellite radar interferometry and seismic waveform modeling. *Geophysical Research Letters*, *107,* 2118.
- Lohman, R. B. & Simons, M. (2005): Locations of selected small earthquakes in the Zagros mountains. *Geochemistry, Geophysics, Geosystems, 6*(3), Q03001.
- Lu, Z., Masterlark, T., Dzurisin, D., Rykhus, R. & Wicks, C., Jr. (2003a): Magma supply dynamics at Westdahl volcano, Alaska, modeled from satellite radar interferometry. *Journal of Geophysical Research*, *108*, 2354.
- Lu, Z., Fielding, E., Patrick, M. R., & Trautwein, C. (2003b): Estimating lava volume by precision combination of multiple baseline spaceborne and airborne interferometric synthetic aperture radar: the 1997 eruption of Okmok volcano, Alaska. *IEEE Transactions on Geoscience and Remote Sensing*, v. 41, n. 6, p. 1428-1436.

SAREDU
Remote Sensing Education Initiative

References

- Lu, Z., Wicks Jr., C., Kwoun, O., Power, J. A. & Dzurisin, D. (2005): Surface deformation associated with the March 1996 earthquake swarm at Akutan Island, Alaska, revealed by C-band ERS and L-band JERS radar interferometry. *Canadian Journal of Remote Sensing, 31*, 7-20.
- Lu, Z., (2007): InSAR Imaging of Volcanic deformation over cloud-prone areas Aleutian Islands, *Photogrammetric Engineering & Remote Sensing*, Vol 73, No. 3, 245-257.
- Massonnet, D. & Feigl, K. L. (1998): Radar interferometry and its application to changes in the Earth's Surface. *Reviews of Geophysics, 36*(4), 441-500.
- McTigue, D. F. (1987): Elastic stress and deformation near a finite spherical magma body: resolution of the point source paradox. *Journal of Geophysical Research , 92*, 12931-12940.
- Mogi, K. (1958): Relations between the eruptions of various volcanoes and the deformations of the ground surfaces around them. *Bulletin of the Earthquake Research Institute of the University of Tokyo, 36,* 111-123.
- Motagh, M., Klotz, J., Tavakoli, F., Djamour, Y., Arabi, S., Wetzel, H.-U. & Zschau, J. (2006): Combination of Precise Leveling and InSAR Data to Constrain Source Parameters of the Mw = 6.5, 26 December 2003 Bam Earthquake. *Pure and Applied Geophysics, 163*, 1-18.
- Motagh, M., Hoffmann, J., Kampes, B., Baes, M. & Zschau, J. (2007): Strain accumulation across the Gazikoy-Saros segment of the North Anatolian Fault inferred from Persistent Scatterer Interferometry and GPS measurements. *Earth and Planetary Science Letters, 255, 432-444.*

References

- Motagh, M., Wang, R., Walter, T. R., Bürgmann, R., Fielding, E., Anderssohn, J. & Zschau, J. (2008a): Coseismic slip model of the 2007 August Pisco earthquake (Peru) as constrained by Wide Swath radar observations. *Geophysical Journal International, 174*, 842-848.
- Motagh, M., Walter, T. R., Sharifi, M. A., Fielding, E., Schenk, A., Anderssohn, J. & Zschau, J. (2008b): Land subsidence in Iran caused by widespread water reservoir overexploitation. *Geophysical Research Letters, 35*, L16403.
- Motagh, M., Schurr, B., Anderssohn, J., Cailleau, B., Walter, T. R., Wang, R. & Villotte, J.-P. (2010): Subduction earthquake deformation associated with 14 November 2007, Mw 7.8 Tocopilla earthquake in Chile: Results from InSAR and aftershocks. *Tectonophysics, 490*, 60-68.
- Okada, Y. (1985): Surface deformation due to shear and tensile faults in a half-space. *Bulletin of the Seismological Society of America ,75*, 1135-1154.
- Okada, Y. (1992): Internal deformation due to shear and tensile faults in a half-space. *Bulletin of the Seismological Society of America, 82*, 1018-1040.
- Pathier, E., Fielding, E. J., Wright, T. J., Walker, R., Parsons, B. E. & Hensley, S. (2006): Displacement field and slip distribution of the 2005 Kashmir earthquake from SAR imagery. *Geophysical Research Letters , 33*, L20310.
- Parsons, B., Wright, T., Rowe, P., Andrews, J., Jackson, J., Walker, R., Khatib, M., Talebian, M., Bergman, E. & Engdahl, E. R. (2006): The 1994 Sefidabeh (eastern Iran) earthquakes revisited: new evidence from satellite radar interferometry and carbonate dating about the growth of an active fold above a blind thrust fault. *Geophysical Journal International*, 164: 202–217. doi: 10.1111/j.1365-246X.2005.02655.x

SAREDU Remote Sensing Education Initiative

References

- Peltzer, G., Rosen, P., Rogez, F. & Hudnut, K. (1996): Postseismic rebound in fault step-overs caused by pore fluid flow. *Science, 273*, 1202-1204.
- Peyret, M., Dominguez, S., Cattin, R., Champenois, J., Leroy, M. & Zajac, A. (2011): Present-day interseismic surface deformation along the Longitudinal Valley, eastern Taiwan, from a PS-InSAR analysis of the ERS satellite archives. *Journal of Geophysical Research*, *116,* B03402.
- Pollitz, F. F., Wicks, C. & Thatcher, W. (2001): Mantle flow beneath a continental strike-slip fault: postseismic deformation after the 1999 Hector Mine earthquake. *Science, 293*, 1814-1818.
- Pritchard, M. E. & Simons, M. (2002): A satellite geodetic survey of large-scale deformation of volcanic centres in the central Andes. *Nature, 418*, 167-171.
- Ranalli, G. (1995): Rheology of the Earth. ISBN-13: 978-0412546709, Edition: 2nd
- Rice J. R., & Cleary, M. P. (1976): Some basic stress diffusion solutions for fluid-saturated elastic porous media with compressible constituents, *Reviews of Geophysics,* 14,2, 227-241
- Ryder, I., Parsons, B., Wright, T. J. & Funning, G. J. (2007): Post-seismic motion following the 1997 Manyi (Tibet) earthquake: InSAR observations and modelling. *Geophysical Journal International, 169*, 1009-1027.
- Salichon, J., Lundgren, P., Delouis, B., & Giardini, D. (2004): Slip history of the 16 October 1999 Mw 7.1 Hector Mine earthquake (California) from the inversion of InSAR, GPS, and teleseismic data. *Bulletin of the Seismological Society of America*, *94*(6), 2015-2027.
- Segall, P. (2002): Integrating geologic and geodetic estimates of slip rate on the San Andreas Fault System. *International Geology Review, 44,* 62-82.

SAREDU Remote Sensing Education Initiative

References

- Simons, M., Fialko, Y., & Rivera, L. (2002): Coseismic deformation from the 1999 Mw 7.1 Hector Mine, California, earthquake as inferred from InSAR and GPS observations. *Bulletin of the Seismological Society of America*, *92*(4), 1390-1402.
- Strozzi, T., Farina, P., Corsini, A., Ambrosi, C., Thüring, M., Zilger, J., Wiesmann, A., Wegmüller, U. & Werner, C. (2005): Survey and monitoring of landslide displacements by means of L-band satellite SAR interferometry. *Landslides, 2*, 193-201.
- Strozzi, T., Delaloye, R., Kääb, A., Ambrosi, C., Perruchoud, E. & Wegmüller, U. (2010): Combined observations of rock mass movements using satellite SAR interferometry, differential GPS, airborne digital photogrammetry, and airborne photography interpretation. *Journal of Geophysical Research, 115*, F01014.
- Walters, R. J., Holley, R. J., Parsons, B., & Wright, T. J. (2011): Interseismic strain accumulation across the North Anatolian Fault from Envisat InSAR measurements. *Geophysical research letters*, *38*(5).
- Wang, R., Kümpel, H.-J. (2003): Poroelasticity; efficient modeling of strongly coupled, slow deformation processes in a multilayered half-space. *Geophysics*, *68*, 2, p. 705-717.
- Wang, R. Lorenzo-Martin, F. & Roth, F. (2003): Computation of deformation induced by earthquakes in a multi-layered elastic crust—FORTRAN programs EDGRN/EDCMP. *Computers & Geosciences*, 29, 195-207
- Wang, R. Lorenzo-Martin, F. & Roth, F. (2006): PSGRN/PSCMP-a new code for calculating co- and post-seismic deformation, geoid and gravity changes based on the viscoelastic-gravitational dislocation theory, *Computers & Geosciences* 32, 527-542.

SAREDU Remote Sensing Education Initiative

References

- Wdowinski, S. & Hong, S. H. (2011): Postseismic deformation following the 2010 Haiti earthquake: time-dependent surface subsidence induced by groundwater flow in response to a sudden uplift. Presentation on Fringe 2011, 19. – 23. September 2011, Frascati, Italy. Retrieved October, 10, 2012 from http://earth.eo.esa.int/workshops/fringe2011/files/Wdowinski_FRINGE2011.pdf
- Weston, J., Ferreira, A. M. G. & Funning, G. J. (2011): Global compilation of interferometric synthetic aperture radar earthquake source models: 1. Comparisons with seismic catalogs. *Journal of Geophysical Research, 116*, B08408.
- Weston, J., Ferreira, A. M., & Funning, G. J. (2012): Systematic comparisons of earthquake source models determined using InSAR and seismic data. *Tectonophysics*, *532*, 61-81.
- Wright, T., Parsons, B. & Fielding, E. (2001): Measurement of interseismic strain accumulation across the North Anatolian Fault by satellite radar interferometry. *Geophysical Research Letters, 28,* 2117-2120.
- Wright, T. J., Lu, Z. & Wicks, C. (2004): Constraining the slip distribution and fault geometry of the Mw 7.9, 3 November 2002, Denali Fault earthquake with interferometric synthetic aperture radar and global positioning system data. *Bulletin of the Seismological Society of America, 94,* S175-S189
- Wright, T. J., Ebinger, C., Biggs, J., Ayele, A., Yirgu, G., Keir, D. & Stork, A. (2006): Magma-maintained rift segmentation at continental rupture in the 2005 Afar dyking episode. *Nature, 442*, 291-294.
- Yang, X.-M., Davis, P. M. & Dieterich, J. H. (1988): Deformation from inflation of a dipping finite prolate spheroid in an elastic half-space as a model for volcanic stressing. *Journal of Geophysical Research*, *93*, 4249-4257.

SAREDU Remote Sensing Education Initiative

SAR-EDU – SAR Remote Sensing Educational Initiative

https://saredu.dlr.de/

Supported by:

Federal Ministry
of Economics
and Technology

on the basis of a decision
by the German Bundestag

SAREDU
Remote Sensing
Education Initiative